Nanoscale investigation of light-matter interactions mediated by magnetic and electric coupling

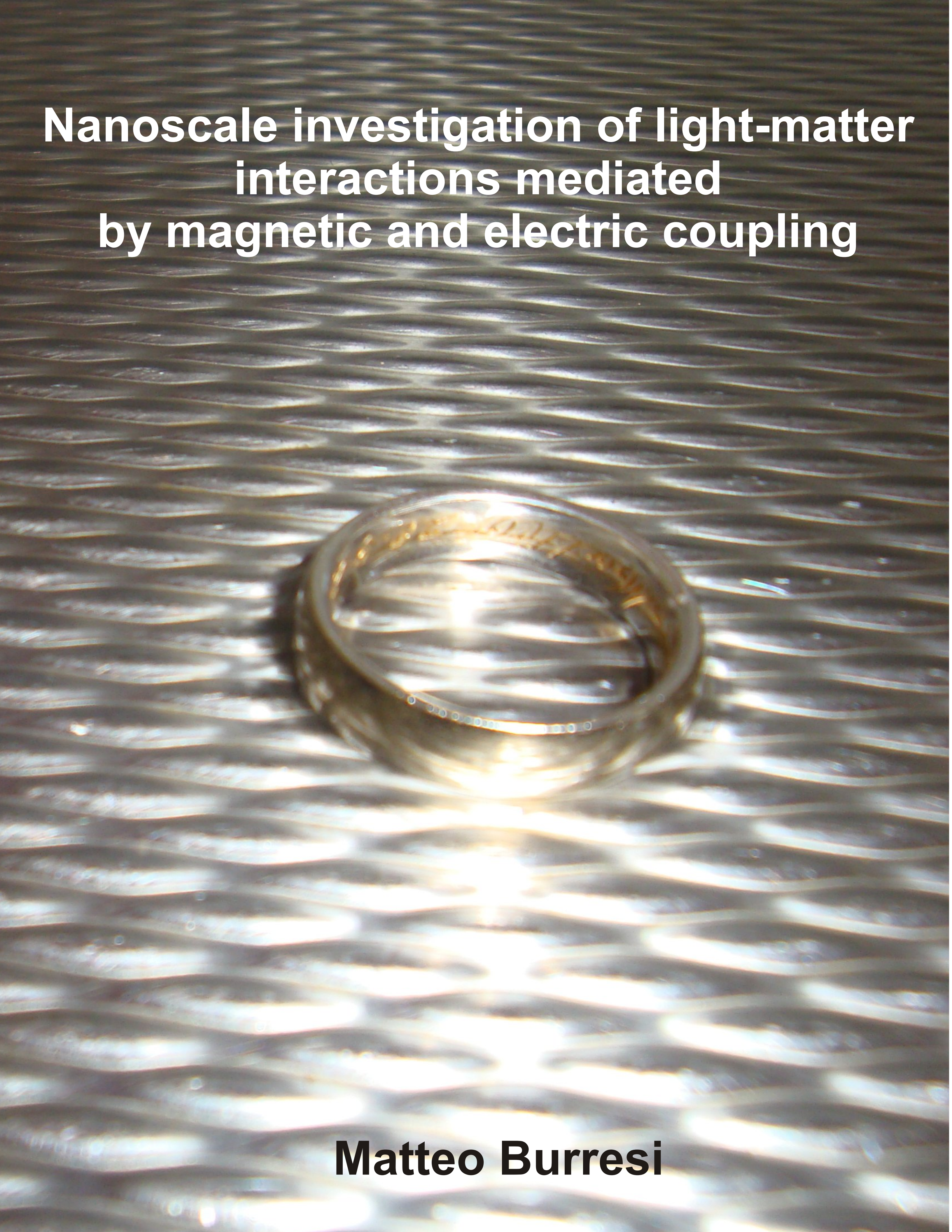

Matteo Burresi

NANOSCALE INVESTIGATION OF LIGHT-MATTER INTERACTIONS MEDIATED BY MAGNETIC AND ELECTRIC COUPLING

Samenstelling van de promotiecommissie:

prof. dr. L. Kuipers (promotor)	Universiteit Twente
prof. dr. H. Giessen	Universität Stuttgart
prof. dr. A. Fiore	Technische Universiteit Eindhoven
prof. dr. V. Subramaniam	Universiteit Twente
prof. dr. B. Poelsema	Universiteit Twente
prof. dr. A. van den Berg	Universiteit Twente

This work is also supported by NanoNed, a nanotechnology
program of the Dutch Ministry of Economic Affairs
(project number 6943)
and is part of the research program of the
“Stichting Fundamenteel Onderzoek der Materie” (FOM), which is
financially supported by the
“Nederlandse Organisatie voor Wetenschappelijk Onderzoek” (NWO).

This work was carried out at:
NanoOptics Group,
FOM-Institute for Atomic and Molecular Physics (AMOLF)
Science Park 113, 1098 XG Amsterdam, The Netherlands,
where a limited number of copies of this thesis is available.

ISBN: 978-90-365-2876-4
Printed by Ipskamp Drukkers, The Netherlands.

NANOSCALE INVESTIGATION OF LIGHT-MATTER INTERACTIONS MEDIATED BY MAGNETIC AND ELECTRIC COUPLING

PROEFSCHRIFT

ter verkrijging van
de graad van doctor aan de Universiteit Twente,
op gezag van de Rector Magnificus,
Prof. Dr. H. Brinksma,
volgens besluit van het College voor Promoties
in het openbaar te verdedigen
op donderdag 24 September 2009 om 13:15

door

Matteo Burresi

geboren op 21 februari 1979,
te Firenze (IT)

Dit proefschrijft is goedgekeurd door:
Prof. Dr. L. (Kobus) Kuipers

Alla memoria di mio nonno,
Virgilio Bartolini

Publications related to this thesis:

M. Burresi, R. J. P. Engelen, A. Opheij, D. van Oosten, D. Mori, T. Baba, and L. Kuipers, Observation of Polarization Singularities at the Nanoscale, *Physical Review Letters* **102**, 033902 (2009).

M. Burresi, T. Kampfrath, D. van Oosten, J.C. Prangsma, B.S. Song, S. Noda and L. Kuipers, Active control of light trapping by means of local magnetic coupling, submitted.

M. Burresi, D. van Oosten, T. Kampfrath, H. Schoenmaker, R. Heideman, A. Leinse and L. Kuipers, Detecting the magnetic field of light at optical frequencies, submitted.

Other manuscript related to this thesis:

M. Burresi, B.S. Song, S. Noda and L. Kuipers, Local investigation of nano-confinement of light in space and time, in preparation.

Other publications:

C.M. Bruinink, M. Burresi, M.J. de Boer, F.B. Segerink, H.V. Jansen, E. Berenschot, D.N. Reinhoudt, J. Huskens, and L. Kuipers, Nanoimprint Lithography for Nanophotonics in Silicon, *Nano Letters* **8 (9)**, 2872 (2008).

T. Kampfrath, D.M. Beggs, T.P. White, M. Burresi, D. van Oosten, T.F. Krauss, and L. Kuipers, Ultrafast re-routing of light via slow modes in a nano-photonic directional coupler, *Applied Physics Letters* **94**, 241119 (2009).

S. Vignolini, M. Burresi, S. Gottardo, L. Kuipers and D. S. Wiersma, Vortex and field correlation in the near-field of a three dimensional disordered photonic crystal, submitted.

Contents

Introduction

Human beings have come to master the interaction between light and matter to improve the quality of their life. We take for granted such daily actions as turning on the light in a dark room to perceive our surroundings and generally we do not fully appreciate all occurring light-matter interactions. In fact, light propagating through air, is scattered by the objects in the room, travels again through air and, eventually, interacts with our eyes. Only at that point we can we see the room.

Nowadays, refined techniques to control light-matter interaction are demanded. Faster transfer and computation of information can be achieved using optics, more efficient low-carbon-footprint energy production can be obtain with photovoltaic systems and laser devices can be used for highly accurate medicine procedures. Nano-optics is one of the modern answers to these needs. In fact, nano-optics is strongly application-oriented, trying not only to gain new fundamental knowledge but also to create a benefit for society. Investigations of the quantum and classical properties of light interacting with disordered, ordered and quasi-ordered dielectric structures, or metallic and metallo-dielectric materials tailored at the nanoscale stimulate the interest of the scientific communities of all the industrialized societies.

This thesis spans three central fields of nano-optics, which are photonic crystals, metamaterials and near-field microscopy. Through a study that aims to a better understanding of this microscopy, we investigated the optical properties of photonic nanostructures by means of both magnetic and electric coupling.

In Chapter 1 we will provide a brief summary of the topics related to this thesis. After a brief introduction to light-matter coupling, we will discuss some of the main modern strategies employed to control the flow of light, such as photonic crystal waveguides and photonic crystal cavities. As a result of the strong interaction between light and these man-made materials, light undergoes complicated interference patterns, where optical singularities might arise. We will also provide some of the basic concepts of singular optics. The field distribution of light in photonic nanostructures is characterized by subwavelength features. Near-field microscopy will be introduced as a powerful tool that provides us with the necessary subwavelength resolution.

In Chapter 2 we will discuss the electromagnetic response of three different near-field probes. After considerations based on metamaterials concepts, we will show that coupling between light and probe can be described by electric and magnetic polarizability matrices. Subsequently, we will introduce the phase-sensitive, time-resolved, near-field microscope employed in all the investigations in this work.

In the next part of the thesis we will experimentally prove some of the optical properties of the probes discussed in Chapter 2 and exploit them to perform a novel type of investigation. In Chapter 3 we will show that a coated probe combined with a polarization sensitive near-field microscope allows us to separately detect the in-plane components of the electric field of propagating light in a 2D photonic crystal waveguide. Consequently, we will perform a study of optical singularities of light in the waveguide.

In Chapter 4 we will demonstrate the coupling between a coated probe to a photonic crystal cavity through the magnetic component of the confined light. We will achieve a novel blue-shift of the cavity resonance and an unexpected increase of the photon lifetime of the cavity.

In Chapter 5 the coupling mechanism between an L3 side-coupled nanocavity and the mode of an access waveguide will be unraveled. By performing phase-sensitive, time-resolved, near-field microscopy and a subsequent Fourier analysis, we will show that the -1 first Bloch harmonic of light propagating in the photonic crystal waveguide mediates the coupling between waveguide and nanocavity.

In Chapter 6 we will show that a functionalized coated probe exhibit a magnetic response. We will exploit this response to directly detect the magnetic field at optical frequencies. By performing a near-field experiment on a ridge waveguide, we will detect the magnetic component of propagating light.

Chapter 1

Background concepts

1.1 Introduction

Electromagnetism deals with magnetic and electric fields and their interaction with matter. Materials are classified based on their susceptibility to a constant electric and magnetic field. In the case of an electric response, a material can be a conductor, where a high concentration of free carriers (electrons) is available, a semiconductor, with a low free carrier concentration, or an insulator, where the free carrier concentration is zero [1]. In the case of a magnetic response, materials are classified as ferromagnetic, paramagnetic and diamagnetic. Here, the classification is based on the ease with which the spins characterizing the material orient under an applied constant magnetic field [1].

However, the above mentioned nomenclature loses its meaning once we deal with electromagnetic waves. Let us consider a metal in an electric field which oscillates in time. At low frequencies ($\nu < 1$ THz) the electrons move in phase with the external electric field, such that the total field inside the metal is zero. As a result, the electric field, and thus light, is shielded by the metal [2]. However, the electrons cannot move with infinite speed. When the field varies faster than the response of the electrons, the electric field is no longer screened and can penetrate into the metal. The penetration of the field (*skin depth*) becomes larger as the frequency approaches the so-called *plasma frequency* ν_p. In this regime, light can strongly couple to the electrons present at a metallic interface, which creates surface electromagnetic waves (*surface plasmon polaritons*) [3]. As the frequency becomes larger than ν_p, the metal exhibits a dielectric-like behavior [2]. This resonance frequency is in the ultraviolet or visible range ($\nu_p > 700$ THz) for all metals. Analogously, an insulator can be considered as a material with $\nu_p = 0$ and, thus, light can penetrate it. On the other hand, a semiconductor has a low, but not vanishing, ν_p ($0.1 - 10$ THz, depending on the doping). At frequencies smaller than ν_p, the semiconductor behaves like a metal, reflecting the oscillating electric field [4]. Evidently the nomenclature developed in the electrostatic limit does not describe light-matter interaction.

The magnetic response of matter also drastically changes at optical frequencies. In fact, the magnetic field plays a significant role only for slowly varying electromagnetic fields [5]. Not even atomic spin waves (*magnons*) can be excited by a magnetic field at frequencies $\nu > 1$ THz [6]. Strictly speaking, the magnetic component of light does interact with matter at optical frequencies [7]. However, this interaction is generally negligible with respect to the electric coupling and magnetic light-matter interaction is omitted in most textbooks of classical electrodynamics. In order to understand this asymmetry in electromagnetism, we consider the force exerted by light on a moving charge in vacuum, the well known Lorentz force. For the sake of clarity, we write the Lorentz force in Gaussian (CGS) units. *We will use the Gaussian system instead of the International System only in this occasion.* The Lorentz force is [8]

$$\boldsymbol{F} = q\left(\boldsymbol{E} + \frac{\boldsymbol{v}}{c} \times \boldsymbol{B}\right) , \tag{1.1}$$

where q is the charge, $\boldsymbol{v}$ is the velocity of the charge and c is the speed of light. As we will discuss in Appendix B, in CGS the electric field $\boldsymbol{E}$ has the same unit as the magnetic field $\boldsymbol{B}$. Because $\boldsymbol{E}$ and $\boldsymbol{B}$ of an electromagnetic wave in vacuum have the same energy [2], and thus the same amplitude, it is clear that the magnetic component of the Lorentz force is v/c smaller than the electric component. Only in case of relativistic charges ($v \approx c$) the two components are comparable. Let us consider the hydrogen atom. The velocity of the electron bound to the atom is approximately two order of magnitude smaller than the speed of light. More precisely, $v/c \simeq \alpha = 1/137$, where α is the fine-structure constant. The probability that light induces a dipole transition in a hydrogen atom scales as $|F|^2$. Consequently, a magnetic coupling is $\alpha^2 \approx 10^{-4}$ smaller than the electric coupling. As a result, at the macroscopic level the magnetic susceptibility of a material is generally $\sim 10^{-4}$ the electric susceptibility [5]. Hence, light-matter coupling is governed by the electric interaction.

Consequently, the control of light propagation is generally mediated by the electric permittivity of matter. Classical examples are lenses, dielectric and metallic mirrors, prisms, etc. Even an optical isolator, that is based on the Faraday effect, exploits the interaction between the electric field of light and the anisotropy of the electric permittivity induced by the permanent magnetization of a ferromagnetic material [5]. Nowadays, new strategies for controlling the light flow are being developed. For instance, photonic crystals provide a high level of control of light propagation and are based on the electric interaction between light and spatially engineered dielectric materials (see Section 1.2).

Modern alternatives are the so-called metamaterials. These materials exhibit a magnetic response even at optical frequencies, which can be exploited to control the flow of light. The physics lying behind this effect can be summarized as follows. The metal present in the metamaterials is tailored with geometries that are equivalent to subwavelength metallic loops. Due to Faraday's law, a single loop exhibits an induced magnetic dipole resulting from the magnetically induced circular current. Because the dimensions of these loops are much smaller than the wavelength of the employed light, a metamaterial exhibits a homogenous effective magnetic response at optical frequencies that is comparable with the electric response. Metamaterials are promising for achieving new and exciting optical phenomena, such as negative index of refraction [9], super-focusing [10] and cloaking [11,12].

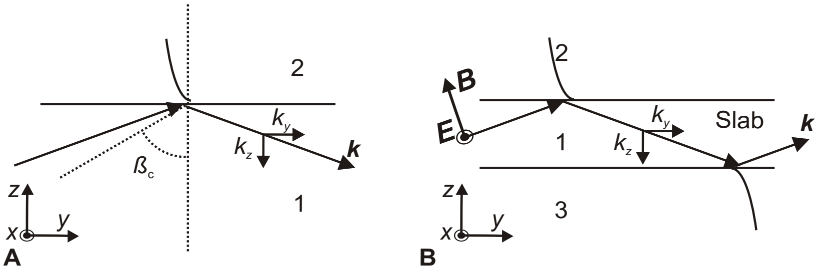

Figure 1.1:
A, *Schematic representation of total internal reflection. The rays represent the wave vectors of light that is totally reflected by the interface between the two media. The exponential decay represent the evanescent field in medium 2.* β_c *is the critical angle.* **B**, *Schematic representation of a slab waveguide. Light that impinges at the surfaces with an angle larger than* β_c *is confined inside the slab along* $\hat{z}$*. In this schematics the electric field is parallel to the slab.*

1.2 Guiding and trapping light

In this Section we describe light propagation controlled by engineered dielectric materials. Light can be guided through sharp corners [13] or trapped in volumes comparable with the cubed wavelength [14]. In order to guide or trap it, light must be confined, reducing the degrees of freedom of its propagation. In this thesis we will deal only with 2D photonic structures, where light is guided (or confined) by total internal reflection. Let us consider light propagating in medium 1 towards the interface with medium 2 (Fig. 1.1A). Medium 1 has higher refractive index than medium 2. Snell's law teach us that light impinging at the interface with an angle of incidence above a certain critical angle β_c will experience total reflection (Fig. 1.1A) and only an evanescent field will extend into medium 2 [3]. When medium 1 is a slab that separates medium 2 and medium 3, both with a refractive index smaller than medium 1, light cannot escape from it and the slab becomes a waveguide (a *slab waveguide*, Fig. 1.1B). Light in such a waveguide experiences an effective refractive index that primarily depends on the thickness of the slab and differs from the refractive index of the bulk material: the thinner is the slab the smaller is the effective

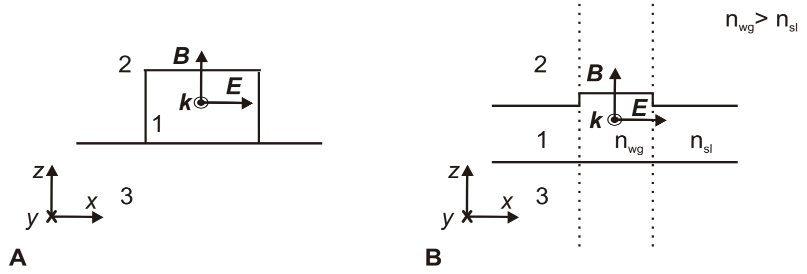

Figure 1.2:
A, *Schematic cross-section of a 'wire' waveguide. The waveguide lies on a substrate of smaller refractive index. Due to total internal reflection, light cannot propagate in the* xz*-plane. The electromagnetic wave is guided along* $\hat{y}$*, as indicated by the wave vector.* **B**, *Schematic cross-section of a ridge waveguide. The slab lies on a substrate of smaller refractive index. A ridge in the profile of the slab is created. The effective refractive index in the ridge area (between the dashed lines) is higher than in the slab area. Light is guided along* $\hat{y}$.

refractive index. It can be analytically proved that, in the limit of an infinitesimally small slab, light can always be trapped in a dielectric slab regardless of the wavelength [15]. However, the effective refractive index contrast with the surrounding media decreases as the slab becomes thinner. As a result, the evanescent field extends further and the amount of electromagnetic energy confined to the slab decreases. In this thesis we use slabs of thickness between 150 and 300 nm, which is much smaller than the employed vacuum wavelength (around 1500 nm).

1.2.1 Ridge waveguides

By using a slab-waveguide we confine the light in one direction of space. In order to confine light also along another direction we can once again use total internal reflection. The first strategy could be to use a dielectric wire (Fig. 1.2A). In such a system light is confined in $\hat{x}$ and $\hat{z}$ and, thus, propagates along $\hat{y}$. Alternatively, we can slightly modify the effective refractive index in an area of the slab. Figure 1.2B shows a cross-section of a so-called ridge waveguide. This waveguide is obtained by creating a smal step, or a ridge, in the profile of a slab waveguide. The effective refractive index n_{wg} in the ridge area is higher than in the rest of the slab (n_{sl}). Hence, light is confined also along $\hat{x}$ and propagates along $\hat{y}$ (Fig. 1.2B). A ridge waveguide generally has a weaker lateral confinement than a 'wire' waveguide. In fact, the lateral refractive index contrast ($\Delta n = (n_{wg} - n_{sl})/n_{sl}$) for a typical ridge waveguide is only [0.01...0.1]. As a result, the transverse component of the wave vector must be much smaller than the longitudinal component, because it must obey the Snell's law. In other words, $\beta_{\mathrm{c}} \approx 90$ degrees and the wave vector is approximately parallel to the waveguide. Let us consider, for instance, the ridge waveguide that we investigate in Chapter 6. The sample consists of a Si wafer on top of which an 8 µm layer of thermal silicon oxide has been grown. The waveguide is obtained by growing a 170 nm Si_3N_4 layer and subsequently by dry etching a straight ridge with a width of 2 µm and a height of 20 nm. This waveguide supports only a weakly guided transverse electric (TE) mode with an effective refractive index ~ 1.46, whereas the refractive index of the bulk Si_3N_4 is ~ 1.9. Figure 1.3 shows the numerically calculated electric and magnetic field components in the waveguide obtained by global mode expansion[1] [16]. Because the lateral refractive index contrast is only $\Delta n \sim 0.07$, $E_x \gg E_y \approx 4E_z$ and $k_y \gg k_x$. Note that strictly speaking the mode does not have a pure transverse electric field. This terminology is a heritage of the field that studies slab waveguides, where there is no lateral confinement and, thus, the electric field is perfectly transverse. As we will show in Section 1.2.2 and Chapter 3, the name TE for modes in a photonic crystal waveguide is even more misleading because there the longitudinal and the transverse component of the electric field are in fact of comparable magnitude. In order to clarify, we call TE the mode that can be excited by light with polarization oriented parallel to the slab on which the waveguide is grown.

A closer look to the magnetic field distribution shows that $B_z \approx 2B_y \gg B_x$. This is due to the fact that the refractive index contrast along $\hat{z}$ is $\Delta n \sim 0.46$ and the z-component of the wave vector is comparable with the y-component, as it is shown in Fig. 1.1B. $\boldsymbol{B}$ and $\boldsymbol{E}$ must be orthogonal to the wave vector[2] and, thus, $\boldsymbol{B}$ must be tilted with respect to $\hat{z}$. As a

---

[1] These calculations are a generously provided by O. (Alyona) Ivanova and M. Hammer, University of Twente.

[2] Strictly speaking $\boldsymbol{E}$ and $\boldsymbol{B}$ have to be orthogonal to the Poynting vector $\boldsymbol{S}$. However,

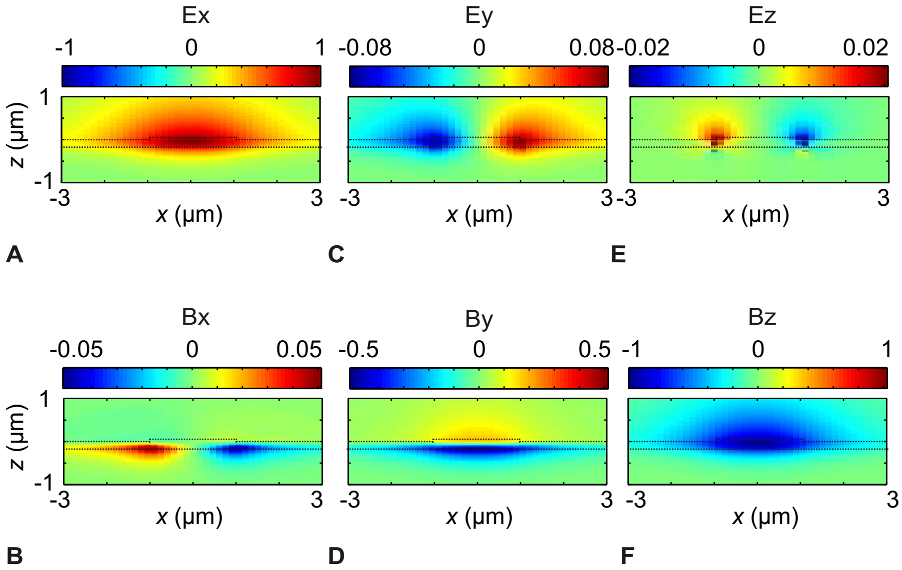

Figure 1.3:
Calculated distribution of the six fields, in the xy-plane, of light in a ridge waveguide. Light propagates in the negative y-direction. The ridge profile is also indicated. The electric (magnetic) fields are normalized to the maximum electric (magnetic) field component.

result, the longitudinal component of the magnetic field is not negligible with respect to the transverse component.

1.2.2 Photonic crystal waveguides

A modern strategy to control the propagation of light is the use of photonic crystal architectures. These 'materials' are made of periodic arrangements of dielectric materials, where the arrangement can be in one, two or three dimensions.

In order to explain the basic concepts of photonic crystals, we start with the simple case of the so-called Bragg stack, which is a stack of different

---

phase velocity (wave vector), group velocity and energy velocity (Poynting vector) of light in a ridge waveguide have all the same direction.

dielectrics layered with period a (Fig. 1.4A). Because of the periodicity of the system, light propagating through the structure has to obey the Bloch's theorem [1,17]. This theorem states that a light wave in a periodic medium can be described as a plane wave with wave vector k and amplitude modulated with the same period as the medium. This wave is called a Bloch wave and can be written as an expansion in plane waves

$$\Psi_k(y) = \sum_m c_{k,m} e^{\mathrm{i}(k+mG)y} = u_k(y)e^{\mathrm{i}ky}, \tag{1.2}$$

$$u_k(y) = \sum_m c_{k,m} e^{\mathrm{i}mGy} = u_k(y+a), \tag{1.3}$$

where m is an integer, $c_{k,m}$ is the amplitude of the m-th wave and $G = 2\pi/a$ is the reciprocal lattice vector. In other words, the spatial distribution of the wave changes according to the periodicity of the structure. Consequently, a Bloch wave can be described as an expansion in m Bloch harmonics. The m-th harmonic has a wave vector $k + mG$ and the zero-order harmonic ($m = 0$) is called the fundamental Bloch harmonic. In Fig. 1.4B the dispersion relation ($\omega(k)$) of a Bragg stack is shown. Let us consider a fixed angular frequency ω. As indicated by the dark gray dashed line in Fig. 1.4B, many (infinite) wave vectors compose the Bloch wave. For a certain frequency, which is indicated by the light gray dashed line, we notice that two harmonics should have the same wave vector $G/2 + mG$. This degeneracy in wave vectors is removed by the strong coupling between the forward and backward propagating mode (indicated by the diagonal dotted lines in Fig. 1.4B). Consequently, an avoided crossing occurs, as indicated by the black ellipses in Fig. 1.4B, and a frequency gap in which light cannot propagate through the Bragg stack is opened. This frequency window is called a bandgap (for further details see [17]). As the refractive index contrast becomes larger, the light-matter interaction and, thus, also the frequency (or energy) splitting increases. Analogous considerations are valid for periodic dielectric structures in two or three dimensions. The more dimensions one adds to these systems, the richer the optical properties that they exhibit [17].

In this thesis we investigate only 2D photonic crystal structures. Let us consider a dielectric slab as described in Section 1.2.1. By creating a periodic arrangement of holes in the slab, we create a system that is the 2D analogue of a Bragg stack (Fig. 1.4C). Besides many other interesting properties [17], this structure exhibits a 2D bandgap where no modes

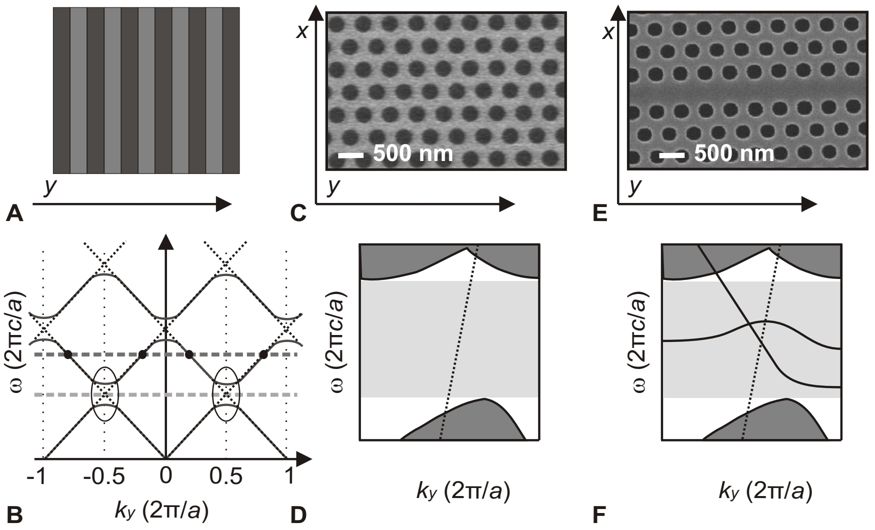

Figure 1.4:
A, *Schematic representation of a Bragg stack. Shades of gray represent different dielectric materials.* **B**, *Schematic representation of the dispersion diagram of a Bragg stack. The angular and spatial frequencies are normalized by $a/(2\pi)$ and $a/(2\pi c)$, respectively. The dark gray dashed line indicates a frequency with Bloch harmonics having different wave vectors. The light gray dashed line indicates a frequency which should have some of the Bloch harmonics with the same wave vectors. This degeneracy in wave vectors is removed by the strong coupling between the forward and backward propagating mode. Consequently, an avoided crossing of these two modes occurs. The ellipses show the avoided crossing of the dispersion lines (indicated by dotted lines). A bandgap is opened at this frequency.* **C** and **E**, *Scanning electron micrograph of a typical 2D photonic crystal and 2D photonic crystal waveguide, respectively. In Fig. 1.4E the waveguide channel is clearly visible.* **D** and **F**, *Schematic representation of the dispersion diagram along $\hat{y}$ of a 2D photonic crystal and 2D photonic crystal waveguide, respectively. The dotted lines represent the light line ($\omega = ck$). The light gray and dark gray areas indicate the 2D bandgap and the photonic crystal modes, respectively. In Fig. 1.4F the lines in the bandgap indicate the photonic crystal waveguide modes.*

for in-plane propagating light are available. In Fig. 1.4D the dispersion relation for a 2D photonic crystal is shown. The light gray area indicates the bandgap. A photonic crystal waveguide can be considered as a system where two 2D photonic crystals are placed in close proximity with a *line-defect*, which serves as a waveguide 'channel' for light (Fig. 1.4E). Light at frequencies corresponding to the bandgap is confined in the lateral directions by the photonic bandgap and in the vertical direction by total internal reflection (see also Chapter 3). Explaining all the fascinating properties of a photonic crystal waveguide [18] is beyond the scope of this thesis. However, we want to point out that new modes for propagating light along the line-defect ($\hat{y}$) are now available in the bandgap, as shown in Fig. 1.4F.

1.2.3 Photonic crystal cavities

In this Section we will show how light can be trapped in a photonic crystal. By placing two other photonic crystals at the extremities of a photonic crystal waveguide, light can be trapped in the line-defect. In this way, we can create a cavity that can be as small as two unit cells (a so-called *point-defect*). Many different designs have been proposed in order to increase the quality of the cavity [14, 19–21]. These designs generally aim to decrease the intrinsic out-of-plane radiation. In fact, it has been shown through Fourier analyses that the eigenmode of the nanocavity has some spatial frequencies which are not confined by total internal reflection [14], which results in a radiation which primarily skims along the surface of the sample (see Chapter 4). The number of these unbound wave vectors can be decreased by engineering the geometries of the cavity. Arguably the most important property of this type of cavities is their ability to confine light to a very small volume (comparable with the wavelength in matter cubed, $\sim (\lambda/n)^3$) for a very long time (up to a million oscillation periods) [20, 22]. In this nanocavity, the ratio between the quality factor Q and the mode volume V is extremely high. As a result, the cavity is particularly sensitive to environmental variations, such as the presence of a nano-object in its proximity or variations in the chemicals surrounding it, and could be used, e.i., for sensing applications[3].

In Chapter 4 and 5 we investigate an air-bridge 2D photonic crystal

---

[3] The employment of ultra-high-Q photonic crystal cavities are also extremely promising for quantum electrodynamic applications but this research of field is not part of the work described in this thesis.

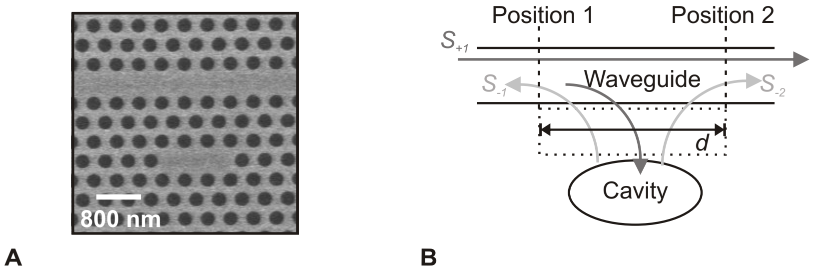

Figure 1.5:
A, *Scanning electron micrograph of a typical L3 photonic crystal cavity side-coupled to a photonic crystal waveguide.* **B**, *Schematic representation of cavity/waveguide system. The dark gray arrows represent the light (with electric field amplitude* S_{+1}*) that propagates into the waveguide and partially couples to the cavity. The light gray arrows indicate the light that leaks away from the cavity:* S_{-1} *and* S_{-2} *is the electric field amplitude of backwards and forward propagating light. The doted box show the area where the cavity mode and the waveguide mode overlap, d is the length of the box. Position 1 and 2 indicate the location related with* S_{-1} *and* S_{-2}*, respectively.*

nanocavity side-coupled to a photonic crystal waveguide. The silicon slab is 250 nm thick, the lattice constant of the holes is $a = 415$ nm and the holes diameter $b = 250$ nm. As shown in Fig. 1.5A, the cavity is formed by removing three holes and this cavity is separated by three rows of holes from the waveguide. In Fig. 1.5B a schematic representation of the waveguide-cavity system is depicted. Let us call g, S_{+1}, S_{-1} and S_{-2} the amplitudes of the cavity mode, of the incoming wave at position 1 of the access waveguide, of the outgoing wave at position 1 and of the outgoing wave at position 2, respectively. The equations describing the time evolution of g, S_{-1} and

S_{-2} are [23]

$$\frac{\mathrm{d}g}{\mathrm{d}t} = (\mathrm{i}\omega_o - \frac{1}{\tau_{in}} - \frac{1}{\tau_v})g + \sqrt{\frac{1}{\tau_{in}}}e^{-\mathrm{i}kd/2}S_{+1}, \tag{1.4}$$

$$S_{-1} = -\sqrt{\frac{1}{\tau_{in}}}e^{-\mathrm{i}kd/2}g, \tag{1.5}$$

$$S_{-2} = e^{-\mathrm{i}kd}\left(S_{+1} - \sqrt{\frac{1}{\tau_{in}}}e^{-\mathrm{i}kd/2}g\right), \tag{1.6}$$

where $1/\tau_{in}$ is the so-called in-plane decay rate, which is only due to the coupling with the access waveguide, and $1/\tau_v$ is the so-called out-of-plane decay rate, which describes the loss of the cavity (intrinsic out-of-plane radiation, roughness and imperfection of the cavity). Here, k is the wave vector of light in the waveguide and d is the length of the area where the cavity mode and the waveguide mode overlap (Fig. 1.5B). From the equation that relates the quality factor of the cavity with the ring down time $1/Q = 2/(\omega_o\tau)$, we infer that $1/Q = 2/(\omega_o\tau_{in}) + (2/\omega_o\tau_v) = 1/Q_{in} + 1/Q_v$, where Q_{in} and Q_v are the so-called in-plane and vertical quality factor of the cavity, respectively. The complex transfer function of the system is given by the ratio between the amplitude of the outgoing wave at position 2 and of the incoming wave at position 1

$$T = \frac{S_{-2}}{S_{+1}} = e^{-\mathrm{i}kd}\left(1 - \frac{\frac{\omega_o}{2Q_{in}}}{\mathrm{i}(\omega - \omega_o) + \frac{\omega_o}{2Q_{in}} + \frac{\omega_o}{2Q_v}}\right), \tag{1.7}$$

which can be consider as the difference between "perfect transmission" and a transmission described by a Lorentzian function centered at the resonance frequency of the cavity.

1.3 Singular Optics

As mentioned in Section 1.2.2, the strong light-matter interaction occurring in photonic crystals leads to multiple reflections of light propagating through the periodic structure. In a photonic crystal waveguide, the interference between these reflected waves leads to a complicated field distribution. Moreover, in a photonic crystal waveguide the strong confinement results in pronounced transverse components of the wave vectors (see Section 1.2.1). The longitudinal component of the electric field can therefore be as strong as the transverse component (see Chapter 3), giving rise to a 3D polarization state. Systems where many light waves interfere and generate complicated field distributions are intriguing candidates for investigating wave singularities [24–28]. A wave singularity occurs at locations where one of the parameters that define an complex field is ill-defined. These singularities appear in every type of waves and, thus, their role is important in many different area of science, such as chemistry, oceanography, seismology, medicine, biology, etc.. Singularities in optical fields are investigated by singular optics.

The scope of this Chapter is not to give an exhaustive overview of the entire broad field of singular optics. Here, we will rather provide only the basic concepts necessary for a clear understanding of the following chapters.

In optics, the most common types of wave singularities are phase singularities and polarization singularities.

1.3.1 Phase singularities

Phase singularities, or dislocations, are associated with scalar fields. Let us consider a complex scalar wave field $\Psi(x, y, z) = |\Psi(x, y, z)|\mathrm{e}^{\mathrm{i}\phi(x,y,z)}$. A phase singularity occurs at positions where the real and imaginary part of $\Psi(x, y, z)$ are zero and the phase cannot be defined. It turns out that a point can only have $\mathrm{Re}(\Psi(x, y, z)) = \mathrm{Im}(\Psi(x, y, z)) = 0$ when the phase around a dislocation changes $2\pi s$, where $s \in \mathbb{Z}$. Every phase singularity is therefore characterized by a topological charge s, given by

$$s = \frac{1}{2\pi}\oint_l \mathrm{d}\phi, \tag{1.8}$$

where l is a closed curve that encloses the dislocation. The sign of s is positive if the phase increases in the counterclockwise direction. In Fig.

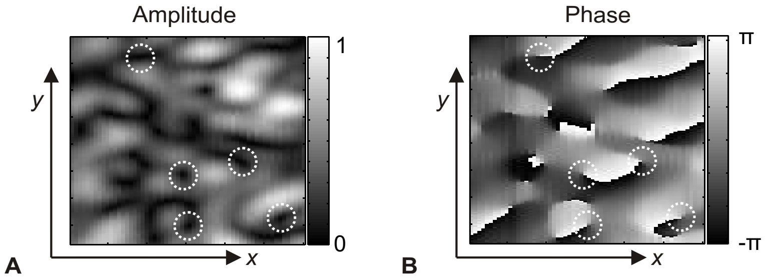

Figure 1.6:
A and **B**, *Typical amplitude and phase distribution of a measured speckle pattern. The amplitude is normalized to the maximum and the phase ranges between* $-\pi$ *and* π*. The dashed circles indicate the position of some of the phase singularities. Measurement related with [29].*

1.6A and B the measured amplitude and phase of a speckle pattern is shown [29]. As indicated by the dashed circles, a phase singularity occurs only where the amplitude of the field is zero. It is clear that the phase of the detected field changes 2π around a phase singularity and thus $s = \pm 1$.

The topology of the phase distribution is fully determined by the dislocations. In fact, all the equiphase lines, which are lines with constant ϕ, converge on phase singularities [28], fixing the phase distribution. In principle, by knowing the position and topological charge of every dislocation, we could reconstruct the phase distribution of the scalar field. A detailed classification of all the possible dislocations is presented by J. F. Nye in [27].

Because dislocations can be present in any scalar complex field, the above considerations also hold for the three components of the electric and magnetic field of light. Due to the difficulties in measuring the magnetic field at optical frequencies, no experimental observation of phase dislocations for the magnetic components of light has been observed so far. In contrast, many investigations of phase singularities in the electric field distribution have been performed, especially in random fields [29–36]. Due to the complicated field distribution present in and around photonic nanostructures, nowadays a new interest for the observation of phase singularities in the near field is arising [29].

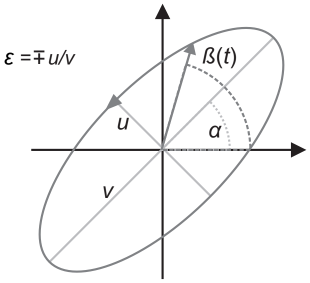

Figure 1.7:
The polarization ellipse which describe the polarization state. The parameter ε indicates the eccentricity, α the orientation of the major axis, u and v are the semi-axes and $\beta(t)$ is the instantaneous angle of the vector electric field. The handedness of the polarization is described by the sign of ε.

1.3.2 Polarization singularities

Polarization singularities are singularities associated with the vectorial nature of the electric field of light. It is important to immediately point out that a polarization singularity is not a singularity in the polarization state. The polarization of light is always well defined for every point of the light field. In contrast to a scalar field, in which dislocations occur where the amplitude of the field is zero, in a vector field a position (x_o, y_o) where $\boldsymbol{E}(x_o, y_o, t) = 0$ at all times does not exist (excluding the trivial case of zero electric field at all locations). In other words, the dislocations of the scalar components of $\boldsymbol{E}$ (e.g. E_x and E_y) never occur at the same position. In contrast, the electric field can be instantaneously zero ($\boldsymbol{E}(x_o, y_o, t_o) = 0$), giving rise to a time-varying polarization singularity, as we will show in the following. In Fig. 1.7 the polarization ellipse is shown, where u and v are the minor and major semiaxis, respectively [8]. This ellipse is defined by its eccentricity, described by the parameter $\varepsilon = \mp u/v$, the orientation of the major axis, which is indicated by the angle α, and the handedness, that is described by the sign of ε and indicates how the vector electric field rotates in time. A polarization singularity is the occurrence of one of these three parameters being ill-defined [27]. In a light field where the polarization is a function of position, we can define three types of polarization singularities:

two are time-independent and one is time-dependent.

Let us start with the first class. When the two components of the electric field oscillate $\pi/2$ out of phase and with the same amplitude the polarization is circular. In such a case the orientation of the polarization state is undetermined because the ellipse in Fig. 1.7 becomes a circle and a major axis cannot be defined. These polarization singularities are spatially arranged in points (or lines) called C-points (or C-lines) in 2D (or 3D) systems. In analogy to phase singularities, C-points are characterized by a topological charge I, that is

$$I = \frac{1}{2\pi} \oint_{l} \mathrm{d}\alpha, \tag{1.9}$$

where l is a closed curve that enclose the C-point. Similarly to the scalar dislocation case, the sign of I is positive if α increases in the counterclockwise direction. In contrast with phase singularities, I is always half an integer, because $\alpha \in [0; \pi]$. Figures 1.8A, B and C show the main three types of C-points, namely *star* (I=-1/2), *monstar* (I=+1/2) and *lemon* (I=+1/2) which are also classified according to the orientation of the ellipses around them (*line classification*). The lines in Fig. 1.8 indicate the orientation of the polarization ellipse. The difference between monstar and lemon is given by the number of straight lines, indicated by the light gray lines, that converge on the C-point. The first has always three straight lines, whereas the second only one [28].

A C-point can be considered as a particular type of scalar dislocation. Any polarization state can be described as the linear superposition of two circular polarizations (A_1 and A_2) with opposite handedness. Because in a C-point the polarization must be circular, either A_1 or A_2, depending on the handedness of the C-point, must be zero. Hence, in analogy with the scalar dislocation, the C-point is a dislocation in one of the two circular polarization components.

The second type of time-independent polarization singularity occurs when the handedness is not defined. This is the case of points of linear polarization that in 2D (or 3D) system are spatially arranged in L-lines (or L-surfaces) [27]. These lines separate two areas of opposite handedness. Note that, although the polarization along L-lines is linear, the orientation α along these lines varies.

The time-dependent polarization singularities are the so-called disclinations. A disclination occurs when all components of the vector electric field

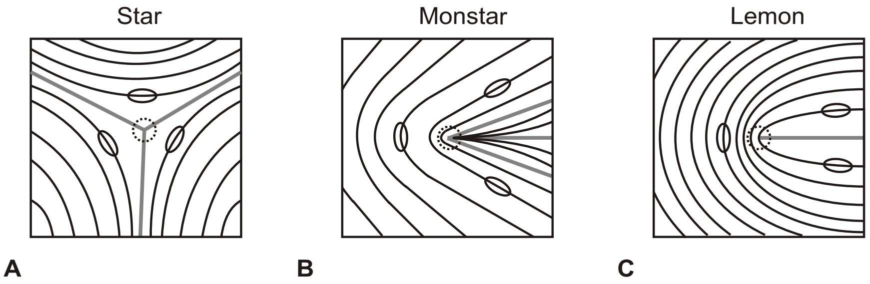

Figure 1.8:
The three types of C-points. The light gray lines are the straight lines that characterize these points. The ellipses indicate the orientation of the polarization ellipse around the singularity. **A**, Star-type. *There are three straight lines. The orientation of the ellipse changes around the C-point in the counterclockwise direction (I=-1/2).* **B**, Monstar-type. *There are three straight lines. The orientation of the ellipse changes around the C-point in clockwise sense (I=1/2).* **C** Lemon-type. *There is only one straight line. The orientation of the ellipse changes around the C-point in clockwise sense (I=1/2).*

vanish. A disclination, whose position is a function of time $(x_o(t), y_o(t))$, is an instantaneous singularity in the polarization state. Because an instantaneous zero of the electric field occurs only when the polarization is linear, a disclination lies on L-lines and moves along them as time progresses. The topological charge H for this singularity is

$$H = \frac{1}{2\pi} \oint_l \mathrm{d}\beta, \tag{1.10}$$

where $\beta(t)$ is the instantaneous orientation of the vector electric field around the disclination and H turns out to be an integer. An interesting property of disclinations is that generally the vector field distribution around it cyclicly changes as time progresses[4] [27].

---

[4] In Chapter 3 we will show that in a photonic crystal waveguide this is not necessarily the case.

1.3.3 Concluding remarks on wave singularities

In recent years, interest in singular optics has increased. This has a twofold cause. Firstly, the remarkable interdisciplinary aspects of wave singularities. Because in science physical phenomena are primarily described by waves, the investigation of wave singularities attracts the interest of a broad audience. Studies on optical singularities, that can be performed in a laboratory, could help in the understanding of natural phenomena in fields of science where experimental conditions are more demanding. A striking example is given by the tidal theory. The science that studies the motion of the tides has a strong link with singular optics. The so-called amphidromic points, position on Earth where the height of the tide is constantly zero, are phase singularities of the complex wave function that describe the tides motion [37]. However, the analogies between optics and the tides is not only for scalar fields but also vectorial. Strong similarities have been found between polarization singularities and the currents induced by tides [38]. Phase singularities, named as 'rotors', also seem to have a crucial role in cardiac fibrillations [39]. Disclinations and dislocations appear in the distribution of liquid crystals [40]. Therefore, a better understanding of topological properties of optical singularities can be useful in many fields of science.

Secondly, the possible applications in optics itself. Phase singularities are related to the orbital angular momentum of light beams. It has been shown that a linearly polarized laser beam with an angular gradient in the phase distribution, for instance a beam with a 'donut' shape, carries an orbital angular momentum orthogonal to the gradient [41]. Such a gradient in the phase distribution occurs around a phase singularity (Fig. 1.6) and, thus, the orbital angular momentum associated can be transferred to micro- and nano-objects [42]. It is important to point out that a phase singularity does not carry any angular momentum because it coincides with a zero of the intensity of the field. However, around the singularity, where the intensity is maximum, the Poynting vector flows circularly, creating an optical vortex. Similarly, polarization singularities can be related to spin angular momentum. Such an angular momentum is carried, for instance, by a circularly polarized laser beam [43]. Hence, the investigation of the polarization topology of complicated light fields where the polarization state is a function of position can be useful for applications in quantum system, where one wants to transfer spin states to quantum objects, such as atoms or molecules [44]. Moreover, the two angular momenta can be simultaneously transferred to particles using a circularly polarized donut-shaped beam, as shown in [45].

1.4 Near-field optics

Investigations of the optical properties of photonic nanostructures, for example singular optical properties, requires a very high resolution [3]. Unfortunately, according to the theory developed by Rayleigh in 1879, a monochromatic light field with wavelength λ cannot be focused more than a spot of diameter $\sim \lambda/2$ (the *diffraction limit*) [8]. Therefore, the resolution of an optical microscope is limited by this condition and many of the intriguing optical properties of photonic nanostructures remain hidden by the diffraction barrier. Near-field optics has been developed to beat the diffraction limit. In order to understand what the added value provided by near-field microscopy is, we first consider a light wave with a spatial distribution along the xy-plane $f(\mathbf{r}_{||})$ with a width $\Delta\mathbf{r}_{||}$, where $\mathbf{r}_{||} = \sqrt{x^2 + y^2}$. Through Fourier mathematics it is possible to show that

$$\Delta\mathbf{r}_{||} \cdot \Delta k_{||} \geq 1, \tag{1.11}$$

where $\Delta k_{||}$ is the spread of the wave vectors of $f(\mathbf{r}_{||})$ along the xy-plane [3]. The equality of eq. 1.11 holds when $f(\mathbf{r}_{||})$ is a Gaussian function. In order to obtain a high spatial resolution a large number of wave vectors must be employed. Let us now consider a collimated monochromatic laser beam $E(z,t) = E(t)e^{\mathrm{i}zk}$ propagating along $\hat{z}$ which is focused by an objective. The magnitude of the wave vector after the objective is given by $k = \sqrt{{k_{||}}^2 + {k_z}^2}$ and, thus, $k_z = \sqrt{k^2 - {k_{||}}^2}$, where $k_{||}$ is the transverse component of the wave vector and is determined by the numerical aperture (NA) of the objective. To decrease the spot size of the focus and obtain a high resolution the magnitude of $k_{||}$ should be increased. However, the parallel transverse component of the wave vector cannot be indefinitely increased. When $k_{||}$ becomes larger than k, the longitudinal component k_z becomes imaginary and, therefore, the wave exponentially decays. Hence, wave vectors with $k_{||} > k$ cannot be detected in the far field and we obtain that the upper limit for $\Delta k_{||}$ is $k = 2\pi\mathrm{n}/\lambda$. Therefore, eq. 1.11 for a Gaussian function $f(\mathbf{r}_{||})$ the maximum achievable resolution is

$$\Delta\mathbf{r}_{||} = \frac{1}{k}. \tag{1.12}$$

Taking in consideration that an objective can focus the laser beam with a maximum angle $\theta_{\max}$ (NA $= n \sin\theta_{\max}$), we obtain $k = (2\pi\mathrm{n}\sin\theta_{\max})/\lambda$

and the 'ideal' diffraction limit is retrieved from eq. 1.12

$$\Delta \mathbf{r}_{||} = \frac{1}{2\pi}\frac{\lambda}{\mathrm{NA}}. \tag{1.13}$$

Equation 1.13 is similar to the Rayleigh diffraction limit

$$\Delta \mathbf{r}_{||} = 0.6098\frac{\lambda}{\mathrm{NA}}, \tag{1.14}$$

which is more accurate for practical purposes [3].

Near-field optics reaches resolutions beyond the diffraction limit by coupling also those wave vectors for which $k_{||} > k$ [3]. Near-field optics has been first envisioned in 1928 by Singe [46], who proposed to place a subwavelength hole in an opaque screen close to the investigated sample such that a very small area is illuminated (Fig. 1.9). After the first experimental verification performed in the microwave regime in 1972 by Ash and Nicholls [47], near-field microscopy also reached optical frequencies and nowadays is a crucial tool for nano-optics (for a historical background see [3]). Nowadays, the opaque screen has been replaced by a so-called near-field probe (see Section 2.1). This probe can be used in either illumination or in collection mode [3, 48]. In the first case, the apex of the probe is used as a subwavelength source of radiation. In the second case the apex acts like a subwavelength detector. In both cases the probe is kept in close proximity of the investigated specimen, by controlling the separation with an electronic feedback loop [49, 50]. The near field of both probe and sample is characterized by a broad spatial frequency distribution, because the evanescent fields there have a nonvanishing contribution. The large wave vectors ($k_{||} > k$) of the probe and sample couple and generate a propagating wave with wave vector given by the difference between them, as shown in [3]. The process can also be considered as the optical classical analogue of tunneling in quantum mechanics. Because in the gap between the probe and the sample the light field is evanescent, this area acts as a barrier for light which can tunnel through it (see Fig. 1.9B) [3]. The above described mechanism occurs for both illumination (light gray arrows in Fig. 1.9B) and collection mode (dark gray arrows in Fig. 1.9B). In the work described in this thesis the probe is always used in collection mode.

The high resolution of near-field microscopy has a two-fold high cost. Firstly, the low throughput of these probes makes light detection a challenging task. Nowadays, this issue is solved with a large variety of solutions but

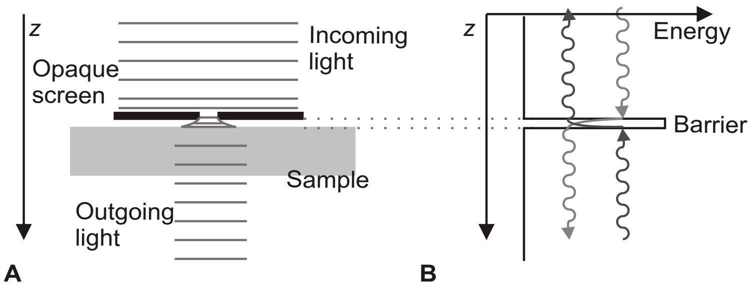

Figure 1.9:
A, *Schematic representation of Singe's idea. An opaque screen (black), which stops the light, is placed in close proximity of the investigated sample. Through a subwavelength hole in the screen the light can reach the sample and illuminate it with a subwavelength spot.* **B**, *Singe's idea in a 'quantum mechanics picture'. Light propagating in vacuum (upper part of the figure) impinges on the barrier (screen-sample gap). Inside the barrier the light exponentially decays. However, light tunnels through the barrier with a finite amplitude in the lower part of the figure.*

the most powerful is the heterodyne detection schemes (see Section 2.2). Secondly, the probe is so close to the sample that the interaction between the two might not be negligible. In contrast to far-field microscopy where interaction with the investigated sample does not occur, a near-field probe can drastically change the optical properties of the studied structure [51]. Because the degree of interaction depends on the optical properties of the sample, after any near-field experiment it is crucial to investigate the relevance of this coupling. When the polarizability of the probe is known (see Section 2.1), this interaction can be exploited to investigate novel phenomena at the nanoscale (see Chapter 4).

A near-field microscope is particularly useful for investigating 2D photonic structures, such as 2D photonic crystals [52] and plasmonic structures [53]. In far-field investigations generally the optical properties of photonic materials are inferred by comparing transmission and reflection spectra of different types of samples [54]. In contrast, near-field optics directly visualizes how light behaves inside the investigated sample, providing a new insight in the optical properties of the photonic structures [13, 55–57].

Chapter 2

Microscope & Probes

Arguably the most important part of a near-field microscope is the employed near-field probe. In this chapter, we discuss the electric and magnetic response of three different types of probe. A novel insight in the optical properties of photonic nanostructures is achieved by combining a homemade near-field microscope with a Mach-Zehnder interferometer. Here, we provide an brief introduction to interferometry and to the main characteristics of our setup.

2.1 Optical response of near-field probes

Near-field microscopy overcomes the diffraction limit and obtains images with subwavelength resolution by exploiting the interaction between a subwavelength object (the probe) and the evanescent field of light (see Chapter 1). Hence, in order to reconstruct the actual field distribution that we investigate, a detailed knowledge of the optical properties of the probe is necessary. Because the near field of photonic nanostructures is often characterized by a complicated distribution of the six fields (three for both electric and magnetic field) and due to the geometries of the probes, this is a challenging task. To describe the light-probe interaction the end of the probe is generally approximated with an appropriately chosen subwavelength object, of which the optical properties are well known.

Let us consider an object with linear dimension a embedded in an electromagnetic field with wavelength λ. This field induces a current density distribution $\boldsymbol{J}$ in the object. In the quasi-static limit ($a \ll \lambda$) [5] the response of the object to the electromagnetic wave can be described by the lowest multipole moments of $\boldsymbol{J}$ as

$$\boldsymbol{p} = \frac{1}{i\omega}\int_V \boldsymbol{J}\mathrm{d}^3x = \frac{1}{i\omega}\int_V (\boldsymbol{J}_e + \boldsymbol{J}_m)\mathrm{d}^3x, \tag{2.1}$$

$$\boldsymbol{m} = \frac{1}{2}\int_V (\mathbf{x}\times\boldsymbol{J})\mathrm{d}^3x = \frac{1}{2}\int_V (\mathbf{x}\times(\boldsymbol{J}_e + \boldsymbol{J}_m))\mathrm{d}^3x, \tag{2.2}$$

where ω is the angular frequency of light, V is the volume of the object and $\boldsymbol{p}$ and $\boldsymbol{m}$ are the electric and magnetic dipole moments, respectively [2]. Here, the current density is written as $\boldsymbol{J} = \boldsymbol{J}_e + \boldsymbol{J}_m$, where $\boldsymbol{J}_e$ and $\boldsymbol{J}_m$ are the current densities induced by the electric and magnetic field of light, respectively [58]. Apart from simple geometries, eq. 2.1 and 2.2 are generally solved by numerical calculations.

Equation 2.1 and 2.2 can also be expressed in a matrix formalism. In general the two dipole moments are proportional to the driving fields. The proportionality constants are given by the so-called 6×6 generalized polarizability matrix $\underline{\underline{\alpha}}$

$$\begin{bmatrix}\boldsymbol{p}\\ \boldsymbol{m}\end{bmatrix} = \underline{\underline{\alpha}}\cdot\begin{bmatrix}\boldsymbol{E}\\ \boldsymbol{B}\end{bmatrix} = \begin{bmatrix}\underline{\underline{\alpha}}^{ee} & \underline{\underline{\alpha}}^{em}\\ \underline{\underline{\alpha}}^{me} & \underline{\underline{\alpha}}^{mm}\end{bmatrix}\cdot\begin{bmatrix}\boldsymbol{E}\\ \boldsymbol{B}\end{bmatrix}, \tag{2.3}$$

where $\underline{\underline{\alpha}}^{ee}$ and $\underline{\underline{\alpha}}^{mm}$ are the 3×3 electric and magnetic polarizability matrices, respectively. Here, $\underline{\underline{\alpha}}^{em}$ and $\underline{\underline{\alpha}}^{me}$ are the so-called cross-polarizability matrices. These 3×3 matrices describe the magnetically induced electric polarizability and the electrically induced magnetic polarizability, respectively.

The matrix $\underline{\underline{\alpha}}$ describes how the object becomes polarized and magnetized by an electromagnetic field. For homogenous materials at optical frequencies, the only non-negligible matrix is $\underline{\underline{\alpha}}^{ee}$. This is due to the fact that light-matter coupling is governed by electric interactions rather than magnetic (see Chapter 1). As a result, generally $\underline{\underline{\alpha}}^{em}$, $\underline{\underline{\alpha}}^{me}$ and $\underline{\underline{\alpha}}^{mm}$ either vanish or are negligible with respect to $\underline{\underline{\alpha}}^{ee}$. In the next sections we will provide the polarizability tensors for some of the most common near-field probe and show how this matrix changes as a function of the geometry of the probe itself.

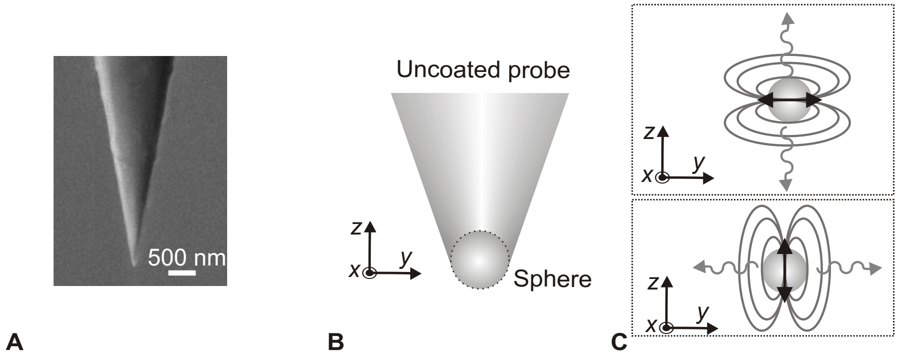

Figure 2.1:
A, *Scanning electron micrograph of a state-of-the-art tapered optical fiber near-field probe, a so-called uncoated probe. The image is a courtesy of F. Intonti. The apex of the probe is* ~ 70 *nm.* **B**, *Schematic representation of an uncoated probe. The apex of the probe is approximated by a dielectric sphere.* **C**, *Schematic representation of the radiation emitted by the in-plane (xy-plane in the upper part) and out-of-plane (yz-plane in the lower part) dipole moment of the dielectric sphere.*

2.1.1 The uncoated near-field probe

The most widespread near-field probe is a tapered optical fiber, shown in Fig. 2.1A. This probe can be obtained from an optical fiber either by etching process [59] or by heating and pulling the fiber [60]. The apex of such a probe is generally one order of magnitude smaller than the wavelength of light (typical radius of curvature is 70 nm) and it is generally approximated as a subwavelength dielectric sphere (Fig. 2.1B) [3, 51]. Due to the symmetry of the sphere, $\alpha^{ee}_{xx} = \alpha^{ee}_{yy} = \alpha^{ee}_{zz}$ are nonvanishing, whereas all the off-diagonal terms of $\underline{\underline{\alpha}}^{ee}$ are zero. This means that, an electric field oriented, for instance, along $\hat{z}$ cannot induce a dipole moment along $\hat{x}$ or $\hat{y}$. In this case, the light-probe interaction can be described by the diagonal polarizability matrix in which all the nonvanishing terms are $\alpha^{ee}_{ii} = \varepsilon_\mathrm{o} 3(\varepsilon_\mathrm{p} - 1)/(\varepsilon_\mathrm{p} + 2)V_p$, where ε_o is the electric permittivity of vacuum, ε_p is the dielectric constant of the probe and V_p is the volume of the sphere [2]. The induced in-plane (along the xy-plane) dipole moments couple to the propagating modes of the probe fiber and their emission can

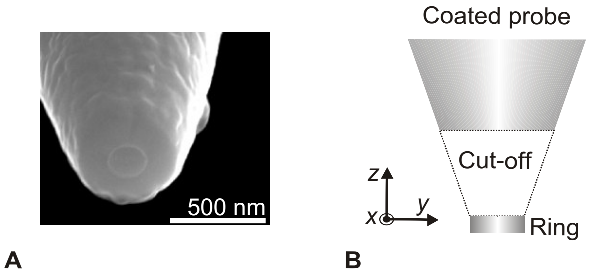

Figure 2.2:
A, *Scanning electron micrograph of a state-of-the-art aperture coated near-field probe. The thickness of the coating and the aperture diameter are in this case* ~ 150 *nm and* ~ 210 *nm, respectively.* **B**, *Schematic representation of a coated probe. The apex of the probe is approximated by a metallic ring. The dashed area indicates a cut-off volume where light propagation is forbidden. The upper part of the probe indicates the volume where propagating modes are available.*

be detected at the end of the fiber (upper part of Fig. 2.1C). The induced out-of-plane (along $\hat{z}$) dipole moment cannot couple to the fiber because the radiation is mainly in-plane (lower part of Fig. 2.1C).

The use of such a probe is not always convenient. The dimension of the apex can be very small but the achievable resolution is affected also by far-field radiation that can be collected far from the tip of the probe. This reduces the achievable resolution of the probe. Moreover, because the collected far-field and near-field waves interfere at the detector, the interpretation of the retrieved near-field image can be rather complicated.

2.1.2 The coated near-field probe

In order to alleviate the problem raised in the previous section, a different type of probe is often employed in near-field microscopy, the so-called aperture probe. A typical example of a metal-coated near-field probe is shown in Fig. 2.2A. The coating, which is deposited by evaporation onto an uncoated probe, is generally made of aluminum with a thickness of $100-200$ nm. An aperture is created at the end of the probe by focused ion beam milling [61]. With such a coating the sides of the probe are shielded and light is collected only through the aperture. Unfortunately, these probes have a throughput of the order of only 10^{-4} or less [3]. There are two main reasons of such a low throughput. Firstly, the absorption of the metal coating. Secondly, due to the coating and the taper of the fiber, light experiences cut-off in the probe. Let us assume that light propagates in the fiber towards the apex. The metal around the tapered fiber progressively confines the light in the probe. However, light cannot be squeezed infinitely in this system. For a specific diameter of the probe, light cannot propagate any further and is back reflected or absorbed by the metal [3]. This leads to a forbidden volume of the probe where the field decays exponentially. Light can reach the apex of the probe with a process that is the classical optical analogue of tunneling in quantum mechanics, albeit with an additional decay due to absorption [3]. A reverse mechanism occurs when light is coupled through the aperture to the fiber. In order to deal with the low throughput and increase the signal-to-noise ratio, modern near-field microscopes are combined with lock-in detection schemes [62, 63], as also shown in sect. 2.2.

The polarizabilty matrix $\underline{\underline{\alpha}}$ of a coated probe is more complicated than the polarizability of the uncoated probe. For several years the complexity of $\underline{\underline{\alpha}}$ of the coated probe has been a severe limitation for the interpretation of near-field experiments. Much effort was spent in investigating both theoretically and experimentally the optical response of such a probe and an interesting scientific debate on what was the best model that describes a coated probe was opened [64–67]. The goal of this thesis is to present our contribution to arguably the most important discussion in near-field optics, that is, the light-probe coupling.

We will show that a coated aperture probe exhibits not only an electric but also a magnetic response. This magnetic response is evident if we compare the coated probe with a metallic hollow cylinder [68]. A time-varying magnetic field oriented along the axis of such a cylinder induces a circular current in the metal. This current, in turn, produces a magnetic field that suppresses the total field inside the cylinder. In short, the probe exhibits a nonvanishing magnetic dipole moment.

In order to calculate the magnetic polarizability, we model the apex of the probe as a metallic ring. In Fig. 2.2B we show the schematic representation of an aperture near-field probe. The dashed lines indicate the cut-off region where only evanescent fields are allowed. In analogy with the sphere

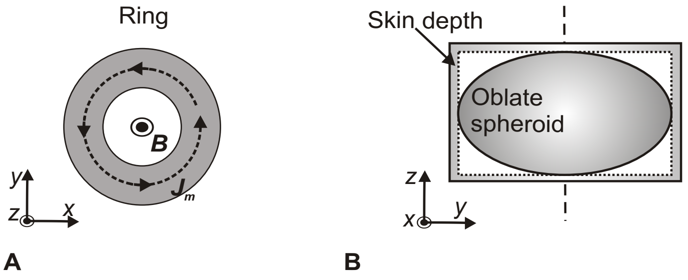

Figure 2.3:
A, *Schematic representation of the metallic ring in a time-varying magnetic field. The magnetic field is along* $\hat{z}$*. The magnetically induced current density* $\boldsymbol{J}_m$*, indicated by a dashed circle, is symmetrically distributed.* **B**, *Schematic representation of the model employed to retrieve the electric polarizability of the ring. The effective ring (dashed box) takes in consideration the skin depth of the metal. The spheroid approximates the effective ring.*

of the uncoated probe (see Section 2.1.1) this ring acts as a nano-object that couples light to the propagating modes of the fiber, which is shown in the upper part of the image. A magnetic field oriented along $\hat{z}$ induces an out-of-plane magnetic dipole moment $m_z = AI_m$ in the cylinder [2], where A is the total area enclosed in the ring, $I_m = J_m V_r$ is the magnetically induced current (Fig. 2.3A) and V_r is the volume of the ring. The current I_m can be described by applying Faraday's law. The electromotive force $\varepsilon_{\mathrm{emf}}$ is

$$\varepsilon_{\mathrm{emf}} = -\frac{\mathrm{d}}{\mathrm{d}t}\Phi - L\frac{\mathrm{d}}{\mathrm{d}t}I_m, = I_m R \tag{2.4}$$

where Φ is the flux of the incident magnetic field B_z and L and R are the self-inductance and the complex resistance of the coil, respectively. Because B_z is orthogonal to the ring, the flux is $\Phi = AB_z e^{-\mathrm{i}\omega t} = AB_z(t)$, where ω is the angular frequency of the magnetic field. Equation 2.4 becomes

$$L\frac{\mathrm{d}}{\mathrm{d}t}I_m + I_m R = \mathrm{i}\omega AB_z(t). \tag{2.5}$$

Equation 2.5 is a first order differential equation with solution

$$I_m = -\frac{AB_z(t)}{(L + \frac{\mathrm{i}R}{\omega})}. \tag{2.6}$$

Because in the case of a subwavelength coil $m_z = \alpha_{zz}^{mm} B_z(t)$ [68], we find that

$$\alpha_{zz}^{mm} = -\frac{A^2}{(L + \frac{iR}{\omega})}. \tag{2.7}$$

Hence, a magnetization of the probe can be achieved at optical frequencies exploiting the geometry of the cylindrical coating. For the specific probe used in Chapter 4, we calculated the resistance $R = \rho l/S \approx (11 - \mathrm{i}60)$ Ω, where ρ is the resistivity of aluminum at 200 THz, l is the average circumference of the ring and S is the cross-section of the coating. The self-inductance $L = 1.2 \cdot 10^{-13}$ H has been integrated numerically using a methodology found in [69] and we obtain from eq. 2.7 that $\alpha_{zz}^{mm} \approx -80 + \mathrm{i}4 \cdot 10^{-15}$ m^4/H. Note that the real part of the magnetic polarizability $\mathrm{Re}(\alpha_{zz}^{mm})$ is negative. Moreover, $\mathrm{Im}(\alpha_{zz}^{mm})$, which describes the absorption of the ring, is one order of magnitude smaller than $\mathrm{Re}(\alpha_{zz}^{mm})$. These are interesting characteristics of the coated probe that will be crucial in the experiment presented in Chapter 4. It is also important to note that a magnetic response of the constituent materials, namely glass and aluminum, is virtually absent and the effective magnetic response is only induced by the geometry of the probe.

The other two diagonal terms of the polarizability matrix, namely α_{xx}^{mm} and α_{yy}^{mm}, can be considered to be negligible. In fact, due to the small extension of the evanescent field ($\sim$ 100 nm) and the minute penetration of light inside the coating, the flux of the in-plane components of the magnetic field is negligible with respect to the flux of the out-of-plane component. As in the case of the dielectric sphere in Section 2.1.1, the off-diagonal terms of $\underline{\underline{\alpha}}^{mm}$ are zero because of the symmetry of the probe. Thus, $\underline{\underline{\alpha}}^{mm}$ has only one nonvanishing term, i.e. α_{zz}^{mm}.

It is possible to show that the cross-polarizability matrices are zero. By comparing eq. 2.1 and 2.2 with eq. 2.3, we conclude that $\int_V \boldsymbol{J}_m \mathrm{d}^3x$ is proportional to $\underline{\underline{\alpha}}^{em}$. The integration of the current distribution over the ring volume is zero. In fact, due to the symmetry of the ring the charges flow on one part of the ring in opposite direction with respect to the part diametrically opposed, as shown in Fig. 2.3A, and, thus, the net current is zero. As a consequence, $\underline{\underline{\alpha}}^{em}$ vanishes. From symmetry consideration we conclude that $\underline{\underline{\alpha}}^{me}$ is also zero. Because a magnetic field cannot induce an electric dipole moment, an electric field cannot generate a magnetic dipole moment. Hence, both cross-polarizability matrices are zero.

Given the cylindrical symmetry of the probe, we obtain $\alpha_{xx}^{ee} = \alpha_{yy}^{ee} \neq \alpha_{zz}^{ee}$. The analytical calculation of these three terms is a rather challenging task. In Chapter 4 we will approximate the ring with a perfect metallic oblate spheroid, as schematically shown in Fig. 2.3B, and use the calculation for the diagonal electric polarizabilty matrix presented by Landau and Lifshitz [5]. The analytical expression of the diagonal terms of the electric polarizability for an oblate spheroid with the short axis along $\hat{z}$ is $\alpha_{ii}^{ee} = \varepsilon_0 V/N_i$, where V is the volume of the spheroid and the label i indicates x, y or z. Here, the so-called depolarizing factors N_i are

$$N_z = \frac{1+e^2}{e^3}(e - \tan^{-1} e), \tag{2.8}$$

$$N_x = N_y = \frac{1-N_z}{2}, \tag{2.9}$$

where e is the eccentricity of the oblate spheroid. Because we are working at optical frequencies, the metal of the ring cannot be considered as perfect. In fact, the electric field penetrates into the metal as much as the skin depth in aluminum, which is ~ 10 nm at 200 THz. In order to obtain a better model, in Chapter 4 we will approximate the ring with a perfect ellipsoid of a smaller dimension to take in consideration the skin depth of the metal (Fig. 2.3B). We obtain for the specific geometry of the probe employed in Chapter 4 $\alpha_{xx}^{ee} = \alpha_{yy}^{ee} \approx 4 \cdot 10^{-32}$ Fm^2 and $\alpha_{zz}^{ee} \approx 7 \cdot 10^{-33}$ Fm^2.

We will show in Chapter 4 that this model is a good approximation when we use the probe as a 'perturbative' object. However, this model cannot be used to describe how light is collected by a coated probe. In this case we also have to consider the presence of the aperture, through which light is coupled to the fiber. As a consequence, $\underline{\underline{\alpha}}^{ee}$ is not diagonal. Let us consider the ring in an in-plane electric field, e.g., E_y. As in the case of a hole in a metallic screen [67], out-of-plane electric field components (E_z) at the edges of the ring are generated due to the scattering of E_y, as shown in Fig. 2.4A. This effect has been experimentally proven in single molecule investigations [70, 71]. Therefore, α_{zx}^{ee} and α_{zy}^{ee} are not zero. Similarly to the case of the magnetic response of the ring, these out-of-plane electric dipole moments cannot couple to propagating modes in the fiber and, thus, their contribution to the detected field is zero. Due to the symmetry of the problem, we expect that an out-of-plane electric field (E_z) generates in-plane electric components (E_x and E_y) at the edges of the ring, as shown

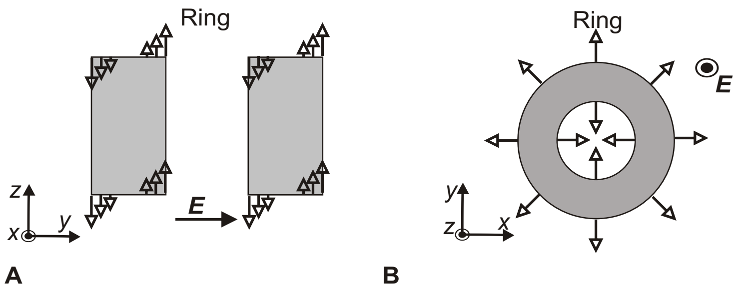

Figure 2.4:
Schematic representation of the metallic ring in a time-varying electric field. **A**, *Cross section of the ring in the zy-plane. The electric field is along $\hat{y}$. Arrows with an empty head represent the E_z electric field induced by the interaction between the metallic rim of the ring and E_y. The E_z close to the aperture does not couple to propagating modes in the fiber.* **B**, *Cross section of the ring along the xy-plane. The electric field is along $\hat{z}$. Arrows with an empty head represent the in-plane electric field induced by the interaction between the metallic edges of the ring and E_z. The in-plane electric fields inside the aperture cancel each other in the far field and, thus, their contribution to the detected optical signal vanishes.*

in Fig. 2.4B. As a result, α^{ee}_{xz} and α^{ee}_{yz} also would be nonvanishing. On the one hand, E_z would induce in-plane electric dipole moments that can couple to the fiber. On the other hand, when E_z is constant inside the aperture of the probe, the induced in-plane dipole moments should have opposite directions and interfere destructively (Fig. 2.4B). Hence, we expect the contribution of these E_z-induced in-plane electric dipoles to the detected field to be negligible.

In several experiments that we performed the actual dimension of the probe is $a = 2/3\lambda$ and, therefore, does not fulfill the condition of the quasi-static limit. A more rigorous approach would consider not only the lowest term of the dipole expansion in eq. 2.1 and 2.2, but also the higher terms. Unfortunately, the calculation of the quadrupole moment of a coated probe is a huge task, which has never been solved so far. Nevertheless, in this thesis we will show that a model for a coated near-field probe that takes in consideration only the first term of the dipole expansion adequately describes the light-probe interaction.

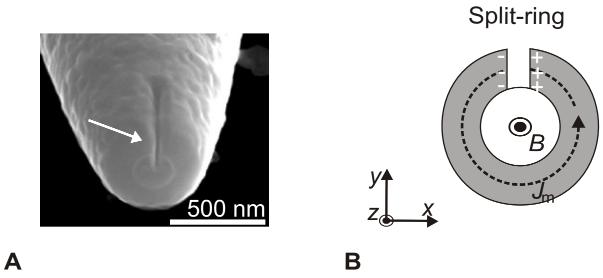

Figure 2.5:
A, *Scanning electron micrograph of a state-of-the-art aperture coated near-field probe with an air-gap in the coating (indicated by the arrow). We call it a split-probe. The thickness of the coating is* $\sim$ 150 *nm and the aperture diameter is* $\sim$ 210 *nm.* **B**, *Schematic representation of the metallic ring in a time-varying magnetic field. The magnetic field is along* $\hat{z}$. *The magnetically induced current* $\boldsymbol{J}_m$ *is indicated by a dashed circle. The symmetry of the current distribution is broken by the presence of the air-gap, where there is no conduction current. An oscillating dipolar charge distribution is generated at the edges of the air-gap.*

In Chapter 3 we will experimentally show that indeed a coated probe primarily couples to the probe fiber in-plane components of the electric field. This is due to the fact that the dipoles associated with α_{zz}^{ee}, α_{zx}^{ee}, α_{zy}^{ee} and α_{zz}^{mm} mainly emit in-plane radiation and the contribution of α_{xz}^{ee} and α_{yz}^{ee} to the detected field is small with respect to the optical signal due to α_{xx}^{ee} and α_{yy}^{ee}. In Chapter 4 we will prove that a coated probe interacts with the vertical component of the magnetic field and, thus, that α_{zz}^{mm} is nonvanishing. In this thesis there is no experimental proof that verifies our expectation for the response of the probe to E_z. However, experiments performed by Verhagen and co-workers [72] and Burresi and co-workers [in preparation] corroborate our interpretation.

2.1.3 The coated near-field split-probe

A novel type of probe has been used in the work described in this thesis. In Chapter 6 we perform near-field measurements with a split-probe. Such a probe has been obtained by opening an air-gap ($\sim$ 40 nm wide) in the coating of an aperture probe close to the apex (Fig. 2.5A). The end of the probe needs to be described as a split-ring resonator (SRR) [73], instead of a metallic ring. A SRR is a metallic nano-object that can resonantly respond to the magnetic and electric field at optical frequencies. The resonance ν_{SRR} and the width $\Delta\nu_{SRR}$ of a SRR can be approximately calculated in analogy to a RLC circuit [68]

$$\nu_{SRR} = \frac{1}{2\pi\sqrt{LC}}, \tag{2.10}$$

$$\Delta\nu_{SRR} = \frac{R}{2\pi L}, \tag{2.11}$$

where $L = 1.9 \cdot 10^{-13}$ H and $R = (5 - \mathrm{i}50)\ \Omega$ are the self-inductance and the complex resistance of the ring, respectively, as calculated in Section 2.1.2. Here, $C = \varepsilon_o A/d$ is the capacitance of the air-gap, where d is the distance between the two sides of the air-gap and A is their area. For the specific geometry of the split-probe employed in chapter 6 we obtain $\nu_{SRR} \approx 245$ THz and $\Delta\nu_{SRR} \approx 4$ THz.

The polarizabilities $\underline{\underline{\alpha}}^{ee}$ and $\underline{\underline{\alpha}}^{mm}$ of the split-probe are qualitatively the same as for the coated probe[1]. The only exception is α^{ee}_{yz} (with respect to the system in Fig. 2.5B). In fact, we expect that, because of the air-gap in the coating, E_z would induce only one in-plane electric dipole moment (in the lower side of the ring in Fig. 2.5B). This dipole moment could couple to the fiber and, thus, would be detected[2].

In contrast to the coated probe, the split-probe exhibits nonvanishing cross-polarizability matrices. In fact, because of the air-gap, the magnetically induced current in the coating cannot completely flow around the ring (Fig. 2.5B) and, thus, the integral $\int_V \boldsymbol{J}_m \mathrm{d}^3x$ is not zero. The magnetically induced current generates a dipolar charge distribution across the gap and, thus, an in-plane electric dipole moment [73]. Hence, the term α^{em}_{xz} is nonvanishing. Like an out-of-plane magnetic field induces an in-plane electric dipole moment, an in-plane electric field will generate an oscillating charge distribution. This induces a circular current in the ring and, thus,

---

[1] The matrix $\underline{\underline{\alpha}}$ for the two probes are quantitatively rather different. In contrast to a coated probe, in a split probe all the terms of $\underline{\underline{\alpha}}^{mm}$ are resonant with the driving magnetic field [74].

[2] This is a only conjecture. There is no experimental proof for this mechanism yet.

an out-of-plane magnetic dipole moment, as shown in [75]. Thus, α_{zx}^{me} also is nonvanishing. Because of the symmetry of the probe, all other terms of the cross-polarizabilty matrices are zero [76].

In Chapter 6 we will indeed show that the vertical component of the magnetic field produces an in-plane electric dipole moment in the split-probe that can couple to the probe fiber and, thus, can be detected.

2.2 Phase- and polarization-sensitive time-resolved near-field microscope

Interferometry is a powerful tool used for the characterization of waves in many different areas of science, such as optics [77], astronomy [78], high energy physics, oceanography [79], seismology [80], diagnosis [81], etc.. By exploiting the interference effect, it is possible to gain knowledge not only on the amplitude of the wave but also on its oscillatory behavior, which is described by the phase. Moreover, with knowledge of a reference pulse, it is possible with interferometry to achieve information on the time duration of wave packets.

In optics there are several types of interferometric schemes that are employed to investigate materials. In this thesis, we use a Mach-Zehnder interferometer combined with a home-made near-field microscope [30]. In the following sections we will provide a brief summary of interferometry and describe the most relevant aspects of our setup.

2.2.1 The Mach-Zehnder interferometer

Let us consider a continuous wave laser source, for example a near-infrared tunable diode laser. The linearly polarized light from the laser diode is split by a beamsplitter in two identical branches and subsequently mixed together by another beamsplitter (Fig. 2.6). The two beams interfere with each other at the detector. We now insert in one of the two branches the sample under investigation. We call this branch of the interferometer the 'signal' branch and the other the 'reference' branch. The light focused on the detector generates a voltage drop $V_D = i_D R$, where i_D is the photocurrent and R is the resistance of the electronics system. The photocurrent is proportional to the light power P, where the proportionality constant σ_D is the sensitivity of the detector. Because the light power is $P = AI$, where I is the intensity of light and A is the spot-size of the focus, we obtain

$$V_D = R\sigma_D AI. \tag{2.12}$$

The light intensity is $I = n\varepsilon_o c(\boldsymbol{E}_R + \boldsymbol{E}_S) \cdot (\boldsymbol{E}_R^* + \boldsymbol{E}_S^*)/2$, where $\boldsymbol{E}_R$ and $\boldsymbol{E}_S$ are the vector electric fields of light in the reference and signal branch, respectively, c is the speed of light, ε_o is the dielectric permittivity of vacuum and n is the refractive index. Hence, the detector signal turns out to

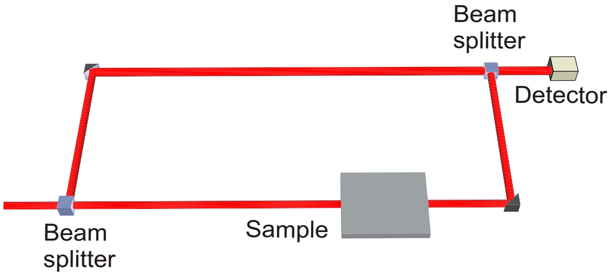

Figure 2.6:
Schematic representation of a Mach-Zehnder interferometer working in continuous wave mode. Light is split into two branches. The branch in which the sample is inserted is called the 'signal' branch, whereas the other is the 'reference' branch. Subsequently, the two branches are mixed together with another beam splitter and the interference signal is detected.

be

$$\begin{aligned} V_D &= C_D(\boldsymbol{E}_R + \boldsymbol{E}_S)\cdot(\boldsymbol{E}_R^* + \boldsymbol{E}_S^*) = C_D[|\boldsymbol{E}_R|^2 + |\boldsymbol{E}_S|^2 + 2\mathrm{Re}\{\boldsymbol{E}_R^*\cdot\boldsymbol{E}_S\}] \\ &= C_D[|\boldsymbol{E}_R|^2 + |\boldsymbol{E}_S|^2 + 2\boldsymbol{E}_R\cdot\boldsymbol{E}_S\cos(\Delta\phi)] \end{aligned} \tag{2.13}$$

where $C_D = R\sigma_D A\varepsilon_o c/2$ describes the conversion from optical to electronic signal and $\Delta\phi$ is the optical phase difference between the two branches. The first two terms of the righthand side of eq. 2.13 contribute a constant offset to the detected signal. The last term (the interference term) 'mixes' the signal of the two branches. When the sample is removed from the signal path, the two branches are identical and, thus, $\Delta\phi = 0$. Hence, by comparing the retrieved $\Delta\phi$ with or without the sample, we obtain information on the optical properties of the investigated sample, for instance a variation of its refractive index [82].

Interferometry can also be used to perform time-resolved measurements when a pulsed laser source is employed. In this thesis we use light from an optical parametric oscillator pumped by a Ti:sapphire mode-locked laser with a repetition rate of 80 MHz. The resulting near-infrared pulse has a duration of $\sim$ 100 fs. Electronically resolving the time duration of such a short pulse is not possible. In contrast, interferometry turns out to be a useful alternative, providing information on the pulse duration with respect

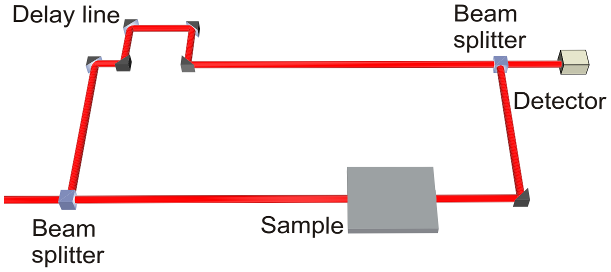

Figure 2.7:
Schematic representation of a Mach-Zehnder interferometer working in pulsed wave mode. In the reference branch a translation stage works as a delay line. As the path length of the two branches matches, the two pulses simultaneously arrive at the detector and the interference signal is detected.

to a reference pulse. In Chapter 5 we will select part of the spectrum of the fs-pulse with a spectral filter to obtain a pulse with a 2 nm bandwidth and a 2 ps duration.

The detector signal generated by the interference of the two pulses is:

$$V_D(t) = \frac{C_D}{T}\int_0^T \left\{|\boldsymbol{E}_R(t)|^2 + |\boldsymbol{E}_S(t+\tau)|^2 + 2\boldsymbol{E}_R(t)\cdot\boldsymbol{E}_S(t+\tau)\cos(\Delta\phi)\right\} dt \tag{2.14}$$

where T is the integration time of the detector and τ is a time difference between the reference and the signal pulse, which can also be written as the length difference $\Delta l = c/\tau$ of the two branches. Because T is much longer than the repetition rate of the laser, the detector experiences many pulses per integration time. When the length of the two branches is identical, $\tau = 0$ and we detect the time-averaged interference term. By varying the length of the reference branch with a translation stage (the delay line in Fig. 2.7), we vary τ and the time-averaged interference term decreases, following the shape of the cross-correlate of the two pulses. When the length difference is such that τ is larger than the coherence length of the two pulses, the time-averaged interference term is zero. Hence, by dynamically varying the length of the reference branch, we reconstruct the time duration of a fs-pulse [18]. It is important to note that the obtained pulse shape is the cross-correlate of the reference and signal pulse. In order to retrieve the actual duration of the signal pulse, the reference pulse must be known in amplitude and phase. Alternatively, we can perform reference measurements such that the properties of the sample are unraveled. By comparing the cross-correlate pulses obtained with and without the sample, we can obtain the influence of the structure on the pulse propagation.

Any minute difference in the refractive index of the two branches changes the relative phase difference between the two optical beams. As a result, interferometry is extremely sensitive to temperature gradients, vibrations, air convection and other phenomena that can induce a difference in refractive index between the two branches. On the one hand, one can exploit this sensitivity to detect small environmental variations. On the other hand, this sensitivity can be a severe limitation if one want a stable setup, as in the case of a phase-sensitive near-field microscope. To overcome undesirable phase variations, the interferometer is generally built on a vibration isolated table, is made as compact as possible and is placed in an isolating box to minimize the temperature gradient.

2.2.2 Heterodyne detection

Near-field microscopy has to deal with weak signals. In particular, the light power collected by a coated probe (see Section 2.1.2) can be on the order of 1 pW [13] and detecting it with the setup described in the previous section is hard. The integration time of the employed detector could be increased to improve the signal-to-noise ratio but interferometric measurements should be performed as quickly as possible to obtain a proper phase retrieval. In fact, the phase rapidly drifts as a function of time ($0.05 - 0.1$ deg/s) even in a very good interferometer, where the phase information is obtained after averaging over several measurements [82]. This is particularly important in phase-sensitive near-field microscopy, where the phase has to be stable during the time required to scan the probe (see Section 2.2.3). In our setup the detection of the interference signal is performed with a heterodyne scheme, which provides us with high signal-to-noise ratio with an integration time comparable to a typical duration of the scanning of the probe (see Section 2.2.3). We will show that with this detection scheme, we also retrieve the complex signal, in contrast with standard interferometry that only yields the real part of the interference signal (see eq. 2.13).

The frequency of the light in the reference branch is slightly shifted

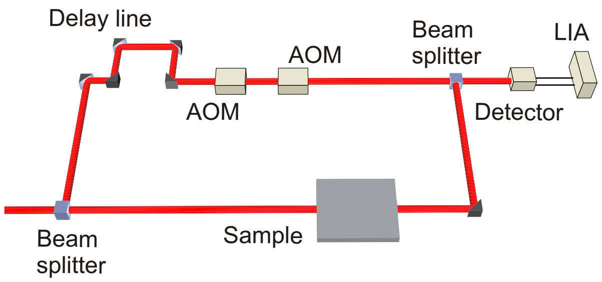

Figure 2.8:
Schematic representation of a heterodyne Mach-Zehnder interferometer. The frequency of the reference branch is Doppler shifted by ±40 kHz with two acousto-optic modulators (AOMs). The interference signal from the detector is detected by a lock-in amplifier (LIA), which is triggered at the same frequency.

using two acousto-optic modulators (AOMs) in a cross-configuration (Fig. 2.8). The first AOM Doppler shifts the frequency of light by 80 MHz, whereas the second shifts the frequency back by 80.04 MHz. As a result, after the second AOM the light has a frequency shift of ±40 kHz. The detector signal then is

$$V_D = C_D \left\{ |\boldsymbol{E}_R|^2 + |\boldsymbol{E}_S|^2 + 2\boldsymbol{E}_R \cdot \boldsymbol{E}_S \cos(\Delta\omega t + \Delta\phi) \right\} \tag{2.15}$$

where $\Delta\omega = \pm 2\pi \cdot 40$ kHz and $\Delta\phi = (\phi_R - \phi_S)$ are the frequency and the phase shift, respectively, between the two branches. The detector signal is sent to a lock-in amplifier (LIA), that is referenced to the same difference frequency. The lock-in detects only the signal characterized by a frequency of 40 kHz, namely the interference term $2\boldsymbol{E}_R \cdot \boldsymbol{E}_S \cos(\Delta\omega t + \Delta\phi)$. Because the lock-in uses only a small bandwidth ($25 - 80$ Hz) around $\Delta\omega$, the electronic noise with different frequency is suppressed, in particular the $1/f$ noise. The signal-to-noise ratio is drastically increased not only by the small bandwidth but also by the so-called heterodyne gain $\gamma = |\boldsymbol{E}_R|/|\boldsymbol{E}_S|$. In fact, the lock-in detects the amplitude $2\boldsymbol{E}_R \cdot \boldsymbol{E}_S = 2\gamma \boldsymbol{E}_S \cdot \boldsymbol{E}_S$ of the interference term of eq. 2.15. When the signal in the signal branch is weak, the optical power in the reference branch can be increased, such that $|\boldsymbol{E}_R| \gg |\boldsymbol{E}_S|$ and, therefore, $\gamma \gg 1$. Consequently, the signal-to-noise ratio improves. In contrast to standard interferometry, which detects also the off-set signal given by $|\boldsymbol{E}_R|^2 + |\boldsymbol{E}_S|^2$ (eq. 2.13), a heterodyne scheme only detects the interference term.

The complex signal is retrieved as follows. The lock-in multiplies the detector signal with two electronic signals, namely $\sin(\Delta\omega t+\theta)$ and $\sin(\Delta\omega t+\theta+\pi/2)$, where θ is a phase shift that can be manually set on the lock-in. In this way, we obtain the time-averaged outputs

$$\begin{aligned} X &= C_D \frac{2\boldsymbol{E}_R \cdot \boldsymbol{E}_S}{T} \int_0^T \sin(\Delta\omega t + \theta)\cos(\Delta\omega t + \Delta\phi)dt \\ &= C_D \frac{2\boldsymbol{E}_R \cdot \boldsymbol{E}_S}{T} \int_0^T -\frac{1}{2}\sin(\Delta\phi - \theta) + \frac{1}{2}\sin(2\Delta\omega t + \Delta\phi)dt \\ &= -C_D \boldsymbol{E}_R \cdot \boldsymbol{E}_S \sin(\Delta\phi - \theta) = C_D \boldsymbol{E}_R \cdot \boldsymbol{E}_S \cos(\Delta\phi - \theta + \frac{\pi}{2}), \qquad (2.16) \end{aligned}$$

$$\begin{aligned} Y &= C_D \frac{2\boldsymbol{E}_R \cdot \boldsymbol{E}_S}{T} \int_0^T \sin(\Delta\omega t + \theta + \frac{\pi}{2})\cos(\Delta\omega t + \Delta\phi)dt \\ &= C_D \frac{2\boldsymbol{E}_R \cdot \boldsymbol{E}_S}{T} \int_0^T -\frac{1}{2}\sin(\Delta\phi - \theta - \frac{\pi}{2}) + \frac{1}{2}\sin(2\Delta\omega t + \Delta\phi)dt \\ &= -C_D \boldsymbol{E}_R \cdot \boldsymbol{E}_S \cos(\Delta\phi - \theta) = C_D \boldsymbol{E}_R \cdot \boldsymbol{E}_S \sin(\Delta\phi - \theta + \frac{\pi}{2}), \qquad (2.17) \end{aligned}$$

where T is the lock-in integration time. By choosing $\theta = \pi/2$, we obtain the complex signal S

$$\begin{aligned} S = X + iY &= C_D[\boldsymbol{E}_R \cdot \boldsymbol{E}_S \cos(\phi_R - \phi_S) + i\boldsymbol{E}_R \cdot \boldsymbol{E}_S \sin(\phi_R - \phi_S)] \\ &= C_D \boldsymbol{E}_R \cdot \boldsymbol{E}_S e^{\mathrm{i}(\phi_R - \phi_S)}. \qquad (2.18) \end{aligned}$$

With this detection technique we increase the signal-to-noise ratio and obtain the amplitude and the phase of the signal with respect to the reference branch.

Particular attention must be paid to the alignment of the two AOMs in the reference path. An AOM works as a time-varying diffractive grating. Light impinging to the AOM is primarily diffracted in three orders, namely 1, 0, -1. The 0 order does not change the frequency of light. The 1 and -1 orders shift the light frequency by ω and $-\omega$, respectively. By changing the order of the two AOMs either $\Delta\omega > 0$ or $\Delta\omega < 0$ can be obtained. In experiments where the sign of the detected phase is important, this difference can be crucial. Let us consider the case where $\Delta\omega < 0$. Because the frequency of the signal that triggers the lock-in is always positive, the argument of the cosine in eq. 2.15 must be inverted and the interference term becomes $2\boldsymbol{E}_R \cdot \boldsymbol{E}_S \cos(\Delta\omega t - \Delta\phi)$. As a result, the sign of the phase in eq. 2.18 is changed, inverting the phase relation between the reference and the signal branch. In this thesis the AOMs are set such that $\Delta\omega < 0$ and, thus, the detected phase is $\Delta\phi = (\phi_S - \phi_R)$.

The use of AOMs has some inconveniences. Firstly, the crystal employed in an AOM introduces a large dispersion in the reference branch. On the one hand, this dispersion can be balanced in the signal branch by adding a crystal with the same dispersion (in Fig. 2.8 this crystal is not shown). On the other hand, balancing the two branches stretches the pulse duration in both branches decreasing the peak power of the laser pulse[3]. Secondly, because we use the first and the minus first order, the transmittance of the two AOMs is only ∼ 1%. Thirdly, the temperature of the AOMs is ∼ 40 °C. This creates a strong temperature gradient and a pronounced convection around AOMs that may unbalance the interferometer. As a result, our interferometer has a phase drift of the order of 0.3 deg/s. A practical solution to that problem could be to isolate the AOMs thermally from the interferometer with additional boxes.

2.2.3 Amplitude and phase maps

In our setup a heterodyne interferometer is combined with a near-field microscope. The evanescent field of light in the sample is collected by the probe (Fig. 2.9). The light is mixed with the reference branch in a fiber-coupler and detected with the heterodyne scheme described in Section 2.2.2. We retrieve from eq. 2.18 the amplitude and the phase of light at a fixed probe position. As we raster scan the probe, which is kept at a distance less than 20 nm from the sample, we reconstruct the amplitude and phase distribution of the evanescent field above the sample and obtain a good measure of the spatial distribution of light propagating inside the structure [83]. The employed highly sensitive homemade near-field microscope can scan the probe above a 2D photonic structure with a typical speed[4] of ∼ 30 µm/s. Because the phase gradient of our interferometer is ∼ 0.3 deg/s,

---

[3] This could be a severe limitation in case of non-linear optical investigation.

[4] The scanning speed strongly depends on the roughness and dimension of the asperities present on the investigated sample: the smoother the surface of the specimen, the faster the probe can be scanned.

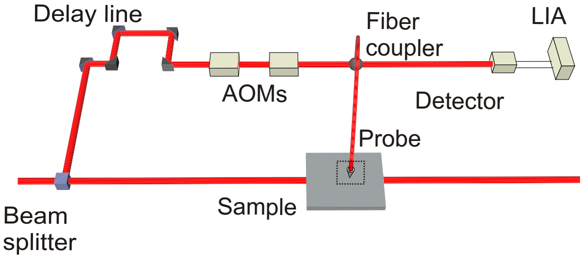

Figure 2.9:
Schematic representation of the phase-sensitive and time-resolved near-field microscope. The evanescent field of light in the sample is coupled by the probe (indicated by the dashed box) to the fiber. The collected light is mixed in a fiber-coupler with the reference branch and detected with a heterodyne scheme. By raster scanning the probe above the sample we reconstruct the amplitude and the phase distribution of the probed field.

during a scan of 50 µm the phase drift is only 0.1%. Thus, we achieve a stable phase information which provides a unique characterization of the optical properties of a photonic structure. For instance, we can retrieve the dispersion of complicated photonic structures, such as photonic crystal waveguides [56], or investigate optical singularities at the nanoscale (see Chapter 1 and 3).

2.2.4 Phase-sensitive polarization detection

A closer look to eq. 2.13 shows that when the polarizations of the reference and signal branch are orthogonal the interference term is zero. This means that interferometry is sensitive to the relative polarization state of the two branches. Therefore, we can exploit this property in order to detect different components of the electric field in the signal branch, by controlling the polarization of the reference branch.

In order to simultaneously detect the two orthogonal polarizations that might be present in the signal branch we need to slightly modify the setup (Fig. 2.10). We introduce a $\lambda/2$-waveplate that controls the orientation of the linear polarization of the reference. The reference polarization is oriented with a 45 degrees angle with respect to the two orthogonal po-

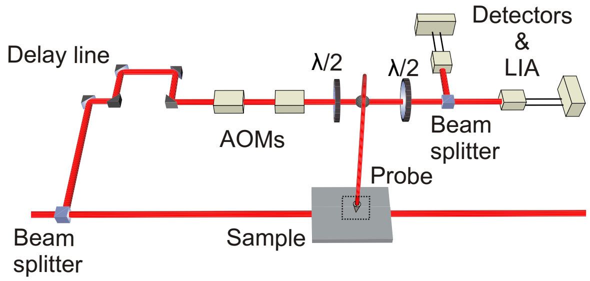

Figure 2.10:
Schematic representation of the phase- and polarization-sensitive time-resolved near-field microscope. A $\lambda/2$-waveplate controls the linear polarization of the reference branch. This orientation is chosen such the the reference light equally interferes with the two orthogonal polarization states in the signal branch. Subsequently, these two polarization states are split by a polarizing beamsplitter cube and simultaneously detected with a heterodyne scheme. An additional $\lambda/2$-waveplate is introduced in order to orient the polarizations with the polarization axes of the beamsplitter cube.

larizations in the signal branch. In this way, the reference branch equally interferes with both polarizations. We subsequently split the two polarizations by using a polarizing beamsplitter cube and separately detected them with a heterodyne scheme. In order to orient the polarization of the mixed light (reference+signal) with the polarization axes of the beamsplitter cube, we insert another $\lambda/2$-waveplate (Fig. 2.10). The advantage of this configuration is that we simultaneously measure two polarizations with only one interferometer. As a result, provided that the two polarizations in the signal branch experience the same optical path after the sample, we can directly compare the phase of the two polarizations. Hence, it is extremely important that the birefringence of the setup is reduced as much as possible. The most logical solution is to remove all fiber optics present in the setup. Unfortunately, this turns out to be a challenging task because the near-field probe itself is created from an optical fiber (see sect. 2.1). However, we will show in Chapter 6 that, if the strain of the optical fiber components in our setup is minimized, the birefringence of the system is negligible.

Chapter 3

Polarization singularities and photonic crystal waveguides

With a phase-sensitive near-field microscope we measure independently the two in-plane electric field components of light propagating through a 2D photonic crystal waveguide and the phase difference between them. Consequently, we are able to reconstruct the electric vector field distribution with sub-wavelength resolution. In the complex field distribution we observe both time-dependent and time-independent polarization singularities and determine the topology of the surrounding electric field.

3.1 Introduction

A wave singularity can be defined as a position in space where a property of a wave is not defined. Such singularities can be found in many types of waves and they can have a large impact on common life. For instance, they play an important role in heart fibrillation [39] and in the distribution of tides [38]. Moreover, wave singularities are studied in many different fields of physics, such as high energy physics [84], Bose-Einstein condensation [85–87], superconductivity [88] and superfluidity [89]. In optics, wave singularities have been studied since the 1830s (for an overview, see for instance Berry [37]) and have been observed in the interference patterns of the diffracted light that is surrounding us [27]. The simplest class of wave singularity is the so-called wave dislocation [24] (vortex, phase singularity, edge dislocation, etc.), which is a scalar field singularity that occurs where the amplitude of a complex valued field is zero and hence its phase is undefined or 'singular' (see Section 1.3.1 [90–92]). Another more subtle class is formed by the so-called polarization singularity (C-points, L-lines and disclinations), which occurs in vector fields at positions where one of the parameters that characterize the polarization ellipse (handedness, eccentricity or orientation) is singular (see Section 1.3.2 [25, 26, 93]). In the last few years polarization singularities have been investigated in optics in the context of tightly focused beams [94], crystal optics [95], skylights [96] and speckle fields [36, 97]. The polarization state of light is of crucial importance in quantum optics. Control of the local polarization state with a nanophotonic structure could therefore be exploited to manipulate a Bose-Einstein condensate trapped close to a surface [98], an atom chip [99], or a photonic crystal [100]. In addition, a spatial dependence of the polarization state will have important consequences for the use of single emitters in photonic nanostructures [44] for quantum information processing. Near-field microscopy has already proven to be a powerful tool in studies of the polarization distribution close to photonic nanostructures [101, 102].

In this chapter, we observe the presence of polarization singularities at the nanoscale in the fields above a 2D photonic crystal waveguide. We succeeded in the separation of the two in-plane field components above the waveguide with high selectivity. Exploiting the measured phase difference between the components, we reconstruct the distribution of the in-plane electric vector field with sub-wavelength resolution. We are able to observe several types of polarization singularities and the topology of the surrounding field at the nanoscale.

3.2 Experimental results

The setup is schematically shown in Fig. 3.1. The inset in the upper-left corner shows the photonic crystal waveguide used in this work. The sample consist of a silicon membrane with a 200 nm thickness with a periodic triangular arrangement of holes (lattice constant a=450 nm). The waveguide is formed by a single missing row of holes. The light source used to investigate the sample is a diode laser tuned to a vacuum wavelength of 1463 nm. The linearly polarized light is coupled into the waveguide by focusing it on the entrance facet. The field above the sample is picked up by the sub-

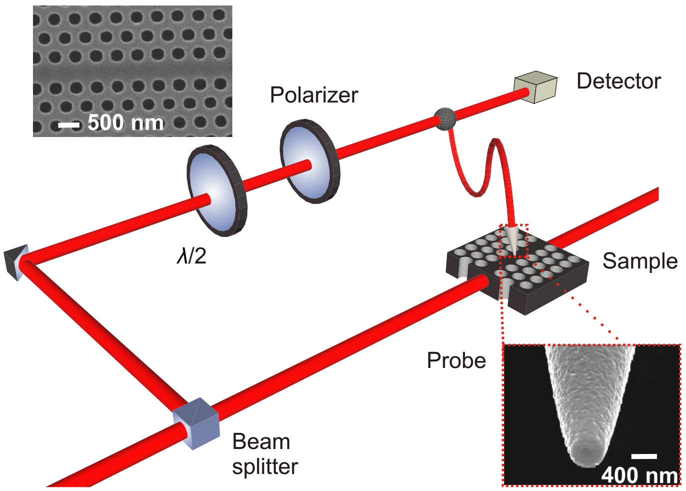

Figure 3.1:
Schematic representation of the experimental setup. Light is coupled into a 2D photonic crystal waveguide. The near-field probe is scanned above the sample and collects light that is interferometrically mixed with a reference beam and detected using a heterodyne scheme. The polarization state in the reference branch is controlled using waveplates. (left inset) Scanning electron micrograph of the silicon membrane photonic crystal waveguide under investigation (lattice constant $a = 450$ *nm and hole diameter* $d = 250$ *nm). (right inset) Scanning electron micrograph of the aluminum-coated near-field probe with aperture of* ≈ 200 *nm.*

wavelength aperture of an aluminum-coated near-field probe (see Section 2.1.2 lower-right inset of Fig. 3.1), that is kept 20 nm above the sample using shear force feedback. The light collected by the probe is interferometrically mixed with a reference signal and subsequently recorded using heterodyne detection [30, 83, 103]. Raster scanning the near-field probe above the 2D photonic structure, we recover the phase and the amplitude pattern of the light field in the waveguide with sub-wavelength resolution. This allows us to reconstruct the complex electric field as $E(x, y) = A(x, y)e^{i\phi(x,y)}$, where A and ϕ are the position-dependent amplitude and phase, respectively. Moreover, when two orthogonal polarizations are present in the probe fiber, we can select either one by choosing the appropriate polarization for the reference branch. As a result, our near-field setup is now sensitive to the polarization state of the near-field.

3.2.1 Detecting the in-plane electric field distribution

Figures 3.2A and B show the amplitude pattern recorded for two orthogonal polarizations of the reference signal. The amplitude is normalized to the maximum value and the scanned area is $4a \times 5a$. The waveguide is centered around $x = 0$. Using Fourier analysis, we observe the presence of both forward and backward propagating Bloch modes in the photonic crystal waveguide (see Section 1.2.2). We attribute the backward propagating mode to light that is reflected at the end-facet of the waveguide. When we select only the forward propagating mode by applying a Fourier filter to the experimental data [13], we obtain the amplitude distribution shown in Fig. 3.2C and D. Figures 3.2E and F show the amplitude of the E_x and E_y components of the electric field, respectively, of the forward propagating mode, as obtained using 3D finite-difference time-domain (FDTD) calculations. Figures 3.2G and H show the line traces of the real part of the complex signals along the dashed lines of Fig. 3.2C, D, E and F. Blue corresponds to the measurements and red to the calculations. Whereas in the first image the line traces are symmetric, in the second the line traces have an antisymmetric pattern, with a zero-crossing in the center of the waveguide. We find an excellent agreement between the measured and the calculated patterns. Thus, by utilizing a highly symmetric aperture probe, we have succeeded in measuring the field distribution of the in-plane electric field components by using two suitably chosen orthogonal polarization in the reference branch.

3.2.2 Polarization singularities

Exploiting the amplitude and the phase relation between the electric field components, we reconstruct the in-plane vector field of the electric field in a single unit cell of the photonic crystal waveguide. Figures 3.3 show the experimentally and theoretically obtained vector plot of the electric field. The depicted area is $2a$ x $1a$ and the waveguide is centered around $x = 0$. The contour lines indicate the measured and calculated electric field magnitude. The out-of-plane component is only significant near the edges of the holes and is vanishing elsewhere. We can therefore consider

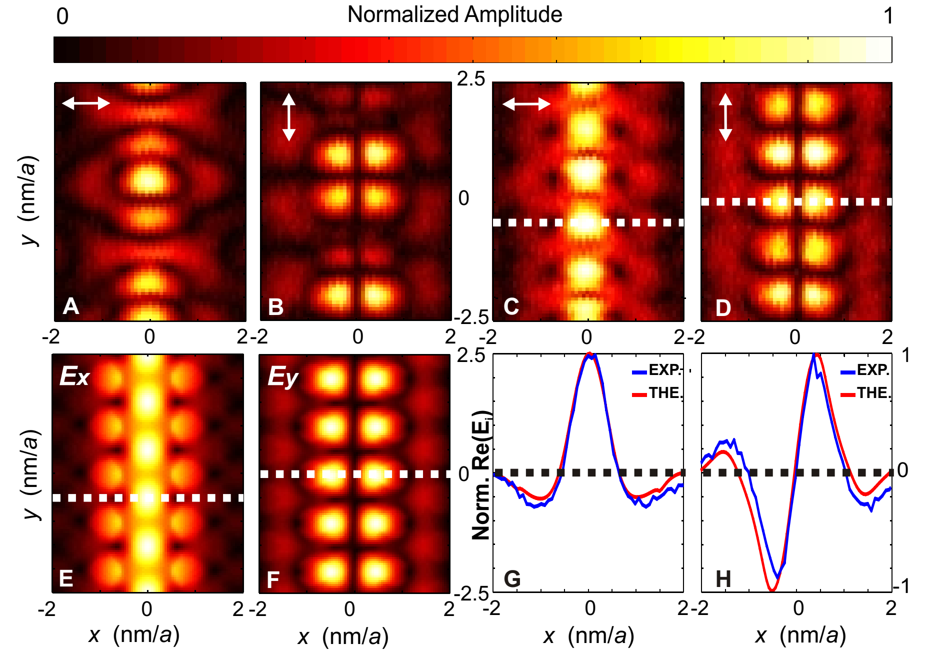

Figure 3.2:
A and **B**, *Detected amplitude pattern for two orthogonal polarizations (indicated by white arrows) in the reference branch.* **C** and **D**, *Amplitude pattern of the forward propagating mode, obtained after Fourier analysis of Fig. 3.2A and B.* **E** and **F**, *Theoretical amplitude pattern of* E_x *and* E_y *20 nm above the surface for the forward propagating mode. For all the images the depicted area is* $4a \times 5a$ *(the center of the waveguide is around* $x = 0$*) and the amplitude is normalized.* **G** and **F**, *Crosscuts of the experimentally (blue) and theoretically (red) obtained real part of the complex field along the dashed lines of Fig. 3.2C, D, E and F, respectively.*

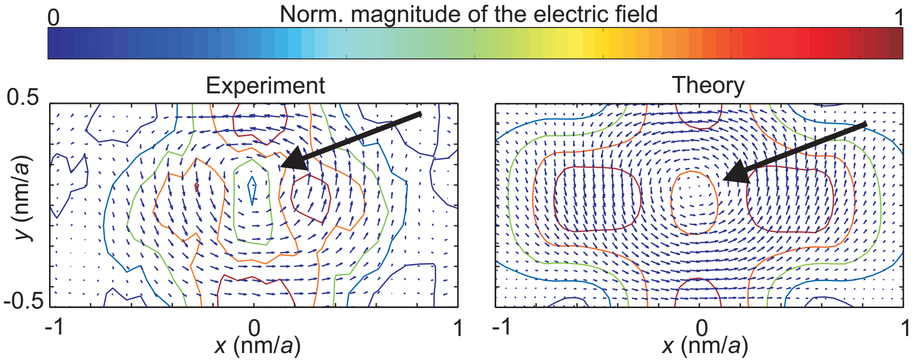

Figure 3.3:
Experimentally and theoretically obtained instantaneous 2D vector plots of the electric field. The contour plots indicate the normalized magnitude of the electric field. The black arrows highlight a disclination. For both figures the depicted area is $2a \times 1a$ *(the center of the waveguide is around* $x = 0$*).*

the electric field in the middle of the waveguide to be in-plane only. In a previous study, Lee *et al.* measured the intensity of the electric field components in the near-field [101]. In contrast, we perform phase-sensitive measurements that allow us to determine the actual instantaneous direction of the electric field.

In the instantaneous electric vector field shown in Fig. 3.3, we find a position where the electric field is at that moment zero (indicated by a black arrow). At this position the polarization state is undetermined. This is a so-called wave disclination (see Section 1.3.2). Such disclinations are singularities that move as time progresses. Because around such a singularity the electric vector field describes a complete circle (rotation of $\pm 2\pi$), it has a topological charge of ± 1 [26–28]. From the vector arrangement in Fig. 3.3 we infer that the topological charge equals $+1$. Usually, disclinations are studied in far-field transmission investigations in a plane orthogonal to the propagation direction of the light. It has been shown that the arrangement of the vectors surrounding a disclination varies as time progresses [26, 27]. In contrast, we investigate the polarization state in a plane parallel to the propagation direction and thus obtain insight in the disclination evolution inside the sample that generates it. We observe that the disclination moves

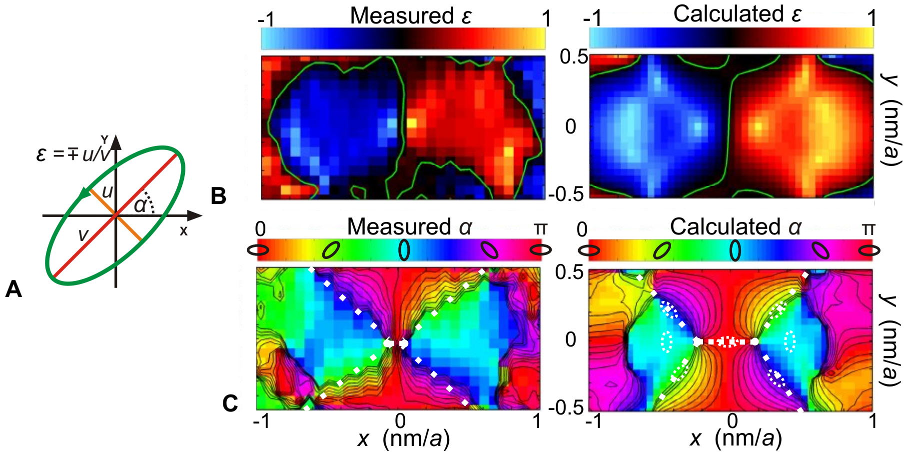

Figure 3.4:
A, *Representation of the polarization ellipse, where* v *is the major semi-axis,* u *is the minor semi-axis of the ellipse,* $\varepsilon = \mp u/v$ *and* α *the orientation angle.* **B**, *Experimentally and theoretically obtained* ε*. Negative and positive values correspond to left- and right-handed polarization, respectively. Lines of linear polarization (L-lines) are shown in green.* **C**, *Experimentally and theoretically obtained* α*. The dotted ellipses indicate the orientation of the polarization and the dashed lines show the 3-fold symmetry of the system. The white dots indicate the position of C-points.*

as time progresses but the topology around it is in a stable vortex shape. We attribute this to the fact that the disclination moves in the center of the waveguide, where there is a zero-crossing in E_y (see Fig. 3.2F). Hence, the electric field must be parallel to the x-direction for every point along the center of the waveguide. This condition fixes the topology of the vectors and prevents the deformation of the vortex around the dislocation.

To elucidate the polarization distribution of the light inside the waveguide further, we determine the ratio $\varepsilon = \mp u/v = \tan\{\arcsin[(\sin 2\psi)\sin\delta]/2\}$ and the orientation angle $\alpha = \{\arctan[(\tan 2\psi)\cos\delta]\}/2$ of the polarization ellipse, where v is the major semi-axis, u is the minor semi-axis (as illustrated in Fig. 3.4A). The angles $\psi = \arctan(|E_y|/|E_x|)$ and $\delta = \delta_y - \delta_x$ characterize the amplitude ratio and the phase difference between the two electric field components, respectively [8]. Thus, to determine ε and α from the two field components, knowing the phase relation between them is crucial. Figure 3.4B shows ε retrieved from the measured and calculated vector field distribution of Fig. 3.3. Negative and positive values correspond to left- and right-handed polarization, respectively. Two areas of opposite handedness are in close proximity (within 2 unit cells, or 860 nm). Fig. 3.4C depicts the angle α retrieved from the calculated and measured field distribution. Note that, because $\alpha = 0$ and $\alpha = \pi$ correspond to the same polarization state, we have chosen a cyclic color map. The phase-sensitive near-field measurements and the calculations show that, in an area of the order of the square wavelength in material $[(\lambda/n)^2]$, the polarization state has an antisymmetric structure.

When the polarization is purely linear ($\varepsilon = 0$), the handedness of the polarization ellipse is undetermined. This occurs along the so-called L-lines, which separate areas of opposite handedness (see Section 1.3.2). The abovementioned polarization disclinations must move along L-lines as time progresses [27, 28]. In Fig. 3.4B L-lines are indicated by green lines. We find a good match between measurement and calculation. The disclination observed in Fig. 3.3 lies on the L-line in the center of the waveguide for both experiment and theory, as predicted by Nye in [26].

When $\varepsilon = \pm 1$ the polarization is purely circular, which means that the orientation of the angle α is undetermined. Positions where this occurs are referred to as C-points (see Section 1.3.2). Around such a point the polarization ellipse describes a semicircle (rotation of $\pm\pi$). Thus, these singularities are characterized by a topological charge of $\pm\frac{1}{2}$, where the sign is determined by the rotation of the direction of the ellipse around the C-point [27, 28]. In order to identify C-points, we introduce the so-called isogyres, defined as lines of equal α. These isogyres are shown in Fig. 3.4C as black lines. The isogyres clearly converge on two points (white dots in Fig. 3.4C) close to the center of the photonic crystal waveguide. Because by definition the isogyres are lines with one unique value of α, their intersection is possible only when α is undetermined. Thus, the intersections of the isogyres are C-points. The dashed white lines and ellipses in Fig. 3.4B show the symmetry and ellipse orientation around the C-points, respectively. Both the C-points have topological charge $-\frac{1}{2}$ and a 3-fold symmetry. This means that this is a so-called *star* singularity. For further information about the classification of the singularities see Section 1.3.2

or [27]. We observed that the Bloch mode propagating in a photonic crystal waveguide generates in every unit cell two circular polarization singularities in sub-wavelength proximity (200 nm according to calculation and 50 nm according to the measurements). In previous publications it has been shown that polarization singularities with the same topological charge repel each other (the so-called topological singularity screening) [36, 95]. However, as the two C-points we investigated have opposite handedness, they are essentially independent and therefore screening does not play a role here.

3.3 Conclusion

In conclusion, exploiting the polarization properties of a highly symmetric aperture near-field probe, we experimentally visualized the electric vector field of the light propagating through a photonic crystal waveguide. We observed with sub-wavelength resolution the vectorial topological defects present in the photonic crystal waveguide. We found two *star*-type circular polarization singularities in sub-wavelength proximity and a disclination lying on a L-line in the center of the waveguide itself. All the measurements are in good agreement with the 3D FDTD calculations. The observed dependence of the polarization state can be used for the on chip manipulation of (cold) atoms and may lead to new strategies for quantum information processing with nanophotonic structures.

Chapter 4

Active control of light trapping by means of local magnetic coupling

The ability to actively tune the properties of a nanocavity is crucial for future applications in photonics and quantum information. Two important man-made classes of materials have emerged to mold the flow of electromagnetic waves. Firstly, photonic crystals are dielectric nanostructures that can be used to confine and slow down light and control its emission. They act primarily on the electric component of the light field. More recently, a novel class of metallo-dielectric nanostructures has emerged. These so-called metamaterials enable fascinating phenomena, such as negative refraction, super-focusing and cloaking. This second class of materials realizes light control through effective interactions with both electric and magnetic component. In this work, we combine both concepts to gain an active and reversible control of light trapping on subwavelength length scales. By actuating a nanoscale magnetic coil close to a photonic crystal nanocavity, we interact with the rapidly varying magnetic field and accomplish an unprecedented control of the optical properties of the cavity. We achieve a reversible enhancement of the lifetime of photons in the cavity. By successfully combining photonic crystal and metamaterials concepts, our results open the way for new light control strategies based on interactions which include the magnetic component of light.

4.1 Introduction

Photonic crystals are materials which provide a high level of control on the light-matter interaction, based on the engineered periodic modulation of the electric permittivity [104]. Nanoresonators in such photonic crystal architectures can store light in volumes comparable to the wavelength cubed for times longer than a million oscillation periods of the light [22]. Such high-Q photonic nano-cavities are promising structures to achieve strong coupling between light and quantum dots [105, 106]. The ability to actively tune the properties of a nanocavity is crucial for future applications in photonics and quantum information [105, 106]. Active tuning is achievable all-optically [107], electrically [108] or through the actuation of nano-objects in the evanescent electromagnetic field of the cavity [51, 109–112]. The latter strategy, which could lead to breakthroughs in the emerging field of optical nanoelectromechanical systems (NEMS) [113], relies typically on the interaction with the electric field in the cavity. This invariably leads to only red shifts of the resonance frequency and usually to a reduction of the photon lifetime of the cavity [51, 109–112]. In principle, an interaction with the magnetic field would also allow tuning of the cavity [110]. Unfortunately, natural materials have a negligible magnetic permeability at optical frequencies. We can overcome this limitation by borrowing concepts from metamaterials. These engineered materials work by geometrically inducing a magnetic response [114]. By using this idea, we have achieved active and reversible tuning of a photonic crystal nanocavity by interacting with the magnetic field of the trapped light. We use a cylindrically symmetric, metal-coated probe as a 'nanocoil'. By positioning the probe close to the cavity, the z-component of the magnetic field induces a counteracting magnetic response in the nanocoil through Lenz' law. As a result, we are able to induce a novel blue shift of the resonance frequency. More importantly, we are able to achieve an increase of the quality factor Q. In other words, we are able to increase the photon lifetime in the cavity.

4.2 Experimental results

4.2.1 Setup and near-field measurements

We investigate a photonic crystal nanocavity which is side-coupled to a photonic crystal waveguide (see inset Fig. 4.1A and Section 1.2.3) [14]. The

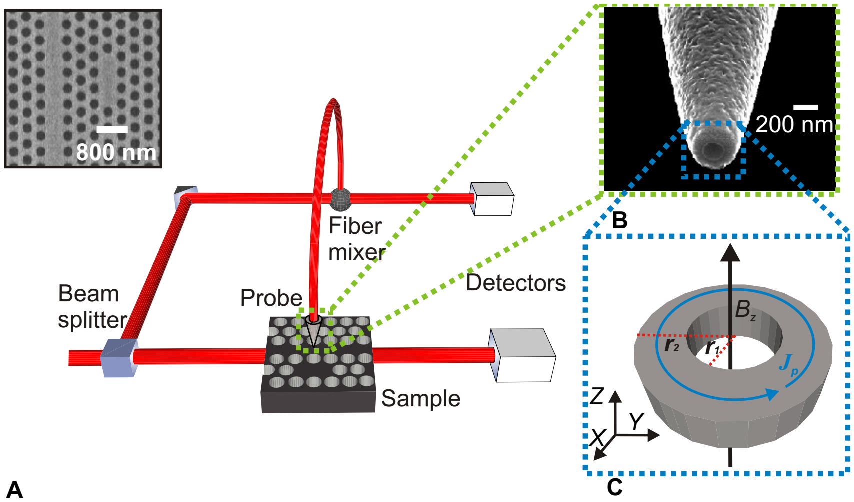

Figure 4.1:
A,*The near-field probe is scanned above the sample and collects the evanescent field of the light in the structure. The collected light is mixed with a reference beam and subsequently detected with a heterodyne scheme. The light power transmitted by the structure is also detected. A scanning electron micrograph of the sample investigated is shown in the inset. The photonic crystal nanocavity is visible below the photonic crystal waveguide.* **B**, *A scanning electron micrograph of the cylindrical symmetric aluminium-coated near-field probe.* **C**, *Schematic representation of the ring that models the end of the near-field probe. The magnetic field B_z, that is orthogonal to the ring, induces a current density J_p in the ring. r_1 and r_2 are the outer and the inner radius, respectively.*

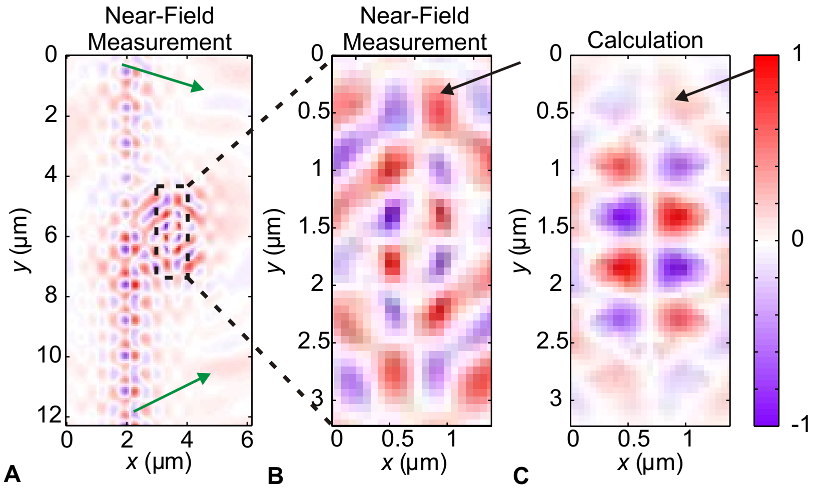

Figure 4.2:

A, *Distribution of Re*(E_y) *detected in the near field of the sample at resonance. The electromagnetic field depicted here is propagating through the accessing waveguide and coupled to the cavity. The color scale is varying between the maximum (red-positive) and the minimum (violet-negative) of the interference signal.* **B**, *Image of the distribution of the detected Re*(E_y) *in the near field above the area indicated in the dashed box of Fig. 4.2A. The green arrows indicate the detected in-plane radiation lost by the cavity.* **C**, *Image of the calculated distribution of the longitudinal component obtained by FDTD calculations at resonance.*

nanocavity exhibits a resonance at a vacuum wavelength of $\lambda_o = 1534.6$ nm with a quality factor $Q_o = 6500$. In order to excite the cavity, light from a tunable diode laser is coupled to the access waveguide. The electric field distribution inside and around the cavity is detected with a phase-sensitive near-field microscope [83] (Fig. 4.1A). By raster scanning a tapered aluminum-coated single-mode fibre (Fig. 4.1B) above the sample at a constant height of 20 nm, we collect a minute fraction of the light and detect it with a heterodyne scheme. The near-field probe, which has an aperture of 200 nm and an aluminum coating of 100 nm, has a cylindrical symmetry [61]. The high symmetry of the probe allows us to detect the in-plane electric field distribution of the sample (see Chapter 3 and [57]). Figure 4.2A displays the distribution of $\mathrm{Re}(E_y)$ detected with a typical near-field measurement at vacuum wavelength λ_o. The image shows how the electromagnetic wave is guided by the waveguide and is coupled to the cavity, which is indicated by the dashed box in Fig. 4.2A. Excellent agreement is found between the measured (4.2B) and the calculated (4.2C) field distribution above the cavity, obtained by Finite Difference Time Domain (FDTD) method. Small deviations between theory and experiment are visible. The field outside the cavity appears stronger in the measurement than in the calculation, as indicated by the arrows. We assign this effect to the influence of the probe on the optical properties of the cavity, as it will been described later in this chapter.

4.2.2 Transmission measurements

While performing the near-field measurement, we simultaneously determine the transmission of the system by measuring the amount of light arriving at the output of the access waveguide. In order to investigate the influence of the probe on the transmittance of the system, we determine the normalized transmission $F(x, y, \lambda) = T_\mathrm{n}(x, y, \lambda)/T_\mathrm{o}(\lambda)$, where x and y represent the in-plane position of the probe, $T_\mathrm{n}(x, y, \lambda)$ is the transmission spectrum as a function of probe position above the cavity, and $T_\mathrm{o}(\lambda)$ is the unperturbed transmission spectrum obtained in absence of the probe. Figure 4.3A shows a typical image of this normalized transmission acquired on resonance ($\lambda = \lambda_\mathrm{o}$). Different probe positions may lead to either an increase (yellow areas in the image, $F > 1$) or a decrease (blue areas, $F < 1$) of the waveguide transmittance. This observation clearly indicates an interaction between probe and cavity. In addition, we analyze the normalized transmission as a function of wavelength for a fixed position of the probe. The upper image of Fig. 4.3B shows a typical graph of F for position 1 in Fig. 4.3A, whereas the lower image shows F for four other positions indicated in Fig. 4.3A. All spectra exhibit identical qualitative behavior. For wavelengths far away from the resonance, the influence of the probe is negligible, i.e. $F = 1$. For wavelengths close to λ_o, the probe-cavity interaction becomes evident since F undergoes a pronounced variation. The change in transmission is caused by a shift of the resonance ($\lambda_\mathrm{o} \rightarrow \lambda_\mathrm{n}(x, y)$) due to the probe-cavity coupling [51, 110], as a consequence of which light with wavelength λ_o no longer couples to the resonator. As a result, the light does not

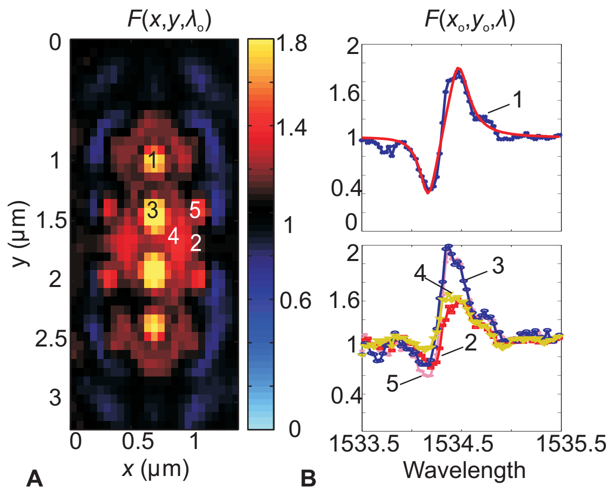

Figure 4.3:
A, *Image of the normalized transmission at resonance. In black the areas where the transmittance equals the unperturbed transmittance. For different positions of the probe the transmittance either increases or decreases.* **B**, *In the upper image the normalized transmission F for position 1 in Fig. 4.3A is shown. For wavelengths far away from the resonance the ratio is 1, indicating no influence of the probe. However, for wavelengths close to the resonance this ratio varies drastically. The fit is shown as a red line. The lower image shows F obtained for different positions indicated in Fig. 4.3A.*

experience the small loss associated with being trapped in the cavity and the transmission increases. Conversely, light with a wavelength close to the new resonance λ_{n} is now loaded in the resonator, leading to a reduction of the transmittance for that wavelength. It is clear that a distinct blue-shift of the cavity resonance occurs when the near-field probe couples to the cavity.

The induced resonance shift is the cause of the above-mentioned disagreement between Fig. 4.2B and C. When the probe is above the cavity, light with wavelength λ_o is not loaded and the electric field in the resonator is smaller than in the unperturbed system. Conversely, when the probe is at the position indicated by the arrow in Fig. 4.2B, light with wavelength

λ_o can couple to the nanocavity and the electric field at that location, as well as the signal detected by the probe, increases. As a result, the ratio between the electric field amplitude inside and outside the cavity for the measurement (Fig. 4.2B) differs from the same ratio for the calculation (Fig. 4.2C).

4.3 Data analysis

This unprecedented blue-shift can be intuitively understood in the following way. Due to the small extension in air of the evanescent fields above the cavity [115], the end of our near-field probe can be modeled as a metallic ring (Fig. 4.1C) that acts like a nano-coil in the electromagnetic field above the cavity (see Section 2.1.2). Faraday's law tells us that the magnetic field induces a circular current density $\boldsymbol{J}_\mathrm{p}$ in the ring (Fig. 4.1C). This current, in turn, generates a magnetic field that, according to Lenz' law, suppresses the driving field inside the ring [5]. The probe, thus, generates a volume where the total magnetic field is reduced. As a result, the effective volume occupied by the light stored in the cavity, the so-called cavity mode volume, is reduced, leading to a resonance shift towards shorter wavelengths.

4.3.1 Shifting the resonance to 'blue'

As a consequence, we expect that the probe-cavity coupling, and thus the variation of the transmittance, is most pronounced when the probe overlaps with the maximum in the amplitude of the out-of-plane component of the magnetic field. We experimentally verify our expectations by comparing the normalized transmission map, shown in Fig. 4.3A, with the amplitude distribution of B_z, obtained by FDTD calculation and shown in Fig. 4.4B. The symmetry and the maxima of the transmission map do coincide with the amplitude of B_z and not with the magnitude of the electric field $\boldsymbol{E}$ (Fig. 4.4A). This indication proves that the probe-cavity interaction is dominated by the magnetic coupling.

For a more formal description of the probe-cavity interaction one has to consider that the relative resonance shift is proportional to the relative energy shift of the system [51, 110]. Here, we have to take into account the induced magnetic dipole moment $\boldsymbol{m}$ of the probe interacting with the magnetic field in addition to the coupling between the induced electric dipole

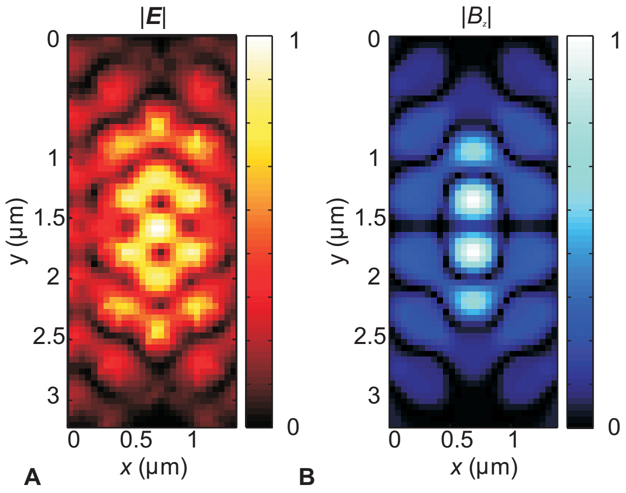

Figure 4.4:
A and **B**, *Distribution of the magnitude of the electric field* $\boldsymbol{E}$ *and of the amplitude of the vertical component of the magnetic field* B_z *normalized to their maximum, respectively. The area shown is the same as Fig. 4.3A. The two pictures show a different symmetry in the pattern of the field distributions.*

moment $\boldsymbol{p}$ of the probe and the electric field. Therefore, the resonance shift can be written as:

$$\frac{\Delta\omega_{\mathrm{o}}}{\omega_{\mathrm{o}}} = -\frac{\boldsymbol{E}_{\mathrm{o}}^{*}\cdot\boldsymbol{p} + \boldsymbol{B}_{\mathrm{o}}^{*}\cdot\boldsymbol{m}}{2U_E}, \tag{4.1}$$

where ω_0 is the resonant angular frequency of the system, $2U_E$ is the total energy stored in the cavity (for a rigorous derivation of eq. 4.1 see Appendix A). The dipole moments, in turn, are proportional to the unperturbed $\boldsymbol{E}_{\mathrm{o}}$ and $\boldsymbol{B}_{\mathrm{o}}$ and can be expressed as $p_i = \alpha_{ii}^{ee}E_i$ and $m_i = \alpha_{ii}^{mm}B_i$, where the label i indicates the spatial coordinates x, y and z. The proportionality constants α_{ii}^{ee} and α_{ii}^{mm} are the electric and magnetic polarizabilities of the probe, respectively (see Section 2.1.2). From eq. 4.1 it is clear that when the perturbative object only exhibits an electric response, the transmittance variation were largest when the probe overlaps with the amplitude maxima of the electric field [51, 109–112]. In order to calculate the electric polarizabilities, we can approximate the ring as a metallic oblate spheroid, following the methodology often employed in split-ring

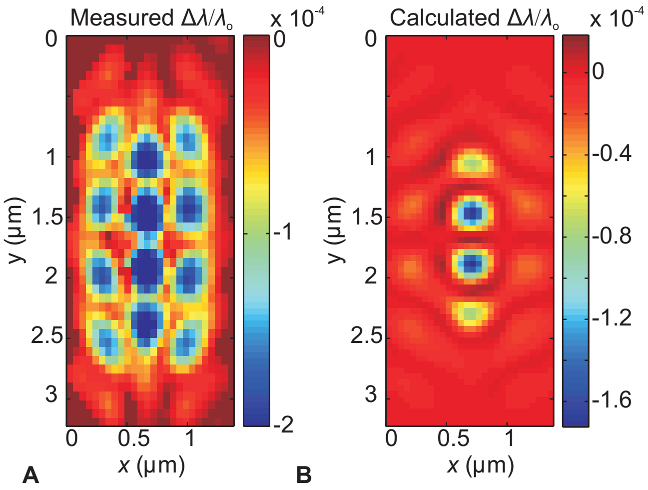

Figure 4.5:
A and **B**, *Images of the measured and calculated shift of the resonance* $\Delta\lambda_o/\lambda_o$ *at every probe position. Figure 4.5A shows an evident blue-shift of the resonance when the probe is above maxima of the* $|B_z|$*. We find an excellent quantitative agreement with the calculated resonance shift in Fig. 4.5B.*

resonators [74]. The electric polarizabilities turn out to be positive (see Section 2.1). The magnetic polarizability can be calculated by applying Faraday's law to a single metallic loop. This leads to a negative polarizability $\alpha_{zz}^{mm} = -A^2/(L + iR/\omega)$, where L is the self-inductance of the ring, R is the complex Ohmic resistance and r_2 is the outer radius (see Section 2.1). Besides exhibiting a positive electric polarizability, our near-field probe also has a negative magnetic polarizability. Thus, the electric coupling $\boldsymbol{E}_o \cdot \boldsymbol{p} > 0$ induces a red-shift [51, 109–112], whereas the magnetic coupling $\boldsymbol{B}_o \cdot \boldsymbol{m} < 0$ leads to a blue-shift. Thus, when the magnetic coupling dominates the resonance is primarily blue-shifted.

In order to compare the theoretical prediction of eq. 4.1 to our experimental data, we extract the relative shift $\Delta\lambda/\lambda_o$ from our measurements. For this purpose, we fit a transmission function based on coupled-mode theory [23] to the normalized transmission (see sect. 1.2). Figure 4.3B shows a typical fit as a red line. From the fit we obtained the relative resonance shift $\Delta\lambda/\lambda_o$ and the relative change in the quality factor $\Delta Q/Q_o$ for all probe positions. In Fig. 4.5A we show the measured $\Delta\lambda/\lambda_o$ as a function of the probe position. By comparing with Fig. 4.3A, it is evident that the largest relative blue-shifts, of the order of 10^{-4}, occur for positions of the probe where the amplitude of B_z is maximum. We calculate the resonance shift by using eq. 4.1 and the field distributions inside the cavity, which were obtained by FDTD calculations. In order to take into account the finite size of the probe, we use the average electric and magnetic fields over the area of the ring by making a convolution of the probe apex shape with the calculated field distributions. The theoretically obtained $\Delta\lambda/\lambda_o$ is shown in Fig. 4.5B. We find an excellent qualitative agreement with the experimental data (Fig. 4.5A).

4.3.2 Increasing the cavity photon lifetime

In addition to tuning the resonance frequency, we also control the lifetime of the photons in the cavity. In Fig. 4.6A, we show an image of the retrieved $\Delta Q/Q_o$ as a function of the probe position. Remarkably, the relative change in Q can, depending on the probe position, be both positive and negative! The largest increase of Q of 50% occurs right above the amplitude maxima of B_z, co-located with the largest blue-shift. The magnetic coupling between the probe and the cavity, thus, not only induces a novel blue-shift of the resonance but also causes the photon lifetime in the cavity to be increased.

Any 2D cavity is affected by losses due to intrinsic out-of-plane radiation [14]. In a previous study, Robinson *et al* [116] reported an increase of only 1% of Q of a nanocavity which resulted from the destructive interference between the out-of-plane radiation and its back-reflection from a metallic object much larger than the nanocavity itself. However, to significantly improve the Q, one has to destructively interfere with a larger amount of the out-of-plane radiation. We achieve 50% increase of the photon lifetime by exploiting the emission caused by the magnetic dipole moment of the probe. In fact, this induced dipole moment emits primarily along the surface of the sample in counter phase with respect to the driving field inside the cavity. On the other hand, as shown by Fourier analyses performed on the cavity mode [14], the cavity also radiates along the surface. We detected this radiation during a near-field measurement, as indicated by the green arrows in Fig. 4.2A where. Therefore, the in-plane radiation

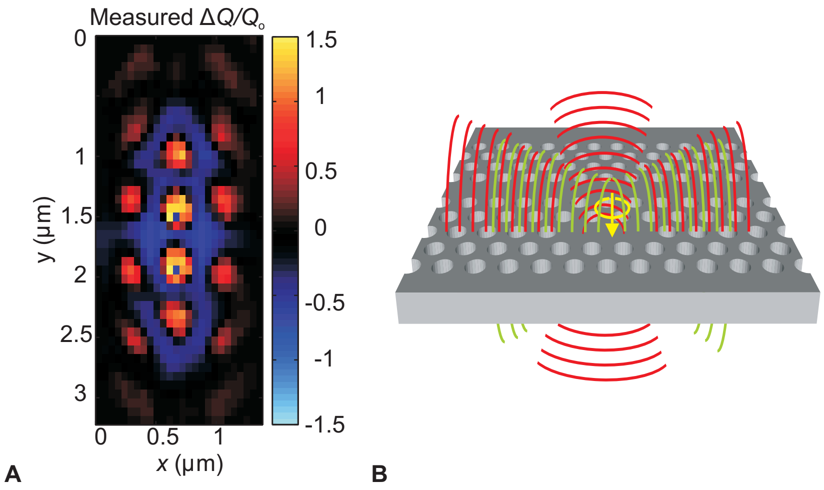

Figure 4.6:
A, *Image of the measured shift of the quality factor* $\Delta Q/Q_{\text{o}}$ *at every probe position. An increase and the decrease of the quality factor of the cavity is evident.* **B**, *Representation of the proposed mechanism that causes the increase of the quality factor. As the probe is above a maximum of the magnetic field, the induced current generates radiation that destructively interferes with the radiative loss of the cavity, yielding an increase of the photon lifetime.*

of the cavity and the emission from the probe destructively interfere (the process is schematically described in Fig. 4.6B). Moreover, analyses on the in-plane decay rate (see Section 1.2) show that we increase the quality of the cavity by also decreasing the coupling with the access waveguide. Remarkably, we obtain a pronounced increase of Q by exploiting at the nano-scale the scattered light from an object smaller than the nanocavity. Furthermore, we achieve an increase of the lifetime by means of magnetic coupling rather than electric.

4.4 Conclusion

Here, we have experimentally demonstrated that we can actively and reversibly control the trapping of light in a photonic crystal nanocavity by means of magnetic coupling with an actuated subwavelength object. The presented method opens up a new way for light control, combining photonic crystals and metamaterials concepts. Moreover, a new exciting application for photonic crystal nanocavities arises. We anticipate the possibility of measuring the magnetic dipole moment of magnetically resonant nano-object, such as single split-ring resonator [117] or single twisted split-ring resonator dimers [75], by actuating it above a maximum of the magnetic field of the nanoresonator. Along these lines, we also envision the striking possibility of using a state-of-the-art ultra-high-Q [22] nanocavity, characterized by a sharp resonance, for measuring the minute magnetic susceptibility of molecules, such as carbon nanotubes [118] or ring-shape (aromatic) molecules [119].

Chapter 5

Local investigation of nano-confinement of light in space and time

Photonic crystal nanocavities have inspired great interest not only for fundamental research but also for applications, as they can be exploited for efficient light sources and devices for telecommunication, quantum information and computing. To enable further improvements, in situ information on the optical properties of the light confined into the nanocavity is crucial. Although several nanoscale investigations on the static behavior of a nanocavity have already been performed, information on the local dynamic properties remains hidden. Here, we obtain with phase-sensitive time-resolved near-field microscopy a direct observation of light confinement in a side-coupled photonic crystal nanocavity. As a result, we unravel the coupling mechanism between the photonic eigenstates of the nanoresonator and of the waveguide.

5.1 Introduction

The fascinating idea of controlling the spontaneous emission [104, 120] has driven the research of many scientists in the photonic community. Cavities with a high quality factor Q and small modal volume V [14] have been envisioned and realized for different type of applications, as low-threshold micro-lasers [121], nonlinear optics [122], second and third harmonic generation [123], photonic devices for telecommunication [124,125], quantum information [126] and sensing [127]. 2D photonic crystal nanocavities, which are characterized by a small mode volume (of the order of $(\lambda/n)^3$) combined with high-Q values (up to 2 million) [19,22,120], are particularly promising for quantum information. So far, the optical properties of nanocavities have been studied in the time and frequency domain with far-field experiments [20,120]. While this type of investigation provides valuable information on key performance indicators, like resonant frequency and Q, it does not give a direct insight on the governing principles of the nanoresonator. In contrast, near-field microscopy provides the necessary subwavelength resolution for investigating, both spectrally and spatially, light confinement in a small modal volume cavity [111,128]. In this chapter, we present a phase-sensitive time-resolved near-field investigation [83] of the dynamic behavior of light confined in a photonic crystal nanocavity. The sample under investigation is a photonic crystal nanocavity side-coupled to a photonic crystal waveguide (see Section 1.2.3). We provide a direct visualization of the light as it couples to the cavity, gets stored into it and subsequently leaks away. Also, detailed Fourier analysis of the sub-wavelength information lays bare the coupling mechanism between the side-coupled nanocavity and the adjacent waveguide.

5.2 Experimental results

The setup is schematically depicted in Fig. 5.1 and described in Section 2.2. The waveguide is formed by a single missing row of holes in a photonic crystal (inset Fig. 5.1), whereas the cavity, with a resonant wavelength of 1534.6 nm, is formed by removing three holes. We perform time-resolved measurements using a ps-pulse laser at a wavelength of 1534 nm with spectral width equal to 2 nm. It is known that the near-field probe in the proximity of the nanocavity induces a frequency shift of the cavity resonance [51]. To infer the induced frequency shift, we analyze the transmission spectrum of the system (see Chapter 4) when the probe is above the cavity [110]. We found a maximum relative shift of the resonance of the order of $\sim 10^{-4}$, which is $|\Delta\lambda| \approx 0.3$ nm. Because the spectral width of the pulse is much broader than the resonance shift, both the unperturbed and the probe-induced resonance can be excited.

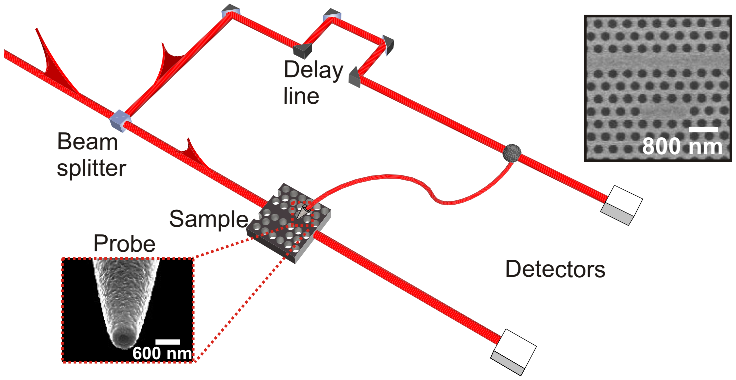

Figure 5.1:
Schematic representation of the setup. Linearly polarized light is coupled to the sample. The evanescent field of the light in the sample is collected by the aperture at the end of the near-field probe. Subsequently, the optical signal is interferometrically mixed with a reference branch and detected with a heterodyne scheme. Simultaneously, the light transmitted by the structure is detected. The optical delay line enables us to perform time-resolved measurements (see Section 2.2). ***right-side inset****, Scanning electron micrograph of the investigated sample. The photonic crystal nanocavity, formed by removing three holes, is visible below the photonic crystal waveguide.* ***left-side inset****, Scanning electron micrograph of the aluminum-coated near-field probe with an aperture of 200 nm.*

5.2.1 Real-space investigation

Figure 5.2A shows the amplitude detected in the near-field at $t = 0$ ps, before the pulse enters the scanned area. As the delay time is increased by increasing the length of the reference branch, the time evolution of the light field is obtained [55]. In the consecutive measurements shown in Fig. 5.2 we observe that the pulse propagates through the access waveguide and couples to the cavity (dashed box in Fig. 5.2F). Figure 5.2 shows in both space and time the confinement of light in a photonic crystal nanocavity.

In order to quantify the photon lifetime inside the resonator, we analyze the amplitude detected at positions 1 and 3 (indicated in Fig. 5.2A) as a function of time delay. Figure 5.3 depicts the time-dependent amplitude

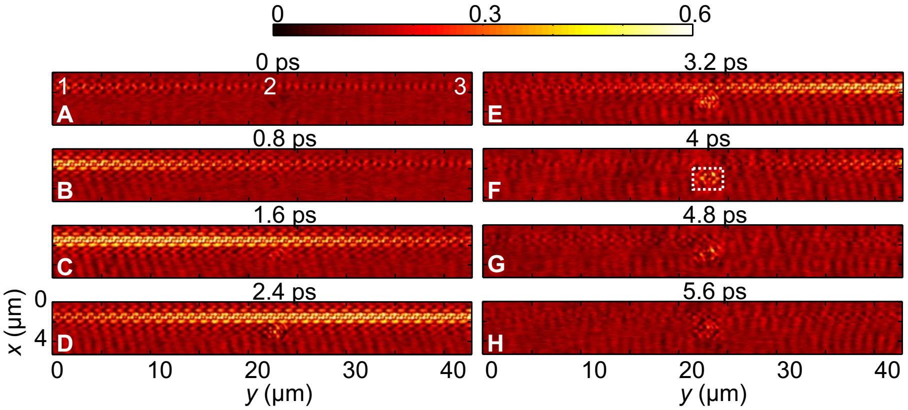

Figure 5.2:
A - H, *The normalized detected amplitude of the ps-pulse propagating through the sample for different times. The time difference between consecutive images is 0.8 ps for a total time interval of 5.6 ps. The color scale varies from 0 to 0.6 times the maximum detected amplitude, in order to enhance the visibility of the signal obtained above the cavity. The consecutive images show an optical pulse entering the access waveguide, loading the nanocavity and exiting from the waveguide. Position 1, 2 and 3 in Fig. 5.2A relate to the graphs in Fig. 5.3 and 5.5B. The dashed box of Fig. 5.2F indicates the position of the nanocavity.*

for both positions. The curve obtained in position 1 (blue dots) can be described by a cross-correlation function of the pulses in the reference and in the signal branch (see Section 2.2.1). The red line in Fig. 5.3 shows the fit $E_1(t)$ to the data obtained by using the cross-correlation function of two identical Gaussian functions. Here, we assume that the optical path in the reference and signal branch is nearly equal and, thus, the dispersion of the photonic crystal waveguide is negligible. This is a valid assumption considering the small bandwidth of the pulse and the linear dispersion of the photonic crystal waveguide at this wavelength. At position 3 the time evolution of the light field is affected by the filling of the nanocavity from the waveguide and the concomitant leakage back into the waveguide. Hence, the time-dependent amplitude at position 3 is given by the experimentally obtained envelope at position 1 convoluted with the response function of the cavity $\xi(t) = e^{-\frac{t}{\tau_0}}$, where τ_0 is the photon lifetime of the cavity. We

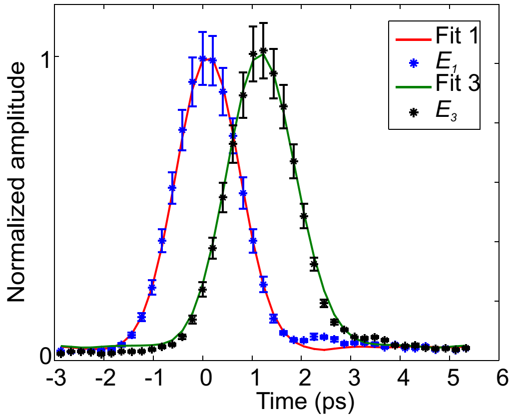

Figure 5.3:
The time-dependent amplitude detected above the waveguide: blue and black dots relate with position 1 and 3, respectively. Red and green lines are the fit for position 1 and 3, respectively.

performed a fit to the data using the convolution $E_3(t) = E_1(t) \otimes \xi(t)$. The fit is shown as a green line in Fig. 5.3 and the retrieved photon lifetime is $\tau_0 = 1.3$ ps. Because this technique is insensitive to the dispersion of the waveguide, we are able to directly measure the pulse reshaping induced by the cavity response without investigating reference structures and thus obtain an absolute characterization of the investigated cavity.

5.2.2 Reciprocal-space investigation

Whereas the basic dynamics of the mode coupling between the waveguide and the nanocavity is visible in Fig. 5.2, detailed information about the mechanism of the coupling of the waveguide mode to the eigenstate of the nanoresonator remains hidden. Exploiting the phase-sensitivity of our measurements, we are able to unravel the mechanism of the mode coupling between cavity and waveguide via Fourier analysis [13]. Figure 5.4A shows the spatial frequencies of the optical field in Fig. 5.2C obtained by applying a Fourier transform to the experimental data. With this procedure we can observe and separate the Bloch harmonics (see Section 1.2.2 and [1]) that compose the pulse traveling in the photonic crystal structure [17].

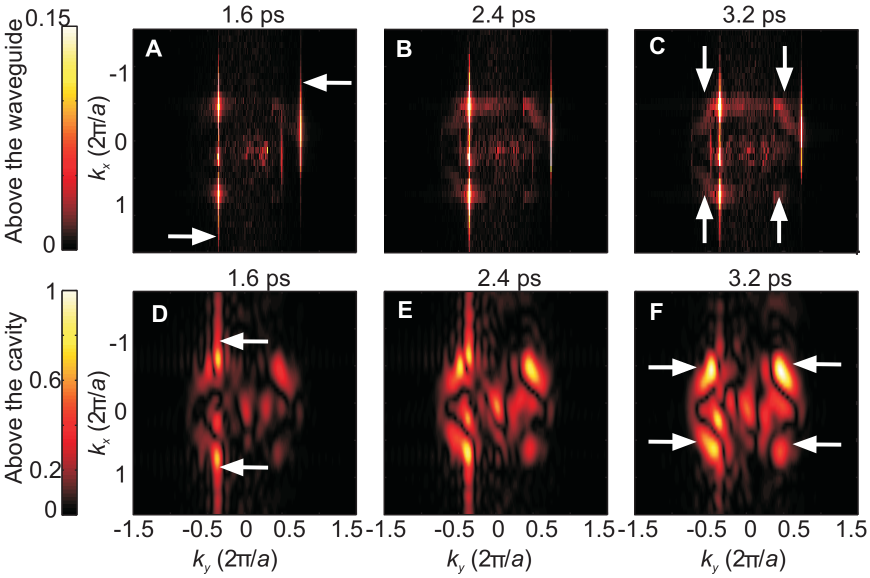

Figure 5.4:

A-C, *Reciprocal-space images of Fig. 5.2C, D and E normalized to the maximum of Fig. 5.4A. The spatial frequencies along* $\hat{y}$ *and* $\hat{x}$ *are normalized to* $2\pi/a$*. The bright features relate with the excited eigenstates of the investigated system: the subsequent images show the time evolution of the eigenstates. The white arrows of Fig. 5.4A indicate the fundamental (right arrow) and the -1 (left arrow) Bloch harmonic of the access waveguide. The white arrows of Fig. 5.4C indicate the four features which relate with the eigenstate of the cavity. The color scale is varying from 0 to 0.15 in order to enhance the visibility of the eigenstate of the cavity.* **D-F**, *Reciprocal-space images of the area indicated by the dashed box in 5.2F, for the same time delay of Fig. 5.4A-C. The k-vectors along* $\hat{y}$ *and* $\hat{x}$ *are normalized to* $2\pi/a$*. The white arrows of Fig. 5.4D indicate the -1 Bloch harmonic of the access waveguide that spatially overlaps the cavity. The white arrows of Fig. 5.4F indicate the four features that relate with the eigenstate of the cavity. The color scale is normalized to the maximum of Fig. 5.4F. The images show that the -1 Bloch harmonic is the promoter of the coupling between the modes in the waveguide and in the cavity.*

The white arrows in Fig. 5.4A indicate the maxima that relate with the fundamental Bloch harmonic ($m = 0$) and the -1 Bloch harmonic ($m = -1$) of the excited photonic eigenstate in the waveguide (see Section 1.2). Fig. 5.4B and C show the time evolution of the excited eigenstates in the system after 0.8 ps and 1.6 ps, respectively. In particular, in Fig. 5.4C four new features, indicated by white arrows, arise. These four features correspond to the eigenstate of the nanocavity.

We perform a Fourier analysis of the complex data detected directly above the cavity (dashed box in Fig. 5.2F). Figures 5.4(D-F) show the amplitude $A_k(t)$ of the Fourier transform for the same time delay of Fig. 5.4(A-C). We find an excellent agreement between Fig. 5.4F and the corresponding calculated spatial frequencies for a photonic crystal nanocavity [14]. The two brighter features in Fig. 5.4D (white arrows) represent the -1 Bloch harmonic of the waveguide which is present in the scanned area above the nanocavity, indicated by dashed box of Fig. 5.2F. As time progresses, the -1 Bloch harmonic peaks disappear and the cavity eigenstate peaks increase in magnitude (white arrows in Fig. 5.4F). Remarkably, these observations show that the -1 Bloch harmonic with its negative k-vector (Fig. 5.4E) is responsible for the light coupling to the nanoresonator. On the one hand, the -1 Bloch harmonic satisfies the k- or phase-matching condition necessary to excite the cavity eigenstate (Fig. 5.4E). On the other hand, the spatial distribution of the -1 Bloch harmonic overlaps with the spatial distribution of the cavity mode, as indicated by the Fourier analysis shown in Fig. 5.4D. In fact, as it has already been proven experimentally [129], the -1 Bloch harmonic is primarily located on the sides of the waveguide, and therefore in proximity of the cavity, whereas the fundamental Bloch harmonic is in the center. Hence, we infer that the -1 Bloch harmonic, rather than the fundamental Bloch harmonic, is the promoter of the coupling between the nanocavity and the waveguide.

In order to directly investigate the extent to which the dynamics of the system can be controlled through the probe-cavity coupling, we analyze the time evolution of the amplitude $A_k(t)$ of the cavity eigenstate. We consider the time-dependent intensity $I_k(t) = A_k^2(t)$, shown in Fig. 5.5A, as the time duration of $I_k(t)$ directly relates to the photon lifetime of the cavity. Initially the cavity is loaded by the pulse and the energy flow from the waveguide to the cavity exceeds the reverse flow (left half of Fig. 5.5A). Thereafter, the predominant flow of energy is from the cavity to the

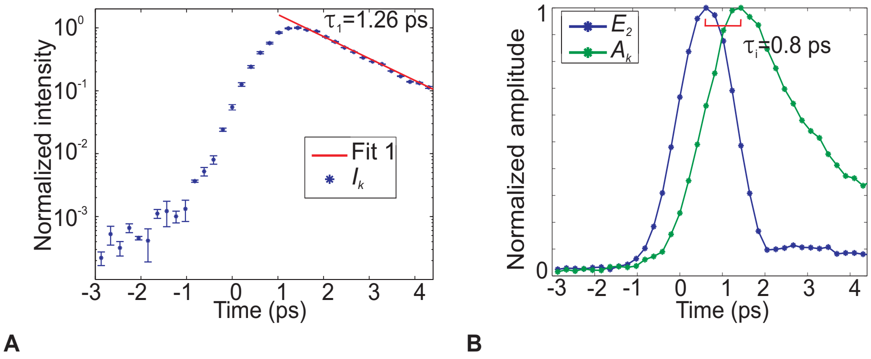

Figure 5.5:
A, *The blue dots relate with the time-dependent intensity (in logarithmic scale) of the eigenstate of the cavity. The red line is the fit to the exponential decay.* **B**, *time-dependent amplitude detected at position 2 above the waveguide (blue dots) and of the eigenstate of the nanocavity (green dots): the colored lines are guide to the eyes. The two maxima have a different position in time because the response of the nanocavity is slower than the pulse duration.*

waveguide and the signal exponentially decreases. Figure 5.5B compares amplitude $A_k(t)$ (green dots) with the amplitude detected at position 2. The evident delay between the two envelopes is induced by the loading time $\tau_i = 0.8$ ps of the cavity, which works as an integrator. From the exponential decay time of $I_k(t)$ in Fig. 5.5A (red line) we obtain that the photon lifetime in presence of the probe-cavity interaction $\tau_1 = 1.26$ ps. When we compare this value with τ_0, we find a relative change of the lifetime $\Delta\tau_1 = (\tau_1 - \tau_0)/\tau_0 \approx -0.03$ caused by the presence of the probe above the nanocavity. Each point in Fig. 5.5A has been obtained scanning the probe through several positions above the nanocavity. As shown in Chapter 4, different position of the probe induces different photon lifetimes. Thus, τ_1 has been inferred averaging through all probe positions. Hence, $\Delta\tau_1$ describes the position-averaged influence of the probe-cavity interaction on the photon lifetime of the nanocavity. Consequently, the relative change of lifetime $\Delta\tau_1$ has to be compared with the relative change of Q obtained in the investigation shown in Chapter 4. Averaging through all the positions of Fig 4.6, we obtain $\langle\Delta Q\rangle \approx -0.05$, where $\langle\cdot\rangle$ represent the spatial average, which is in good agreement with $\Delta\tau_1$.

5.3 Conclusion

We showed the first phase-sensitive time-resolved near-field observation of light confinement in a side-coupled photonic crystal nanocavity. The lifetime of the photons in the cavity was retrieved from the distortion of the pulse in the waveguide as it passes the cavity ($\tau_0 = 1.3$ ps). By directly measuring the decay of the cavity eigenstate, we obtained the influence of the probe-cavity interaction on the photon lifetime, which is a reduction of 3% of the photon lifetime, in good agreement with the investigation shown in Chapter 4. We also observed that the loading time of the cavity when excited by a ps-pulse is $\tau_i = 0.8$ ps. Exploiting the phase-sensitivity of our measurements, we showed that the coupling between the eigenstate of the waveguide and the eigenstate the nanoresonator is actually promoted by the waveguide -1 Bloch harmonic, because it satisfies the coupling conditions in both real- and reciprocal-space. These findings emphasize the versatility of near-field microscopy, showing that it is possible to obtain a full characterization of photonic nanostructures with a rather large variety of solutions. In particular, we achieved a novel insight in the physics lying behind the mode coupling between the access waveguide and the nanocavity investigated.

Chapter 6

Detecting the magnetic field of light

Light is an electromagnetic wave composed of oscillating electric and magnetic fields, the one field never occurring without the other. Nevertheless, in light-matter interaction at optical frequencies the magnetic component of light generally plays only a negligible role. When we "see" or detect light, we only perceive its electric field; we are practically blind to its magnetic component. Nowadays, a new class of man-made metallic materials, the so-called metamaterials, exhibit exciting phenomena, as negative refraction and optical cloaking, as a result of an effective magnetic coupling. The increasing interest in metamaterials demands a detection of the magnetic field at the nanoscale. In this work, we detect the magnetic field of light by using a properly engineered near-field aperture probe. We visualize with subwavelength resolution the magnetic and electric field distribution of propagating light.

6.1 Introduction

In nature, the force exerted by the electric field on charges is c/v larger than the force applied by the magnetic field, where v is the velocity of the charge and c the speed of light. As a result, the responsiveness of a material to a magnetic field, the magnetic susceptibility, is a factor 10^{-4} smaller than the ease with which it is polarized, the dielectric susceptibility [5]. Only when the charges move extremely fast, as for instance in relativistic plasmas [130, 131], can the magnetic and electric coupling become comparable (see Section 1.1). In atomic systems, even though the magnetic dipole coupling is extremely weak, it is very important for fundamental tests of the standard model [132]. However, magnetic light-matter interaction has been accomplished using artificial 'magnetic' atoms. By tailoring the geometry of such subwavelength metallo-dielectric structures effective magnetic coupling is achievable, which has been first shown in the microwave regime [68, 133]. Only in recent years, photonic nanostructures that resonantly respond to the magnetic field at optical frequencies have been fabricated [9, 73, 75, 82, 114]. This magnetic resonance can be exploited to study novel fascinating phenomena, such as negative index of refraction [9], super-focusing [10] and cloaking [11, 12]. Whereas many advances have been made in controlling the light-matter coupling by magnetic means, the possibility of directly detecting the magnetic field at optical frequencies has not yet been explored.

In this report, we experimentally prove that a near-field aperture probe, designed following split-ring resonator concepts (see Section 2.1), can detect the magnetic field at optical frequencies. We use such a probe to map the amplitude and phase of the magnetic field of propagating light. Furthermore, by simultaneously detecting the electric field, we reconstruct the magnetic and electric distributions of light with subwavelength resolution.

6.2 Experimental results

In order to detect the magnetic field at optical frequencies we have fabricated a nanostructured metallo-dielectric probe. To make this probe, a subwavelength aperture has also been created at the end of a tapered aluminum-coated single-mode fiber by focused ion beam milling [61]. Next, an air-gap of 40 nm is opened by focused ion beam milling in the coating. Such a split-probe is shown in the lower image of Fig. 6.1B. We compare the optical properties of a split-probe with a standard, cylindrically symmetric, coated probe (see upper image of Fig. 6.1B) that we successfully utilized in the past [13, 56, 57]. In order to make sure that we detect the magnetic field and not a complex combination of different components of the electric field, we employ a well characterized single-mode Si_3N_4 ridge waveguide as

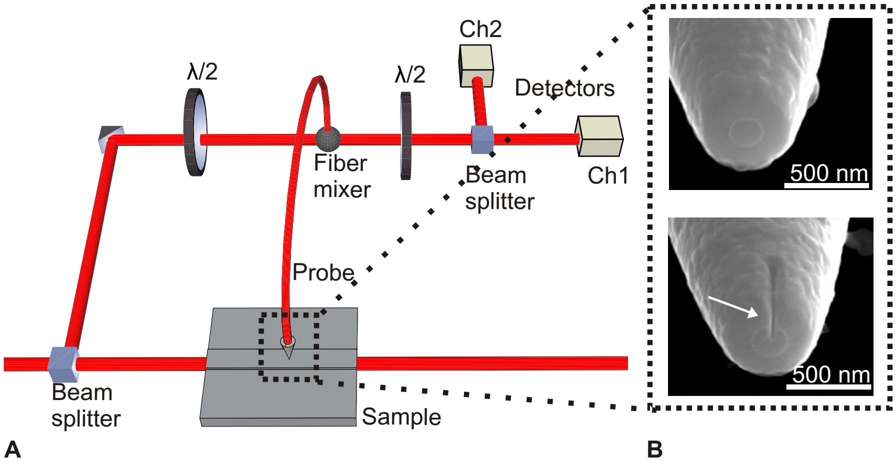

Figure 6.1:
A, *Schematic representation of the phase-sensitive near-field microscope. The near-field probe, indicated by the dashed box, is scanned 20 nm above the sample and collects through the aperture the evanescent field of the propagating light. Subsequently, the light is mixed with a reference branch of an interferometer. The resulting light is split by a polarizing beamsplitter and the two orthogonal polarizing components are detected with a heterodyne scheme. By suitably choosing the orientation of the two* $\lambda/2$ *waveplates, we can relate the signal at the two detectors, called Ch1 and Ch2, with the fields present in the sample.* **B**, *A scanning electron micrograph of the two aluminum coated near-field probes utilized in this work. For both probes the coating thickness is 150 nm and the aperture diameter is 200 to 230 nm. The upper image shows the highly cylindrical standard probe. The lower image shows a split-probe where an air-gap in the coating (indicated by the arrow) has been created.*

a test structure[1] (see Section 1.2). Linearly polarized light from a laser diode tuned to a wavelength of 1550 nm is coupled to the TE-mode of the waveguide. A homemade phase- and polarization-sensitive near-field

---

[1] Note that on one occasion patterns have been visualized in a relatively complex nanostructure that resemble the calculated patterns of the magnitude squared of the magnetic field. Devaux, E. *et al.* Phys. Rev. B **62**, 10504 (2000).

microscope is used for scanning and collecting the light [83], as shown in the schematic representation of the setup of Fig. 6.1A. The aperture of the probes couples the evanescent field of the light propagating through the waveguide to the probe-fiber [3]. The transverse electric fields of the collected light are mixed with the reference branch of a Mach-Zehnder interferometer. Subsequently, the two orthogonal polarizations are separated by a polarizing beamsplitter and simultaneously detected using a heterodyne scheme (see Section 2.2). By raster scanning the probe 20 nm above the sample, we obtain the amplitude and the phase distribution of the probed fields. In a recent publication [57] (see also Chapter 3), we exploited the high symmetry of the standard probe to distinguish the two in-plane components of the electric field of propagating light. As a result of the symmetry of the aperture, the in-plane components of the field couple to the orthogonal modes of the probe fiber and are detected in the two separate channels of the microscope (Ch1 and Ch2).

6.2.1 Measuring with a standard probe

We first characterize the waveguide performing near-field measurements with a standard probe. Figure 6.2A illustrates the geometry of the experiment. The light propagates along $\hat{x}$, the electric field is along $\hat{y}$, the magnetic field is along $\hat{z}$. Because the waveguide contains only a weakly guided TE-mode, the longitudinal component of the electric field is negligible (see Section 1.2) [15]. The probe can be considered as a subwavelength metallic ring parallel to the sample surface, because of its cylindrical symmetry and the fact that the extension of the evanescent fields in air is only $\simeq$ 100 nm [115]. The evanescent electric field component E_y induces a dipolar charge distribution in the probe (see Section 2.1). This induced oscillating dipole moment p_y couples to a propagating mode in the probe fiber and can be detected at the other end of the fiber. The magnetic field B_z, instead, generates a circular current in the ring, as described by Faraday's law. As a result, the probe exhibits a magnetic dipole moment m_z, in analogy with the magnetic response of a metallic cylinder [68]. However, the radiation pattern of the magnetic dipole lies in the xy-plane and the cylindrical symmetry of the system forbids coupling of this magnetic dipole to the propagating modes in the probe fiber that propagate along $\hat{z}$. Therefore, the fields detected with a standard probe are the in-plane electric fields [57, 72].

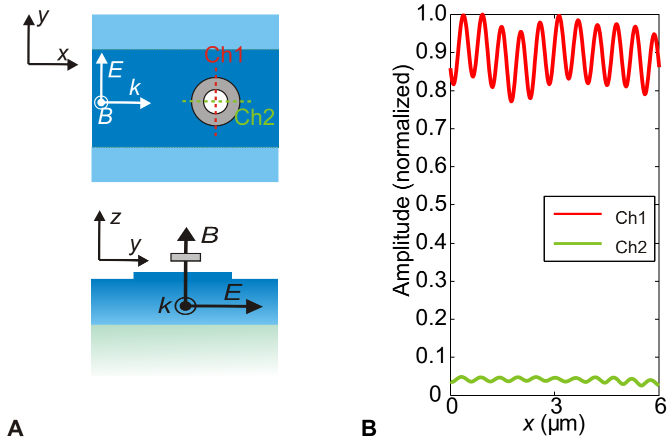

Figure 6.2:
A, *Schematic representation of the experiment performed with a standard probe, which is depicted in gray as a metallic ring. In the upper part, a top view is shown. The 'ridge' has been colored differently for clarity. In the lower part, a cross-section in the zy-plane is shown. The red and green axes correspond to Ch1 and Ch2, respectively.* **B**, *Line-traces of the amplitude obtained scanning a standard probe along the waveguide. The line traces are normalized to the maximum of Ch1. Both signals show a standing wave component.*

Figure 6.2B show the line-traces of the amplitude detected on Ch1 (red) and Ch2 (green), obtained by scanning the probe along the center of the waveguide. Because the only nonvanishing component of the electric field is along $\hat{y}$, we can attribute that the signal detected by Ch1 to E_y and the Ch2-signal thus corresponds to E_x (Fig. 6.2A). Because in the center of the waveguide the longitudinal component (E_x), actually, vanishes [15], Fig. 6.2B allows us to infer the experimental extinction ratio of the two polarization channels. Since the ratio between the two amplitude signals is $\sim 1/20$ (in terms of intensity $\sim 1/400$), we prove that we are able to properly separate the two polarization states. Furthermore, an evident oscillation is present in both channels. Because the spatial period ($\sim$ 500 nm) is half a wavelength in the waveguide (see sect. 1.2), we attribute this oscillation to a standing wave caused by the interference between the

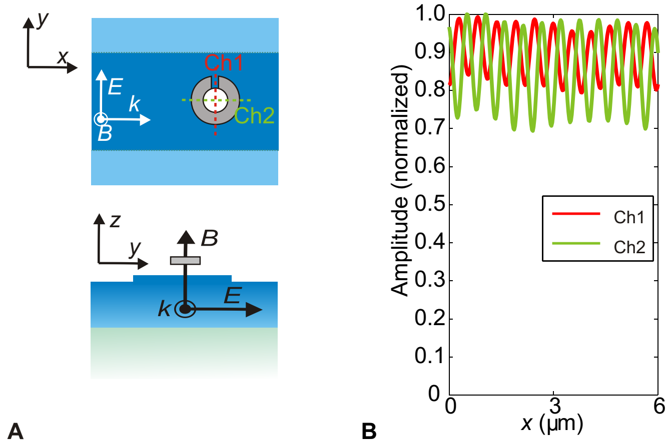

Figure 6.3:
A, *Schematic representation of the experiment performed with a split-probe, which is depicted in gray as a metallic split-ring. In the upper part, a top view is shown. The 'ridge' has been colored differently for clarity. In the lower part, a cross-section in the zy-plane is shown. The red and green axes correspond to Ch1 and Ch2, respectively.* **B**, *Line-traces of the amplitude obtained scanning a split-probe along the waveguide. The line traces are normalized to the maximum of Ch2. The Ch2-signal is comparable to Ch1 and the two standing wave patterns are spatially shift by half a period. We associate the Ch2-signal with* B_z.

forward propagating light and the small fraction of light that is reflected by the end-facet of the waveguide.

6.2.2 Measuring with a split-probe

The sensitivity of the probe to the various field components of light changes drastically when the new split-probe is employed. The air-gap is oriented along $\hat{y}$, as shown in Fig. 6.3A. In analogy to the standard probe, E_y and B_z will induce in the split-probe an electric and magnetic dipole moment p_y and m_z, respectively. Like for the cylindrical probe, the dipole moment p_y will generate an optical signal in Ch1. However, due to the air-gap, the magnetically induced current cannot flow completely around the ring and will produce a time-varying dipolar charge distribution across the gap.

The resulting electric dipole moment along $\hat{x}$ will oscillate in phase with the current and, thus, 90 degrees out of phase (*in quadrature*) with the driving magnetic field (see Section 2.1). In short, the probe will respond to B_z with an electric dipole moment $p_x \propto \mathrm{i}B_z$, analogous to the magnetic response of split-ring resonators [74,75]. This in-plane magnetically induced electric dipole moment can now couple to the fiber of the probe. Because the polarization of this radiation is along $\hat{x}$, the signal corresponding to B_z will be detected by Ch2. Hence, the optical signals with an electric and magnetic origin are detected in Ch1 and Ch2, respectively.

Figure 6.3B shows the measured amplitude of the Ch1- and Ch2-signal obtained with a split-probe. In contrast to Fig. 6.2B, the signals in the two channels have now comparable magnitude. The standing wave induced amplitude modulation of components of the two signals is roughly equal. However, the most important difference between Fig. 6.2B and 2D is that the maxima of the two standing waves are shifted in space by half a period. It is well known that in a standing light wave the amplitude of the magnetic field is shifted in space by half a period with respect to the amplitude of the electric field [2]. The spatial shift of the local maxima that we observe in Fig. 6.3B is therefore a clear signature that Ch2 detects the light generated by the coupling with B_z. Thus, we have detected the out-of-plane component of the magnetic field.

6.2.3 Additional experimental tests

To verify our claim of magnetic sensitivity of the probe, we perform two additional checks. First, we use the same split-probe to measure on a waveguide oriented along $\hat{y}$, while keeping the air-gap oriented along $\hat{y}$ (Fig. 6.4A). In order to measure with a rotated probe-ridge orientation, we use another waveguide with two straight sections connected by a 90 degrees bend. To guide the light across the bend a stronger effective refractive index contrast is required. This is achieved using a 300 nm thick Si_3N_4 substrate. This waveguide turns out to be single-mode for TE and TM. In this configuration the electric field is along $\hat{x}$, rather than $\hat{y}$, and, thus, it should be detected by Ch2. However, B_z should also be detected by Ch2, because the orientation of the probe and, consequently, of the magnetically induced electric dipole moment has not changed. This means that the channel with higher signal should now be Ch2. This is indeed experimentally observed, as shown in Fig. 6.4B. Although the ratio between the

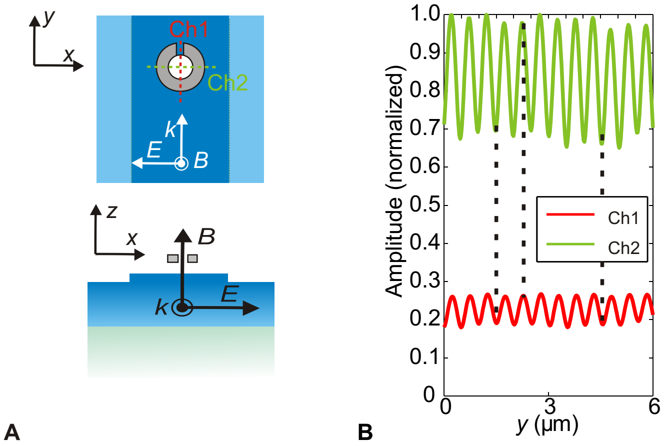

Figure 6.4:
A, *Schematic representation of the experiment performed with a split-probe, which is depicted in gray as a metallic split-ring. Same configuration than Fig. 6.3A but the waveguide is rotated by 90 degrees. In the upper part, a top view is shown. The 'ridge' has been colored differently for clarity. In the lower part, a cross-section in the zy-plane is shown. The red and green axes correspond to Ch1 and Ch2, respectively.* **B**, *Line-traces of the amplitude obtained scanning a split-probe along the waveguide. The line traces are normalized to the maximum of Ch2. Both E_x and B_z are projected along $\hat{x}$ and, thus, detected by Ch2. Consequently, the spatial shift of the standing wave patterns does not occur anymore.*

Ch1- and Ch2-signal is only $\simeq 0.27$ (in terms of intensity is $\simeq 0.07$), the ratio is higher than expected (see Fig. 6.2B). We attribute this to a minute in-plane rotation of the air-gap with respect to $\hat{y}$. When the air-gap is not perfectly aligned with $\hat{y}$, the probe projects a fraction of B_z on Ch1. More importantly, because in this configuration the split-probe does not separate E_x and B_z, the amplitude maxima of the two channels are no longer shifted in space with respect to each other, as indicated by the dashed lines in Fig. 6.4B.

As a second test, we analyze the phase difference $\Delta\phi$ between the complex signals in Ch1 and Ch2 when the conditions of the setup, such as the strain on the fibers, different probes and the orientation of the con-

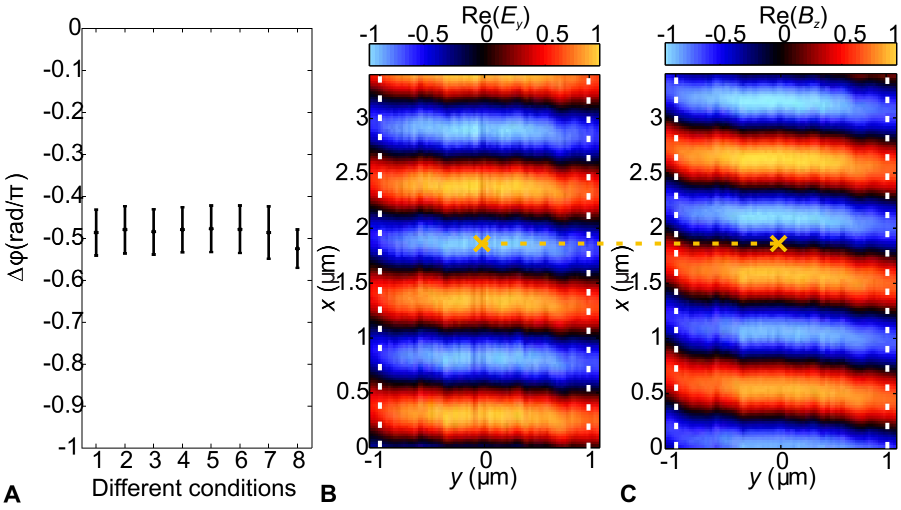

Figure 6.5:
A, *Phase difference $\Delta\phi$ between the complex signals of Ch1 and Ch2 for the measurement of Fig. 6.5B for different experimental conditions.* **B** *and* **C**, *Normalized Distributions of Re(E_y) and Re(B_z), respectively. The images have been obtained by raster scanning the split-probe in the configuration shown in Fig. 6.5B over an area 2.2×3.4 μm^2. The white dashed lines represent the position of the waveguide. The green dashed line is a guide to the eye that indicates the $\pi/2$ phase shift of the two wave fronts.*

nectors, are changed. We use the experimental configuration shown in Fig. 6.3A. The magnetically induced electric dipole moment should be $p_x \propto \mathrm{i}B_z$. Hence, considering that we are far below the resonance wavelength of the split-probe (we estimate a resonant wavelength of $\lambda_o = 1300$ nm and a width $\Delta\lambda_o = 50$ nm for the resonance based on methods for split-ring resonators (see Section 2.1) [68]), the Ch2-signal should be in quadrature with the driving magnetic field. Because B_z and E_y are in phase and Ch1 follows E_y, the Ch1-signal should therefore be in quadrature with the Ch2-signal. Figure 6.5A shows for different probe and setup conditions that we indeed consistently measure a constant phase difference $\Delta\phi = -\pi/2$ (with a spread of 10%).

6.3 Conclusion

We conclude by showing in Fig. 6.5B and C the distributions of the signals of Ch1 and Ch2 corresponding to real part of E_y and $\mathbf{i}B_z$, respectively, detected by raster scanning the split-probe in the experimental configuration of Fig. 6.3A. The white dashed lines represent the position of the waveguide. A closer look at the wave fronts in Fig. 6.5B and C shows that the two waves are shifted by $\pi/2$, where the green dashed lines can be used as guide to the eye. In this waveguide the longitudinal component E_x of the electric field is maximally 10% the transverse component E_y (see Section 1.2). E_x has an antisymmetric distribution with respect to the waveguide and its maximum amplitude is located close to the edge of the ridge. We attribute the slight asymmetry of Fig. 6.5C to the antisymmetric contribution of E_y to the B_z-signal detected on Ch2. These images demonstrate that we simultaneously visualize with phase-sensitivity and subwavelength resolution the magnetic and electric field distribution of light propagating through a ridge waveguide. We anticipate that the simultaneous spatially resolved detection of both magnetic and electric field will open up new fascinating research directions. By redesigning the geometry of the probe, it should be possible to detect other components of the light field, besides the three shown in this work. Furthermore, the split-probe can be used as a movable split-ring resonator and, thus, we can explore the local coupling between nano-objects that resonantly respond to the magnetic field at optical frequencies, such as split-ring resonators, double fishnet structures and stereometamaterials.

Conclusions & Outlook

In this work we presented a nanoscale experimental investigation of both magnetically and electrically induced light-matter interactions. Novel physical phenomena have been explored that we expect to contribute to the development of nano-optics. Here, we will briefly highlight future directions which directly stem from this work. Our intention is to give a glimpse of possible new research perspective and stimulate scientific discussions, rather than present detailed proposals for forthcoming investigations.

The results presented in Chapter 3 and in [29] open the way up for studies of near-field singular optics. As mentioned in Section 1.3.3, light singularities are associated with spin angular momentum and orbital angular momentum. Photonic structures with tailored field patterns where optical vortices and area of circular polarization are present at the nanoscale can be of interest for microfluidity. Micro- or nano-rods could be optically trapped in the near field of photonic structures, like a photonic crystal waveguide, immersed in a liquid. Light in the waveguide would transfer angular momentum to these rods, which would have a spin and/or an angular rotation. We can envision arrays of these rotating nanorods, each of them with different angular momenta, which can be used for mixing fluids at the nanoscale.

Control of the spin state of quantum emitters, such as quantum dots or molecules, can be achieved with photonic nanostructures. As shown in Chapter 3, a photonic crystal waveguide has a polarization distribution that changes handedness in few hundreds of nanometers. Placing molecules or quantum dots in these areas would provide an unprecedented control on the spin state at the nanoscale, which is important for future quantum applications.

In Chapter 4 we showed that we controlled the optical properties of a photonic crystal nanocavity by magnetic coupling between the near-field probe and the resonator. In particular, we decrease the loss of the cavity exploiting the destructive interference between the magnetically induced emission of the probe and the out-of-plane radiation of the cavity. This experiment suggests that we can combine photonic crystal and metamaterials concepts in order to increase the Q of the nanocavity. Metallic nanorings grown where the magnetic field of an ultra-high-Q [22] nanocavity is maximum would act as a 'magnetic mirror' which reflects back into the cavity the 'lost' radiation. Despite the ohmic losses introduced by the metal, the overall quality of these state-of-the-art nanocavities will increase and the mode volume will decrease, as shown in Chapter 4, leading to an higher Q/V.

The fact that a coated probe exhibits a magnetic response suggests that we can measure the magnetic field performing scattering-Scanning Near-Field Microscopy (sSNOM). Instead of the standard AFM-probe employed in sSNOM, we can use a coated probe which scatters the vertical component of the magnetic field of light. The light generated by this scattering event would skim along the surface of the sample and can be detected, in analogy with sSNOM methodologies.

In Chapter 6 we showed that a properly functionalized coated probe can couple the magnetic field of light to propagating mode in the probe-fiber. Consequently, we detected the magnetic field at optical frequencies. This experiment suggests that we can measure also all the other field components at optical frequencies, obtaining the full characterizations of propagating light. With modern fabrication technologies, for example focused ion beam milling, we can engineer the apex of a coated probe such that it could be more sensitive to some fields and less to others. The only fundamental restriction is given by the nature of the modes in the fiber-probe. Because there are only two orthogonal modes in a single-mode fiber, only two fields per fiber can be independently detected. Alternatively, we can envision to use a multimode fiber and create a probe apex that couples each field to a different mode of the fiber. Although in principle possible, this option does not seem to be realistic. However, the simultaneous measurements of orthogonal electric and magnetic field already offers new fascinating challenges. In fact, it has been suggested that a Heisenberg's uncertainty principle might hold for electric and magnetic field [134]. By performing near-field measurements with a split-probe at the single-photon level, it would be possible to explore the validity of such inequality.

Appendix A

Shifting of the resonance frequency

In chapter 4 we calculated the shift of the resonance of a photonic crystal nanocavity induced by coated probe exploiting eq. 4.1. In this appendix we will first derive the relative frequency shift of a photonic crystal eigenmode induced by a subwavelength object placed in close proximity. Secondly, we will calculate the resonance shift for the experimental configuration described in chapter 4 and we will derive eq. 4.1.

A.1 Frequency shift induced by a subwavelength object

Let us consider a photonic crystal with dielectric constant $\varepsilon_{\mathrm{pc}}(\mathbf{r})$ and that the magnetic field $\boldsymbol{H}_{\mathrm{o}}$ is an eigenmode of an unperturbed system with eigenvalue ω_{o}. Thus, the so-called *master equation* for photonic crystals must be fulfilled [17]

$$\hat{M}_{\mathrm{o}}\boldsymbol{H}_{\mathrm{o}} = \frac{\omega_{\mathrm{o}}}{c}^{2}\boldsymbol{H}_{\mathrm{o}}, \tag{A.1}$$

where $\hat{M}_{\mathrm{o}} = \boldsymbol{\nabla} \times (\varepsilon_{\mathrm{pc}}^{-1}(\mathbf{r})\boldsymbol{\nabla}\times)$ and c is the speed of light in vacuum. Let us now assume that a nano-object with dielectric constant ε_{p} is placed at position $\mathbf{r}_{\mathrm{o}}$ in close proximity to the photonic crystal. We also can write a master equation for the object-photonic crystal system at position $\mathbf{r}_{\mathrm{o}}$, eigenmode $\boldsymbol{H}$ and eigenvalue $\omega = \omega_{\mathrm{o}} + \Delta\omega$. As the electric susceptibilities of the photonic crystal and of the probe sum up, the dielectric function at position $\mathbf{r}_\mathrm{o}$ becomes $\varepsilon = \varepsilon_\mathrm{pc}(\mathbf{r}_\mathrm{o}) + \varepsilon_\mathrm{p} - 1$ and thus

$$\hat{M}\boldsymbol{H} = \frac{\omega_\mathrm{o}}{c}^2\boldsymbol{H}, \tag{A.2}$$

where $\hat{M} = \boldsymbol{\nabla} \times (\varepsilon^{-1}(\mathbf{r})\boldsymbol{\nabla}\times)$. Hence, from the difference between e.q A.1 and A.2 we obtain

$$\langle \boldsymbol{H}_\mathrm{o}, (\hat{M} - \hat{M}_\mathrm{o})\boldsymbol{H}\rangle = \frac{(\omega^2 - \omega_\mathrm{o}^2)}{c^2}\langle \boldsymbol{H}_\mathrm{o}, \boldsymbol{H}\rangle, \tag{A.3}$$

where $\langle \boldsymbol{f}, \boldsymbol{g}\rangle = \int \boldsymbol{f}^*\boldsymbol{g}\mathrm{d}^3\boldsymbol{x}$ is the scalar product of two complex fields $\boldsymbol{f}$ and $\boldsymbol{g}$. In order to express eq. A.3 in terms of electric fields, we make use of the relation $\langle \boldsymbol{f}, \boldsymbol{\nabla} \times \boldsymbol{g}\rangle = \langle \boldsymbol{\nabla} \times \boldsymbol{f}, \boldsymbol{g}\rangle$. The left side of the eq. A.3 can be written as

$$\begin{aligned}\langle \boldsymbol{H}_\mathrm{o}, (\hat{M} - \hat{M}_\mathrm{o})\boldsymbol{H}\rangle &= \frac{1}{c^2}\langle -\mathrm{i}\omega_\mathrm{o}\varepsilon_\mathrm{pc}\varepsilon_\mathrm{o}\boldsymbol{E}_\mathrm{o}, -(\frac{1}{\varepsilon} - \frac{1}{\varepsilon_\mathrm{pc}})\mathrm{i}\omega\varepsilon\varepsilon_\mathrm{o}\boldsymbol{E}\rangle = \\ &= -\frac{1}{c^2}\omega\omega_\mathrm{o}\varepsilon_\mathrm{o}^2\langle \boldsymbol{E}_\mathrm{o}, (\varepsilon - \varepsilon_\mathrm{pc})\boldsymbol{E}\rangle, \end{aligned} \tag{A.4}$$

where ε_o is the electric permittivity of vacuum and we made use of the Maxwell equation $\boldsymbol{\nabla} \times \boldsymbol{H} = -\mathrm{i}\omega\varepsilon\varepsilon_\mathrm{o}\boldsymbol{E}$.

The right side of eq. A.3 can be written as

$$\begin{aligned}\frac{(\omega^2 - \omega_\mathrm{o}^2)}{c^2}\langle \boldsymbol{H}_\mathrm{o}, \boldsymbol{H}\rangle &= \frac{(\omega^2 - \omega_\mathrm{o}^2)}{c^2}\langle \frac{1}{\mathrm{i}\omega_\mathrm{o}\mu_\mathrm{o}}\boldsymbol{\nabla} \times \boldsymbol{E}_\mathrm{o}, \frac{1}{\mathrm{i}\omega\mu_\mathrm{o}}\boldsymbol{\nabla} \times \boldsymbol{E}\rangle = \\ &= \frac{\omega^2 - \omega_\mathrm{o}^2}{\omega\omega_\mathrm{o}\mu_\mathrm{o}^2c^2}\langle \boldsymbol{\nabla} \times \boldsymbol{\nabla} \times \boldsymbol{E}_\mathrm{o}, \boldsymbol{E}\rangle = \frac{(\omega^2 - \omega_\mathrm{o}^2)\omega_\mathrm{o}^2}{\omega\omega_\mathrm{o}\mu_\mathrm{o}^2c^4}\langle \varepsilon_\mathrm{pc}\boldsymbol{E}_\mathrm{o}, \boldsymbol{E}\rangle = \\ &= \frac{(\omega^2 - \omega_\mathrm{o}^2)\omega_\mathrm{o}}{\omega\mu_\mathrm{o}^2c^4}\langle \varepsilon_\mathrm{pc}\boldsymbol{E}_\mathrm{o}, \boldsymbol{E}\rangle, \end{aligned} \tag{A.5}$$

where μ_o is the magnetic permeability of vacuum and we made use of the Maxwell equation $\boldsymbol{\nabla} \times \boldsymbol{E} = \mathrm{i}\omega\mu_\mathrm{o}\boldsymbol{H}$ and of the master equation for the electric field $c^2\varepsilon_\mathrm{pc}^{-1}(\mathbf{r})(\boldsymbol{\nabla} \times \boldsymbol{\nabla} \times \boldsymbol{E}) = \omega^2\boldsymbol{E}$. Putting eq. (A.3), (A.4), and (A.5) together yields the relation

$$\frac{\omega^2 - \omega_\mathrm{o}^2}{\omega^2} = \frac{2\omega_\mathrm{o}\Delta\omega + (\Delta\omega)^2}{\omega_\mathrm{o}^2 + 2\omega_\mathrm{o}\Delta\omega + (\Delta\omega)^2} = -\frac{\langle \boldsymbol{E}_\mathrm{o}, (\varepsilon - \varepsilon_\mathrm{pc})\boldsymbol{E}\rangle}{\langle \boldsymbol{E}_\mathrm{o}, \varepsilon_\mathrm{pc}\boldsymbol{E}\rangle}. \tag{A.6}$$

A.2 Derivation of equation 4.1

As we experimentally verified in Chapter 4, our coated probe induces only a minute ($\sim 10^{-4}$) relative frequency shift of the resonance of the cavity. As a consequence we can consider $\omega_o \gg \Delta\omega$ and thus [135]

$$\frac{2\Delta\omega}{\omega_{\mathrm{o}}} \approx -\frac{\langle \boldsymbol{E}_{\mathrm{o}}, (\varepsilon - \varepsilon_{\mathrm{pc}})\boldsymbol{E} \rangle}{\langle \boldsymbol{E}_{\mathrm{o}}, \varepsilon_{\mathrm{pc}}\boldsymbol{E} \rangle}. \tag{A.7}$$

The current density induced by an electric field in the coated probe is $\boldsymbol{J}_{\mathrm{p}} = (1 - \varepsilon_{\mathrm{p}})\mathrm{i}\omega_{\mathrm{o}}\varepsilon_{\mathrm{o}}\boldsymbol{E}$ and $\varepsilon - \varepsilon_{\mathrm{pc}} = \varepsilon_{\mathrm{p}} - 1$. Thus, we can write that

$$(\varepsilon - \varepsilon_{\mathrm{pc}})\boldsymbol{E} = \frac{\mathrm{i}}{\omega_{\mathrm{o}}\varepsilon_{\mathrm{o}}}\boldsymbol{J}_{\mathrm{p}}. \tag{A.8}$$

Combining eq. (A.7) and (A.8) we obtain

$$\Delta\omega \approx -\frac{\mathrm{i}}{2\varepsilon_{\mathrm{o}}}\frac{\langle \boldsymbol{E}_{\mathrm{o}}, \boldsymbol{J}_{\mathrm{p}} \rangle}{\langle \boldsymbol{E}_{\mathrm{o}}, \varepsilon_{\mathrm{pc}}\boldsymbol{E} \rangle} = -\frac{\mathrm{i}}{2\varepsilon_{\mathrm{o}}}\frac{\int \boldsymbol{E}_{\mathrm{o}}^* \cdot \boldsymbol{J}_{\mathrm{p}}\mathrm{d}^3\mathbf{x}}{\int \varepsilon_{\mathrm{pc}}\boldsymbol{E}_{\mathrm{o}}^* \cdot \boldsymbol{E}\mathrm{d}^3\mathbf{x}} = -\frac{\mathrm{i}\int \boldsymbol{E}_{\mathrm{o}}^* \cdot \boldsymbol{J}_{\mathrm{p}}\mathrm{d}^3\mathbf{x}}{2U_E}. \tag{A.9}$$

Because the diameter of the probe is smaller than the wavelength, we restrict ourselves to the lowest multipole moments of $\boldsymbol{J}_{\mathrm{p}}$, which are the probe's electric and magnetic dipole moments $\boldsymbol{p}$ and $\boldsymbol{m}$, respectively (see Section 2.1). We obtain [2]

$$\int \boldsymbol{E}_{\mathrm{o}}^* \cdot \boldsymbol{J}_{\mathrm{p}}\mathrm{d}^3\mathbf{x} = -\mathrm{i}\omega_{\mathrm{o}}\boldsymbol{E}_{\mathrm{o}}^* \cdot \boldsymbol{p} - \mathrm{i}\omega_{\mathrm{o}}\boldsymbol{B}_{\mathrm{o}}^* \cdot \boldsymbol{m}. \tag{A.10}$$

Insertion of A.10 into A.9 then yields the desired result

$$\Delta\omega \approx -\frac{\omega_{\mathrm{o}}\boldsymbol{E}_{\mathrm{o}}^* \cdot \boldsymbol{p} + \omega_{\mathrm{o}}\boldsymbol{B}_{\mathrm{o}}^* \cdot \boldsymbol{m}}{2U_E}, \tag{A.11}$$

which is equal to eq. 4.1.

Appendix B

Choosing the unit system

B.1 Introduction

The choice of the 'right' unit system to use in optics was under debate during most part of the last century. Among the others, the Gaussian (CGS) system and the International System (SI) were the most common. The initially employed unit system was the CGS system and the introduction of the SI system was not unanimously accepted. J. A. Stratton wrote in the 1941 that "... There is still the felling among many physicists that this system [the SI system] is being forced upon them by a subversive group of engineers." [136]. J. D. Jackson published the first two editions of his *Classical Electrodynamics*, one of the most celebrated textbook of electromagnetism, in Gaussian units. Only after 36 years, in the third edition, he employed the SI system but only for part of the book. One of the reason for such a late adoption can be said with Jackson's words: "...Ed Purcell and I [Jackson] had a pact to support each other in the use of Gaussian units..." [2]. Analogously, L. D. Landau and E. M. Lifshitz' *Electrodynamics of continuous media* and M. Born and E. Wolf's *Principle of optics* are still published in CGS units. However, these are the last 'tories' who try to support the use of CGS in textbooks. Nowadays, the SI system apparently won the controversy. In fact, besides few exceptions, the SI system is employed in all textbooks for physicists and engineers.

Both CGS and SI are 'absolute' unit system, which means that every quantity can be expressed in terms of mass (M), length (L) and time (T). To achieve an absolute unit system in electromagnetism three proportionality constants must be introduced. It can be shown that the unit of a charge q and of a magnetic dipole moment $\boldsymbol{m}$ are

$$[q] = \varepsilon_{\text{o}}^{1/2} M^{1/2} L^{3/2} T^{-1}, \tag{B.1}$$

$$[\boldsymbol{m}] = \mu_{\text{o}}^{-1/2} M^{1/2} L^{5/2} T^{-1}, \tag{B.2}$$

where ε_{o} and μ_{o} are the electric permittivity and magnetic permeability of vacuum, respectively. Moreover, from the fact that the magnetic dipole moment of a metallic coil is proportional to the current I flowing through it, we obtain

$$[\boldsymbol{m}] = \gamma^{-1}[I]L^2 = \gamma^{-1}\varepsilon_{\text{o}}^{1/2} M^{1/2} L^{7/2} T^{-2}. \tag{B.3}$$

where γ^{-1} is the proportionality constant. For a more detailed discussion see [136]. By combining eq. B.2 and B.3 we obtain

$$\frac{\gamma}{\sqrt{\varepsilon_{\text{o}}\mu_{\text{o}}}} = \frac{L}{T} = c, \tag{B.4}$$

where c is the speed of light in vacuum (299,792,458 meters per second). Nowadays, c is a quantity *defined* rather than measured and used as basis for the unit of length[1]. The choice of the parameters γ, ε_{o} and μ_{o} sets the employed unit system and must be such that eq. B.4 is always fulfilled. In SI units $\gamma = 1$, $\varepsilon_{\text{o}} = 8.854 \cdot 10^{-12}$ F/m and $\mu_{\text{o}} = 4\pi \cdot 10^{-7}$ H/m. In contrast, in CGS system $\gamma = c$, $\varepsilon_{\text{o}} = 1$ and $\mu_{\text{o}} = 1$, such that ε_{o} and μ_{o} are dropped out of the Maxwell equations and c is introduced.

As a result, the SI system is more 'practical' for measurements. In fact, the CGS system provides far too small units for typical quantities in electronics, such as resistance. Also, the CGS units are less intuitive. In the Gaussian system the capacitance is expressed in cm, the resistance in s$\cdot$cm^{-1} and the inductance in cm$^{-1}\cdot$s^{-2}, which do not seem to provide an intuitive description of these quantities. As yet the CGS units have been supplanted by the SI system, primarily because of practical reasons.

However, the Gaussian system has an interesting and useful property. As a result of the normalization of μ_{o} and ε_{o}, the magnetic and electric quantities have the same unit, emphasizing that they are two faces of the

---

[1] "The metre is the length of the path traveled by light in vacuum during a time interval of $1/299,792,458$ of a second", quoted from *The International System of Units (SI)*, International Bureau of Weights and Measures (2006).

same coin: light. For example, both electric ad magnetic field are expressed in $g^{1/2}cm^{-1/2}s^{-1}$ and both electric and magnetic polarizability are volumes (cm^3). Because in light-matter interaction the magnetic coupling generally plays a negligible role (see chapter 1), this aspect of the CGS system is often considered not relevant. With advent of metamaterials, however, the Gaussian system could come into favor again. These materials exhibit a magnetic response at optical frequencies comparable with the electric response and a direct comparison of the magnetic and electric quantities is often useful.

B.2 Conversion formulas from CGS to SI units

Here, we show the Maxwell equations in CGS and SI units and some conversion formulas from one system to the other. In the following, plain symbols a denote CGS quantities, overlined symbols $\bar{a}$ indicate SI quantities. The Maxwell equations are

$$\begin{array}{rclrcl} \boldsymbol{\nabla}\cdot\boldsymbol{B} & = & 0, & \boldsymbol{\nabla}\cdot\bar{\boldsymbol{B}} & = & 0 \\ \boldsymbol{\nabla}\cdot\boldsymbol{E} & = & 4\pi\rho, & \boldsymbol{\nabla}\cdot\bar{\boldsymbol{E}} & = & \varepsilon_o^{-1}\bar{\rho} \\ \boldsymbol{\nabla}\times\boldsymbol{B} & = & 4\pi c^{-1}\boldsymbol{J}+c^{-1}\partial_t\boldsymbol{E}, & \boldsymbol{\nabla}\times\bar{\boldsymbol{B}} & = & \mu_o\bar{\boldsymbol{J}}+c^{-2}\partial_t\bar{\boldsymbol{E}} \\ \boldsymbol{\nabla}\times\boldsymbol{E} & = & -c^{-1}\partial_t\boldsymbol{B}, & \boldsymbol{\nabla}\times\bar{\boldsymbol{E}} & = & -\partial_t\bar{\boldsymbol{B}} \end{array} \tag{B.5}$$

where $\boldsymbol{E}$ is the electric field, $\boldsymbol{B}$ is the magnetic field, ρ is the charge density and $\boldsymbol{J}$ is the current density.

By defining $\kappa = (4\pi\varepsilon_o)^{1/2}$ and considering that $c = (\varepsilon_o\mu_o)^{-1/2}$ (SI system), we obtain the following conversion formulas

$$\begin{array}{rclrcl} \bar{\rho} & = & \kappa\rho, & \bar{\boldsymbol{J}} & = & \kappa\boldsymbol{J} \\ \bar{\boldsymbol{E}} & = & \kappa^{-1}\boldsymbol{E}, & \bar{\boldsymbol{B}} & = & (c\kappa)^{-1}\boldsymbol{B}, \\ \bar{\boldsymbol{P}} & = & \kappa\boldsymbol{P}, & \bar{\boldsymbol{M}} & = & c\kappa\boldsymbol{M}, \end{array} \tag{B.6}$$

where the last two equations also hold for electric and magnetic dipole moments, respectively.

The parameters which describe the linear response of matter can be converted using

$$\begin{array}{rclrcl} \bar{\chi}_e & = & 4\pi\chi_e, & \bar{\chi}_m & = & 4\pi\chi_m, \\ \bar{\alpha}^{ee} & = & \kappa^2\alpha^{ee}, & \bar{\alpha}^{mm} & = & (c\kappa)^2\alpha^{mm}, \\ \bar{\sigma} & = & \kappa^2\sigma, & & & \end{array} \tag{B.7}$$

where χ_{e} and χ_{m} are the electric and magnetic susceptibility, respectively, α^{ee} and α^{mm} the electric and magnetic polarizability, respectively, and σ is the conductivity of a metal.

To conclude, we obtain for the nonlinear response of matter

$$\bar{\chi}_{\mathrm{e}}^{(l)} \quad = \quad 4\pi\kappa^{l-1}\chi_{\mathrm{e}}^{(l)}, \qquad \bar{\chi}_{\mathrm{e}}^{(l)} \quad = \quad 4\pi\kappa^{l-1}\chi_{\mathrm{e}}^{(l)} \tag{B.8}$$

where the label l indicate the nonlinear order of the susceptibility.

Bibliography

[1] N. W. Ashcroft and N. D. Mermin. *Solid State Physics*. Brooks Cole (1976).

[2] J. D. Jackson. *Classical Electrodynamics*. Butterworth-Heinemann, 3rd edn. (1984).

[3] L. Novotny and B. Hecht. *Principles of Nano-Optics*. Cambridge University Press, Cambridge (2006).

[4] J. G. Rivas, M. Kuttge, H. Kurz, P. H. Bolivar and J. A. Sanchez-Gil. *Low-frequency active surface plasmon optics on semiconductors*. App. Phys. Lett. **88**, 082106 (2006).

[5] L. D. Landau and E. M. Lifshitz. *Electrodynamics of continuous media*. Wiley (1984).

[6] D. Senff, P. Link, K. Hradil, A. Hiess, L. P. Regnault, Y. Sidis, N. Aliouane, D. N. Argyriou and M. Braden. *Magnetic excitations in multiferroic* $TbMnO_3$*: Evidence for a hybridized soft mode*. Phys. Rev. Lett. **98**, 137206 (2007).

[7] S. L. Oliveira and S. C. Rand. *Intense nonlinear magnetic dipole radiation at optical frequencies: Molecular scattering in a dielectric liquid*. Phys. Rev. Lett. **98**, 093901 (2007).

[8] M. Born and E. Wolf. *Principle of optics*. Cambridge University Press, Cambridge, 7th edn (1999).

[9] J. Valentine, S. Zhang, T. Zentgraf, E. Ulin-Avila, D. A. Genov, G. Bartal and X. Zhang. *Three-dimensional optical metamaterial with a negative refractive index*. Nature **455**, 376 (2008).

[10] D. R. Smith, J. B. Pendry and M. C. K. Wiltshire. *Metamaterials and negative refractive index.* Science **305**, 788 (2004).

[11] D. Schurig, J. J. Mock, B. J. Justice, S. A. Cummer, J. B. Pendry, A. F. Starr and D. R. Smith. *Metamaterial electromagnetic cloak at microwave frequencies.* Science **314**, 977 (2006).

[12] J. B. Pendry, D. Schurig and D. R. Smith. *Controlling electromagnetic fields.* Science **312**, 1780 (2006).

[13] R. J. P. Engelen, Y. Sugimoto, H. Gersen, N. Ikeda, K. Asakawa and L. Kuipers. *Ultrafast evolution of photonic eigenstates in k-space.* Nature Phys. **3**, 401 (2007).

[14] Y. Akahane, T. Asano, B. S. Song and S. Noda. *High-Q photonic nanocavity in a two-dimensional photonic crystal.* Nature **425**, 944 (2003).

[15] A. W. Snyder and J. Love. *Optical waveguide theory.* Springer, 1st edn (1983).

[16] O. Ivanova, R. Stoffer, M. Hammer and E. van Groesen. *A vectorial variational mode solver and its application to piecewise constant and diffused waveguides.* MMET 2008. 12th International Conference pages 495–497 (2008).

[17] J. D. Joannopoulos, S. G. Johnson, J. N. Winn and R. D. Meade. *Photonic Crystals: Molding the Flow of Light.* Princeton University Press, Princeton, 2nd edn.

[18] R. J. P. Engelen. *Ultrafast investigations of slow light in photonic crystal structures.* PhD Thesis, University of Twente, Twente (2009).

[19] T. Asano, B. S. Song, Y. Akahane and S. Noda. *Ultrahigh-Q nanocavities in two-dimensional photonic crystal slabs.* IEEE J. Sel. Top. Quantum Electron. **12**, 1123 (2006).

[20] T. Tanabe, M. Notomi, E. Kuramochi, A. Shinya and H. Taniyama. *Trapping and delaying photons for one nanosecond in an ultrasmall high-Q photonic-crystal nanocavity.* Nature Photon. **1**, 49 (2007).

[21] E. Kuramochi, H. Taniyama, T. Tanabe, A. Shinya and M. Notomi. *Ultrahigh-Q two-dimensional photonic crystal slab nanocavities in very thin barriers.* App. Phys. Lett. **93**, 111112 (2008).

[22] Y. Takahashi, H. Hagino, Y. Tanaka, B. Song, T. Asano and S. Noda. *High-Q nanocavity with a 2-ns photon lifetime.* Opt. Express **15**, 17206 (2007).

[23] C. Manolatou, M. Khan, S. Fan, P. Villeneuve, H. Haus and J. Joannopoulos. *Coupling of modes analysis of resonant channel add-drop filters.* IEEE J. Quantum Electron. **35**, 1322 (1999).

[24] J. F. Nye and M. V. Berry. *Dislocations in wave trains.* Proc. R. Soc. A **336**, 165 (1974).

[25] J. F. Nye. *Lines of circular polarization in electromagnetic wave fields.* Proc. R. Soc. A (1934-1990) **389**, 279 (1983).

[26] J. F. Nye. *Polarization effects in the diffraction of electromagnetic waves: The role of disclinations.* Proc. R. Soc. A (1934-1990) **387**, 105 (1983).

[27] J. F. Nye. *Natural focusing and fine structure of light.* Institute of Physics, Bristol (1999).

[28] M. R. Dennis. *Polarization singularities in paraxial vector fields: morphology and statistics.* Opt. Commun. **213**, 201 (2002).

[29] S. Vignolini, M. Burresi, S. Gottardo, L. Kuipers and D. S. Wiersma. *Vortex and field correlation in the near-field of a three dimensional disordered photonic crystal.* in preparation (2009).

[30] M. L. M. Balistreri, J. P. Korterik, L. Kuipers and N. F. van Hulst. *Local observations of phase singularities in optical fields in waveguide structures.* Phys. Rev. Lett. **85**, 294 (2000).

[31] B. Vohnsen and S. I. Bozhevolnyi. *Comment on "Local observations of phase singularities in optical fields in waveguide structures".* Phys. Rev. Lett. **87**, 259401 (2001).

[32] N. van Hulst, M. Balistreri, J. Korterik and Kuipers. *Reply to comment on "Local observations of phase singularities in optical fields in waveguide structures"*. Phys. Rev. Lett. **87**, 259402 (2001).

[33] A. Nesci, R. Dndliker, M. Salt and H. P. Herzig. *Measuring amplitude and phase distribution of fields generated by gratings with subwavelength resolution.* Opt. Comm. **205**, 229 (2002).

[34] I. Freund, A. I. Mokhun, M. S. Soskin, O. V. Angelsky and I. I. Mokhun. *Stokes singularity relations.* Opt. Lett. **27**, 545 (2002).

[35] W. Wang, S. G. Hanson, Y. Miyamoto and M. Takeda. *Experimental investigation of local properties and statistics of optical vortices in random wave fields.* Phys. Rev. Lett. **94**, 103902 (2005).

[36] R. I. Egorov, M. S. Soskin, D. A. Kessler and I. Freund. *Experimental measurements of topological singularity screening in random paraxial scalar and vector optical fields.* Phys. Rev. Lett. **100**, 103901 (2008).

[37] M. Berry. *Making waves in physics.* Nature **403**, 21 (2000).

[38] M. V. Berry. *Geometry of phase and polarization singularities illustrated by edge diffraction and the tides.* Proc. SPIE Vol. **4403**, 1 (2001).

[39] R. A. Gray, A. M. Pertsov and J. Jalife. *Spatial and temporal organization during cardiac fibrillation.* Nature **392**, 75 (1998).

[40] P. G. de Gennes and J. Prost. *The Physics of Liquid Crystals.* Oxford University Press, Oxford, 2nd edn. (1995).

[41] L. Allen, M. W. Beijersbergen, R. J. C. Spreeuw and J. P. Woerdman. *Orbital angular momentum of light and the transformation of Laguerre-Gaussian laser modes.* Phys. Rev. A **45**, 8185 (1992).

[42] N. B. Simpson, K. Dholakia, L. Allen and M. J. Padgett. *Mechanical equivalence of spin and orbital angular momentum of light: an optical spanner.* Opt. Lett. **22**, 52 (1997).

[43] R. A. Beth. *Mechanical detection and measurement of the angular momentum of light.* Phys. Rev. **50**, 115 (1936).

[44] I. Fushman, D. Englund, A. Faraon, N. Stoltz, P. Petroff and J. Vuckovic. *Controlled phase shifts with a single quantum dot.* Science **320**, 769 (2008).

[45] A. T. O'Neil, I. MacVicar, L. Allen and M. J. Padgett. *Intrinsic and extrinsic nature of the orbital angular momentum of a light beam.* Phys. Rev. Lett. **88**, 053601 (2002).

[46] E. H. Singe. *A suggested model for extending microscopic resolution into the ultra-microscopy region.* Phil. Mag. **6**, 356 (1928).

[47] E. A. Ash and G. Nicholls. *Super-resolution aperture scanning microscope.* Nature **237**, 510 (1972).

[48] S. Vignolini. *Sub-wavelength probing and modification of complex photonic structures.* PhD Thesis, University of Florence, Florence (2008).

[49] E. Betzig, P. L. Finn and J. S. Weiner. *Combined shear force and near-field scanning optical microscopy.* App. Phys. Lett. **60**, 2484 (1992).

[50] A. G. T. Ruiter, J. A. Veerman, K. O. van der Werf and N. F. van Hulst. *Dynamic behavior of tuning fork shear-force feedback.* Appl. Phy. Lett. **71**, 28 (1997).

[51] A. F. Koenderink, M. Kafesaki, B. C. Buchler and V. Sandoghdar. *Controlling the resonance of a photonic crystal microcavity by a Near-Field probe.* Phys. Rev. Lett. **95**, 153904 (2005).

[52] S. I. Bozhevolnyi and L. Kuipers. *Near-field characterization of photonic crystal waveguides.* Semicond. Sci. Technol. **21**, R1 (2006).

[53] M. Sandtke and L. Kuipers. *Slow guided surface plasmons at telecom frequencies.* Nature Photon. **1**, 573 (2007).

[54] E. Chow, S. Y. Lin, J. R. Wendt, S. G. Johnson and J. D. Joannopoulos. *Quantitative analysis of bending efficiency in photonic-crystal waveguide bends at* λ*=1.55* μ*m wavelengths.* Opt. Lett. **26**, 286 (2001).

[55] H. Gersen, T. J. Karle, R. J. P. Engelen, W. Bogaerts, J. P. Korterik, N. F. van Hulst, T. F. Krauss and L. Kuipers. *Real-space observation of ultraslow light in photonic crystal waveguides.* Phys. Rev. Lett. **94**, 073903 (2005).

[56] H. Gersen, T. J. Karle, R. J. P. Engelen, W. Bogaerts, J. P. Korterik, N. F. van Hulst, T. F. Krauss and L. Kuipers. *Direct observation of bloch harmonics and negative phase velocity in photonic crystal waveguides.* Phys. Rev. Lett. **94**, 123901 (2005).

[57] M. Burresi, R. J. P. Engelen, A. Opheij, D. van Oosten, D. Mori, T. Baba and L. Kuipers. *Observation of polarization singularities at the nanoscale.* Phys. Rev. Lett. **102**, 033902 (2009).

[58] A. Ishimaru, S. W. Lee, Y. Kuga and V. Jandhyala. *Generalized constitutive relations for metamaterials based on the quasi-static lorentz theory.* IEEE Trans. Antennas Propag. **51**, 2550 (2003).

[59] R. Stockle, C. Fokas, V. Deckert, R. Zenobi, B. Sick, B. Hecht and U. P. Wild. *High-quality near-field optical probes by tube etching.* App. Phys. Lett. **75**, 160 (1999).

[60] G. A. Valaskovic, M. Holton and G. H. Morrison. *Parameter control, characterization, and optimization in the fabrication of optical fiber near-field probes.* App. Opt. **34**, 1215 (1995).

[61] J. A. Veerman, A. M. Otter, L. Kuipers and N. F. van Hulst. *High definition aperture probes for near-field optical microscopy fabricated by focused ion beam milling.* App. Phys. Lett. **72**, 3115 (1998).

[62] Y. C. Chang, J. Y. Chu, T. J. Wang, M. W. Lin, J. T. Yeh and J. K. Wang. *Fourier analysis of surface plasmon waves launched from single nanohole and nanohole arrays: unraveling tip-induced effects.* Opt. Express **16**, 740 (2008).

[63] B. Deutsch, R. Hillenbrand and L. Novotny. *Near-field amplitude and phase recovery using phase-shifting interferometry.* Opt. Express **16**, 494 (2008).

[64] D. V. Labeke and D. Barchiesi. *Probes for scanning tunneling optical microscopy: a theoretical comparison.* J. Opt. Soc. Am. A **10**, 2193 (1993).

[65] J. C. Weeber, F. de Fornel and J. P. Goudonnet. *Numerical study of the tip-sample interaction in the photon scanning tunneling microscope.* Opt. Commun. **126**, 285 (1996).

[66] P. Blattner, H. P. Herzig and R. Dandliker. *Scanning near-field optical microscopy: transfer function and resolution limit.* Opt. Commun. **155**, 245 (1998).

[67] H. Fischer, A. Nesci, G. Leveque and O. Martin. *Characterization of the polarization sensitivity anisotropy of a near-field probe using phase measurements.* Journal of Microscopy **230**, 27 (2008).

[68] J. B. Pendry, A. J. Holden, D. J. Robbins and W. J. Stewart. *Magnetism from conductors and enhanced nonlinear phenomena.* IEEE Trans. Microwave Theory Tech. **47**, 2075 (1999).

[69] M. Dienerowitz. *Magnetism at Optical Frequencies.* MSc Thesis, University of Karlsruhe, Karlsruhe. Published online http://photonics.tfp.uni-karlsruhe.de/ (2005).

[70] J. A. Veerman, M. F. Garcia-Parajo, L. Kuipers and N. F. V. Hulst. *Single molecule mapping of the optical field distribution of probes for near-field microscopy.* Journal of Microscopy **194**, 477 (1999).

[71] R. J. Moerland, T. H. Taminiau, L. Novotny, N. F. van Hulst and L. Kuipers. *Reversible polarization control of single photon emission.* Nano Lett. **8**, 606 (2008).

[72] E. Verhagen, M. Spasenović, A. Polman and L. Kuipers. *Nanowire plasmon excitation by adiabatic mode transformation.* Phys. Rev. Lett. **102**, 20390 (2009).

[73] C. Enkrich, M. Wegener, S. Linden, S. Burger, L. Zschiedrich, F. Schmidt, J. F. Zhou, T. Koschny and C. M. Soukoulis. *Magnetic metamaterials at telecommunication and visible frequencies.* Phys. Rev. Lett. **95**, 203901 (2005).

[74] R. Marques, F. Medina and R. Rafii-El-Idrissi. *Role of bianisotropy in negative permeability and left-handed metamaterials.* Phys. Rev. B. **65**, 144440 (2002).

[75] N. Liu, H. Liu, S. Zhu and H. Giessen. *Stereometamaterials.* Nature Photon. **3**, 157 (2009).

[76] J. Garcia-Garcia, F. Martin, J. D. Baena, R. Marques and L. Jelinek. *On the resonances and polarizabilities of split ring resonators.* J. Appl. Phys. **98**, 033103 (2005).

[77] R. Jones and C. Wykes. *Holographic and Speckle Interferometry.* Cambridge University Press, Cambridge.

[78] J. E. Baldwin and C. A. Haniff. *The application of interferometry to optical astronomical imaging.* Phil. Trans. pages 969–986 (2002).

[79] S. J. FRASIER and A. J. CAMPS. *Dual-beam interferometry for ocean surface current vector mapping.* IEEE Trans. Geosci. Remote Sens. **39**, 401 (2001).

[80] S. Stramondo, M. Tesauro, P. Briole, E. Sansosti, S. Salvi, R. Lanari, M. Anzidei, P. Baldi, G. Fornaro, A. Avallone, M. F. Buongiorno, G. Franceschetti and E. Boschi. *The september 26, 1997 colfiorito, italy, earthquakes.* Geophys. Res. Lett. **26**.

[81] A. M. Zysk, F. T. Nguyen, A. L. Oldenburg, D. L. Marks and S. A. Boppart. *Optical coherence tomography: a review of clinical development from bench to bedside.* J. Biomed. Opt. **12**, 051403 (2007).

[82] G. Dolling, C. Enkrich, M. Wegener, C. M. Soukoulis and S. Linden. *Simultaneous negative phase and group velocity of light in a metamaterial.* Science **312**, 892 (2006).

[83] M. L. M. Balistreri, H. Gersen, J. P. Korterik, L. Kuipers and N. F. van Hulst. *Tracking femtosecond laser pulses in space and time.* Science **294**, 1080 (2001).

[84] T. H. R. Skyrme. *A non-linear field theory.* Proc. R. Soc. A **260**, 127 (1961).

[85] J. R. Abo-Shaeer, C. Raman, J. M. Vogels and W. Ketterle. *Observation of vortex lattices in bose-einstein condensates.* Science **292**, 476 (2001).

[86] K. W. Madison, F. Chevy, W. Wohlleben and J. Dalibard. *Vortex formation in a stirred bose-einstein condensate.* Phys. Rev. Lett. **84**, 806 (2000).

[87] M. R. Matthews, B. P. Anderson, P. C. Haljan, D. S. Hall, C. E. Wieman and E. A. Cornell. *Vortices in a bose-einstein condensate.* Phys. Rev. Lett. **83**, 2498 (1999).

[88] A. A. Abrikosov. *On the magnetic properties of superconductors of the second group.* Sov. Phys. JETP **5**, 1174 (1957).

[89] P. Coullet, L. Gil and J. Lega. *Defect-mediated turbulence.* Phys. Rev. Lett. **62**, 1619 (1989).

[90] H. F. Schouten, T. D. Visser, G. Gbur, D. Lenstra and H. Blok. *Connection between phase singularities and the radiation pattern of a slit in a metal plate.* Phys. Rev. Lett. **93**, 173901 (2004).

[91] N. Shvartsman and I. Freund. *Vortices in random wave fields: Nearest neighbor anticorrelations.* Phys. Rev. Lett. **72**, 1008 (1994).

[92] S. Zhang and A. Z. Genack. *Statistics of diffusive and localized fields in the vortex core.* Phys. Rev. Lett. **99**, 203901 (2007).

[93] J. V. Hajnal. *Singularities in the transverse fields of electromagnetic waves. II. observations on the electric field.* Proc. R. Soc. A **414**, 447 (1987).

[94] R. W. Schoonover and T. D. Visser. *Polarization singularities of focused, radially polarized fields.* Opt. Express **14**, 5733 (2006).

[95] F. Flossmann, U. T. Schwarz, M. Maier and M. R. Dennis. *Polarization singularities from unfolding an optical vortex through a birefringent crystal.* Phys. Rev. Lett. **95**, 253901 (2005).

[96] M. V. Berry, M. R. Dennis and R. L. Lee. *Polarization singularities in the clear sky.* New Journal of Physics **6**, 162 (2004).

[97] F. Flossmann, K. O'Holleran, M. R. Dennis and M. J. Padgett. *Polarization singularities in 2d and 3d speckle fields.* Phys. Rev. Lett. **100**, 203902 (2008).

[98] D. Rychtarik, B. Engeser, H.-C. Nägerl and R. Grimm. *Two-dimensional bose-einstein condensate in an optical surface trap.* Phys. Rev. Lett. **92**, 173003 (2004).

[99] W. Hansel, P. Hommelhoff, T. W. Hansch and J. Reichel. *Bose-einstein condensation on a microelectronic chip.* Nature **413**, 498 (2001).

[100] J. Bravo-Abad, M. Ibanescu, J. D. Joannopoulos and M. Soljacic. *Photonic crystal optical waveguides for on-chip bose-einstein condensates.* Phys. Rev. A **74**, 053619 (2006).

[101] K. G. Lee, H. W. Kihm, J. E. Kihm, W. J. Choi, H. Kim, C. Ropers, D. J. Park, Y. C. Yoon, S. B. Choi, D. H. Woo, J. Kim, B. Lee, Q. H. Park, C. Lienau and D. S. Kim. *Vector field microscopic imaging of light.* Nature Photon. **1**, 53 (2007).

[102] Z. H. Kim and S. R. Leone. *Polarization-selective mapping of near-field intensity and phase around gold nanoparticles using apertureless near-field microscopy.* Opt. Express **16**, 1733 (2008).

[103] M. Sandtke, R. J. P. Engelen, H. Schoenmaker, I. Attema, H. Dekker, I. Cerjak, J. P. Korterik, F. B. Segerink and L. Kuipers. *Novel instrument for surface plasmon polariton tracking in space and time.* Rev. Sci. Instrum. **79**, 013704 (2008).

[104] E. Yablonovitch. *Inhibited spontaneous emission in Solid-State physics and electronics.* Phys. Rev. Lett. **58**, 2059 (1987).

[105] T. Yoshie, A. Scherer, J. Hendrickson, G. Khitrova, H. M. Gibbs, G. Rupper, C. Ell, O. B. Shchekin and D. G. Deppe. *Vacuum rabi splitting with a single quantum dot in a photonic crystal nanocavity.* Nature **432**, 200 (2004).

[106] K. Hennessy, A. Badolato, M. Winger, D. Gerace, M. Atature, S. Gulde, S. Falt, E. L. Hu and A. Imamoglu. *Quantum nature of a strongly coupled single quantum dot-cavity system.* Nature **445**, 896 (2007).

[107] V. R. Almeida, C. A. Barrios, R. R. Panepucci and M. Lipson. *All-optical control of light on a silicon chip.* Nature **431**, 1081 (2004).

[108] Q. Xu, B. Schmidt, S. Pradhan and M. Lipson. *Micrometre-scale silicon electro-optic modulator.* Nature **435**, 325 (2005).

[109] W. C. L. Hopman, K. O. van der Werf, A. J. F. Hollink, W. Bogaerts, V. Subramaniam and R. M. de Ridder. *Nano-mechanical tuning and imaging of a photonic crystal micro-cavity resonance.* Opt. Express **14**, 8745 (2006).

[110] L. Lalouat, B. Cluzel, P. Velha, E. Picard, D. Peyrade, J. P. Hugonin, P. Lalanne, E. Hadji and F. de Fornel. *Near-field interactions between a subwavelength tip and a small-volume photonic-crystal nanocavity.* Phys. Rev. B **76**, 41102 (2007).

[111] S. Mujumdar, A. F. Koenderink, T. Snner, B. C. Buchler, M. Kamp, A. Forchel and V. Sandoghdar. *Near-field imaging and frequency tuning of a high-Q photonic crystal membrane microcavity.* Opt. Express **15**, 17214 (2007).

[112] F. Intonti, S. Vignolini, F. Riboli, A. Vinattieri, D. S. Wiersma, M. Colocci, L. Balet, C. Monat, C. Zinoni, L. H. Li, R. Houdre, M. Francardi, A. Gerardino, A. Fiore and M. Gurioli. *Spectral tuning and near-field imaging of photonic crystal microcavities.* Phys. Rev. B **78**, 041401 (2008).

[113] M. Li, W. H. P. Pernice, C. Xiong, T. Baehr-Jones, M. Hochberg and H. X. Tang. *Harnessing optical forces in integrated photonic circuits.* Nature **456**, 480 (2008).

[114] C. M. Soukoulis, S. Linden and M. Wegener. *Negative refractive index at optical wavelengths.* Science **315**, 47 (2007).

[115] R. J. P. Engelen, D. Mori, T. Baba and L. Kuipers. *Subwavelength structure of the evanescent field of an optical bloch wave.* Phys. Rev. Lett. **102**, 023902 (2009).

[116] J. T. Robinson and M. Lipson. *Far-Field control of radiation from an individual optical nanocavity: Analogue to an optical dipole.* Phys. Rev. Lett. **100**, 043902 (2008).

[117] M. Husnik, M. W. Klein, N. Feth, M. Konig, J. Niegemann, K. Busch, S. Linden and M. Wegener. *Absolute extinction cross-section of individual magnetic split-ring resonators.* Nature Photon. **2**, 614 (2008).

[118] E. D. Minot, Y. Yaish, V. Sazonova and P. L. McEuen. *Determination of electron orbital magnetic moments in carbon nanotubes.* Nature **428**, 536 (2004).

[119] R. C. Haddon. *Magnetism of the carbon allotropes.* Nature **378**, 249 (1995).

[120] S. Noda, M. Fujita and T. Asano. *Spontaneous-emission control by photonic crystals and nanocavities.* Nature Photon. **1**, 449 (2007).

[121] O. Painter, R. K. Lee, A. Scherer, A. Yariv, J. D. O'Brien, P. D. Dapkus and I. Kim. *Two-Dimensional photonic Band-Gap defect mode laser.* Science **284**, 1819 (1999).

[122] S. M. Spillane, T. J. Kippenberg and K. J. Vahala. *Ultralow-threshold raman laser using a spherical dielectric microcavity.* Nature **415**, 621 (2002).

[123] T. Carmon and K. J. Vahala. *Visible continuous emission from a silica microphotonic device by third-harmonic generation.* Nature Phys. **3**, 430 (2007).

[124] S. Noda, A. Chutinan and M. Imada. *Trapping and emission of photons by a single defect in a photonic bandgap structure.* Nature **407**, 608 (2000).

[125] B. Song, S. Noda and T. Asano. *Photonic devices based on In-Plane hetero photonic crystals.* Science **300**, 1537 (2003).

[126] P. Michler, A. Kiraz, C. Becher, W. V. Schoenfeld, P. M. Petroff, L. Zhang, E. Hu and A. Imamoglu. *A quantum dot Single-Photon turnstile device.* Science **290**, 2282 (2000).

[127] E. Chow, A. Grot, L. W. Mirkarimi, M. Sigalas and G. Girolami. *Ultracompact biochemical sensor built with two-dimensional photonic crystal microcavity.* Opt. Lett. **29**, 1093 (2004).

[128] L. Lalouat, B. Cluzel, F. de Fornel, P. Velha, P. Lalanne, D. Peyrade, E. Picard, T. Charvolin and E. Hadji. *Subwavelength imaging of light confinement in high-Q/small-V photonic crystal nanocavity.* App. Phys. Lett. **92**, 111111 (2008).

[129] M. Sandtke and L. Kuipers. *Spatial distribution and near-field coupling of surface plasmon polariton bloch modes.* Phys. Rev. B **77**, 235439 (2008).

[130] M. Tatarakis, I. Watts, F. N. Beg, E. L. Clark, A. E. Dangor, A. Gopal, M. G. Haines, P. A. Norreys, U. Wagner, M. Wei, M. Zepf and K. Krushelnick. *Laser technology: Measuring huge magnetic fields.* Nature **415**, 280 (2002).

[131] A. Pukhov and J. Meyer-ter-Vehn. *Relativistic magnetic Self-Channeling of light in Near-Critical plasma: Three-Dimensional Particle-in-Cell simulation.* Phys. Rev. Lett. **76**, 3975 (1996).

[132] M. C. Noecker, B. P. Masterson and C. E. Wieman. *Precision measurement of parity nonconservation in atomic cesium: A Low-Energy test of the electroweak theory.* Phys. Rev. Lett. **61**, 310 (1988).

[133] R. A. Shelby, D. R. Smith and S. Schultz. *Experimental verification of a negative index of refraction.* Science **292**, 77 (2001).

[134] W. L. Barnes, A. Dereux and T. W. Ebbesen. *Surface plasmon subwavelength optics.* Nature **424**, 824 (2003).

[135] S. G. Johnson, M. L. Povinelli, M. Soljacic, A. Karalis, S. Jacobs and J. D. Joannopoulos. *Roughness losses and volume-current methods in photonic-crystal waveguides.* App. Phys. B **81**, 283 (2005).

[136] J. A. Stratton. *Electromagnetic theory.* McGraw Hill (1941).

Samenvatting

De mensheid is er in geslaagd de interactie tussen licht en materie te beheersen om haar kwaliteit van leven te verbeteren. Wij vinden allerdaagse handelingen, zoals het aanzetten van het licht in een donkere kamer om onze omgeving te kunnen zien, vanzelfsprekend. Meestal zijn we ons helemaal niet bewust van alle lichtmaterie interacties. Als je het lichtknopje omschakelt beweegt het licht zich door de lucht voort, wordt verstrooid door de voorwerpen in de kamer, beweegt nogmaals door de lucht en heeft - uiteindelijk interactie heeft met onze ogen. Pas op dat moment zien we de kamer.

Tegenwoordig worden verfijnde technieken om de licht-materie interactie te controleren vereist. Snellere overdracht en berekening van informatie kan worden bereikt door optica te gebruiken. Efficiëntere duurzame energie productie kan worden verkregen met foto-voltaïsche systemen en lasers kunnen worden gebruikt voor zeer nauwkeurige medische methoden. Nano-optica is een van de moderne antwoorden op deze behoeften. Nano-optica is sterk toepassingsgericht, niet alleen fundamentele kennis wordt nagestreefd maar ook een bijdrage aan de maatschappij. Onderzoek naar de kwantum en klassieke eigenschappen van licht in interactie met geordende, ongeordende en quasi geordende diëlektrische structuren of metallische en metaal-diëlektrische materialen die op de nanoschaal op maat gemaakt zijn, stimuleert de interesse van de wetenschappelijke gemeenschappen van alle geïndustrialiseerde samenlevingen.

Dit proefschrift overspant drie belangrijke velden binnen de nano-optica: fotonische kristallen, metamaterialen en nabije-veld microscopie. Door met een unieke experimentele opstelling het nabije-veld te meten konden we niet alleen de elektrische maar ook de magnetische eigenschappen van fotonische nanostructuren bij optische frequenties onderzoeken.

Hoofdstuk 1 bevat een korte samenvatting van de onderwerpen die gerelateerd zijn met dit proefschrift. Na een korte introductie over licht-materie koppeling, beschrijven we enkele van de moderne strategieën die gebruikt worden om de stroming van licht te controleren zoals fotonisch kristal golfgeleiders en fotonisch kristal trilholtes. Deze fotonische nanostructuren worden gekarakteriseerd door gecompliceerde interferentie patronen die ontstaan door de meervoudige reflecties die het licht ondergaat. Omdat in licht velden die uit verschillende golven zijn opgebouwd singulariteiten kunnen voorkomen, zoals we in Hoofdstuk 3 zullen zien, worden in dit hoofdstuk enkele van de basale concepten van de singuliere optica beschreven. Om de veld verdeling van licht in fotonische nanostructuren te visualiseren is een zeer hoge resolutie nodig die standaard microscopie ons niet kan bieden. Nabije-veld microscopie werd dan geïntroduceerd als een krachtig instrument dat ons de benodigde subgolflengte resolutie verschaft.

In Hoofdstuk 2 is de elektromagnetische respons van drie verschillende nabije-veld sondes besproken. Na overwegingen gebaseerd op de concepten van metamaterialen, hebben we laten zien dat de koppeling tussen licht en een gecoate sonde beschreven kan worden door een elektrische en magnetische polariseerbaarheids matrix. We hebben ook laten zien dat als we een lucht gat maken in de aluminium coating, de polariseerbaarheidsmatrix van de sonde op zon manier verandert dat de detectie van het magnetische veld mogelijk is. Vervolgens introduceerden we de fase-gevoelige, tijds-opgeloste nabije-veld microscoop die in alle metingen in dit proefschrift gebruikt wordt.

In het volgende deel van het proefschrift hebben we enkele van de optische eigenschappen die bediscussieerd zijn in Hoofdstuk 2 experimenteel bewezen en gebruikt om een nieuw type onderzoek uit te voeren. In Hoofdstuk 3 toonden we aan dat een gecoate sonde gecombineerd met een polarisatie gevoelige nabije-veld microscoop ons in staat stelt onafhankelijk de componenten van het elektrische veld van licht dat in het vlak in een 2D fotonisch kristal golfgeleider voort beweegt te meten. Vervolgens vonden we twee circulair gepolariseerde singulariteiten in het centrum van de golfgeleider. We vonden twee ster-C punten met tegengestelde draairichting op een afstand van slechts 200 nm van elkaar. Ook is de zeer gestructureerde polarisatie verdeling van licht dat door de golfgeleider beweegt gedetecteerd. We vonden de kennis van de polarisatie toestand op de nanoschaal waardevolle informatie, voor toekomstige toepassingen gebaseerd op de controle van de spin toestanden van emitters.

In Hoofdstuk 4 demonstreerden we de koppeling tussen een gecoate sonde en een fotonische kristal holte door de magnetische component van het opgesloten licht. We bereikten een niet eerder waargenomen blauw verschuiving van de holte resonantie en een onverwachte vergroting van de foton-levensduur in de holte. Deze ontdekkingen zullen onderzoek stimuleren dat het gat tussen fotonische kristallen en metamaterialen overbrugt en de weg openen voor nieuwe strategieën om licht te controleren.

In Hoofdstuk 5 was het koppelingsmechanisme tussen een L3-zijwaarts gekoppelde nano-holte en de mode van een toegangsgolfgeleider uitgezocht. Door fase-gevoelige tijdsopgeloste nabije-veld microscopie en daaropvolgende Fourier analyse toonden we aan dat de -1 Bloch harmonische van licht dat in de fotonisch kristal golfgeleider voort beweegt verantwoordelijk is voor de koppeling tussen golfgeleider en nanoholte. Bovendien bepaalden we direct de foton levensduur van het opgesloten licht in de holte zonder enige referentie meting.

In Hoofdstuk 6 toonden we aan dat een gefunctionaliseerde gecoate sonde een magnetische respons vertoont. We gebruikten deze respons om direct het magnetische veld bij optische frequenties te bepalen. Door en nabije-veld experiment uit te voeren op een richel golfgeleider, detecteerden we de magnetische component van het propagerende licht. Wij geloven dat deze ontdekkingen een impuls zullen geven aan nabije-veld onderzoek op een nieuw nauwkeurigheidsniveau waarin ook het magnetische veld van het licht gedetecteerd wordt door een nabije-veld sonde.

-Translated by Jord C. Prangsma-

Riassunto

La luce viene utilizzata dagli essere vivente per il loro sostentamento sia in modi diretti (ad esempio, la fotosintesi clorofilliana delle piante) che indiretti (ad esempio, la vista negli animali). Il genere umano, in particolare, è riuscito a padroneggiare l'interazione tra luce e materia per migliorare la qualità della propria vita. Diamo per scontato azioni quotidiane, come accendere la luce in una stanza buia per vedere l'ambiente circostante, senza apprezzare appieno tutte le interazioni luce-materia che si verificano. In effetti, la luce propagando attraverso l'aria interagisce con essa, dopodiché viene riflessa dagli oggetti presenti nella stanza per poi nuovamente propagare attraverso l'aria ed infine viene percepita dai nostri occhi. Solo a quel punto noi riusciamo a vedere la stanza.

Al giorno d'oggi sono richieste raffinate tecniche per controllare l'interazione luce-materia. Il trasferimento e l'elaborazione delle informazioni in futuro saranno realizzati più velocemente utilizzando l'ottica; con il sistema fotovoltaico si può ottenere una efficiente produzione di energia a bassa emissione di carbonio; dispositivi laser possono essere utilizzati per le più accurate procedure mediche. La nano-ottica è una delle risposte a queste moderne esigenze. Infatti, la nano-ottica è fortemente orientata verso future applicazioni, cercando non solo di acquisire nuove conoscenze di fisica fondamentale, ma anche di creare un beneficio per la società che sostiene la ricerca stessa. Le indagini sperimentali sull'interazione delle proprietà quantistiche e classiche della luce con strutture dielettriche disordinate, ordinate e quasi-ordinate, o materiali metallici e metallo-dielettrici strutturate su scale nanometriche, stimolano l'interesse delle comunità scientifiche di tutte le società industrializzate.

Questa tesi si estende su tre campi centrali della nano-ottica quali cristalli fotonici, metamateriali e microscopia a campo vicino. Attraverso esperimenti orientati ad una migliore comprensione di questo moderno tipo

di microscopia, abbiamo scoperto che è possibile studiare non solo le proprietà elettriche, ma anche le proprietà magnetiche di nanostrutture fotoniche a frequenze ottiche.

Nel Capitolo 1 abbiamo fornito una breve sintesi degli argomenti correlati a questa tesi. Dopo una breve introduzione sull'interazione luce-materia, abbiamo discusso di alcune delle principali odierne strategie impiegate per controllare la propagazione della luce, focalizzando la nostra attenzione sui cristalli fotonici. Questi particolari materiali in futuro potranno essere utilizzati per creare chip miniaturizzati dove lo luce possa scorrere e le informazioni da essa portate elaborate. Questa futurista tecnologia sarà, poiché la luce può trasportare le informazioni molto più velocemene e con una maggiore qualità sulla lunga distanza. Una delle proprietà più significative dei cristalli fotonici è la possibilità di intrappolare la luce per lunghi periodi di tempo in volumi piccolissimi (nanocavità): 10^{-19} m^3, cioè un milionesimo, di un miliardesimo di una tazzina da caffè. All'interno dei cristalli fotonici la luce interagisce fortemente con il materiale. A causa di queste interazioni, alcune delle proprietà della luce non sono più definite in maniera appropriata in specifici punti, detti *punti singolari*, e la luce stessa non 'sa' come comportarsi. Questi fenomeni ottici sono investigati dall'ottica singolare, che viene introdotta in questo capitolo della tesi. Poiché queste singolarità possono apparire in ogni tipo di onda, l'ottica singolare risulta essere molto importante. Infatti, le scoperte fatte in questo campo possono essere utilizzate in campi di ricerca completamente differenti, come la geologia, l'oceanografia, la chimica, la fisica delle alte energie, la medicina, etc. Per poter osservare queste ed altre proprietà ottiche dei cristalli fotonici, la comune microscopia non è sufficiente, perchè la massima risoluzione da essa ottenibile è comparabile con la lunghezza d'onda della luce. Per questo alla fine del Capitolo 1 e nel Capitolo 2 vengono introdotti sia la microscopia a campo vicino in generale che il microscopio utilizzato in questo lavoro di tesi. La microscopia a campo vicino fornisce una risoluzione molto minure della lunghezza della luce utilizzando una piccolissima sonda che raccoglie una piccola quantita della luce presente nel campione investigato. In questa tesi viene data un particolare attenzione alla componente più importante del microscopio: la sonda (o punta) metallizzata. Il principale risultato di questo lavoro di tesi è dato dall'interpretazione sulle proprietà ottiche di questa particolare sonda, proprietà che sono il soggetto di venti anni di dibattito scientifico.

Abbiamo scoperto che la sonda non è sensibile solamente al campo elettrico della luce ma anche a quello magnetico. Questa è una sorprendente proprietà, considerando che in natura la luce interagisce con la materia solo attraverso il campo elettrico. Esempi di tale interazione nella vita di tutti i giorn sono innumerevoli, fra gli altri le lenti degli occhiali, gli specchi, la luce diffusa da un banco di nebbia, la distorsione delle immagini data dalla superficie dell'acqua, etc.. tutte queste interazion avvengono attraverso la componente elettrica della luce poich 'e la materia esibisce un trascurabile magentismo. La sonda metallizzata, al contrario, esibisce un forte magnetismo che può essere sfruttato per studi di ottica fondamentale e per applicazioni, come dimostrato in questo libro.

Nella seconda parte della tesi vengono descritti i risultati sperimentali ottenuti utilizzando le proprietà ottiche della sonda metallizzata descritte nella prima parte. Qui riportiamo una sintesi dei tre principali risultati ottenuti. Nel Capitolo 3 abbiamo dimostrato che una sonda metallizzata può misurare simultaneamente differenti campi elettrici della luce in un cristallo fotonico. Abbiamo quindi scoperto che il campo elettrico ha una complicata distribuzione spaziale che varia drasticamente in soli 200 nm (200 miliardesimi di metro) e presenta alcune delle menzionate singolarità. Le nostre osservazioni sperimentali risultano estrememamente importanti, considerando che molte delle future applicazioni per i chip derivanti da questi materiali si basano sulla conoscenza della distribuzione del campo elettrico al loro interno.

Nel Capitolo 4 abbiamo dimostrato che si possono controllare le proprietà ottiche di una nanocavità sfruttado il magnetismo di una sonda metallizzata. Avvicinando la punta alla nanocavità ad una distanza minore di 20 nm é possible interagire con il campo magnetico della luce intrappolata al suo interno. La luce viene 'trattenuta' nella cavità più a lungo di quanto non farebbe senza la sonda nelle vicinanze, come se la sonda fosse un ago piccolissimo che 'afferra' la luce e la trattiene dentro una piccolissima scatola (la nanocavità). Tale esperimento prova che sia possibile migliorare la qualità di una nanocavità, che si basa solamente sull'interazione elettrica luce-materia, utilizzando l'interazione magnetica tra la luce e la sonda.

Infine, nel Capitolo 6 abbiamo dimostrato che è possibile sondare il campo magentico di luce propagante in una struttura fotonica a frequenze ottiche. Una tale misurazione non era mai stata effettuata poiché, in generale, il campo magnetico interagisce così debolmente con i materiali che non può essere misurato. Modificando la sonda metallizzata è possible aumentare l'interazione tra campo magnetico e punta stessa e, quindi, sondare la componente magnetica della luce. Riteniamo che questi risultati daranno un forte impulso alle microscopia a campo vicino. Nuove indagini in cui il campo magnetico viene trattato con pari digità rispetto al campo elettrico saranno fondamentali per la comprensione dei neo-nati metamateriali, i quali esibiscono un forte magnetismo a frequenze ottiche.

Acknowledgements

When I wrote my diploma dissertation, I began the long list of acknowledgements addressing myself as the person who contribute the most to the achievement of my degree in physics. Here, I first have to acknowledge my love, Benedetta, and the rest of my family, my daughter Margherita and my son Niccolò, as the essential ingredients for the accomplishment of my PhD degree. I dragged her (them) to another country far from relatives and friends (this is a really demanding action for a Florentine) and, when life did not go as planned (as always life does), they adapted to the new conditions so that my wishes could become true. The actions and decisions which supported me for four years were driven by LOVE and this love MUST at least be acknowledged. Grazie mille, amori miei.

Right after my family, I thank my supervisor Kobus. I owe him a lot, not only for teaching me HOW to be a researcher (everything included) but also for personal reasons. Due to my familiar situation and my ’madness’, I was far from the ’perfect’ PhD, who generally wants to go to conferences and works during weekends. Although at the beginning we both wondered ”why did Diederik suggest this guy as PhD student?”, he always supported me beyond his actual duties. I think that we decently worked it out, eventually, and now I ended my PhD period successfully. Thank you very much for everything.

I thank now my two *paranimfen*, Dries and Jord. Appointing them as *paranimf* was just a mere consequence of our relationships in these years. Dries taught me so many things that my mind cannot just bear them all and, what is much more important, was a great advisor *nelle cose della vita* (my English doesn’t work here). Thanks for seriously offering your help when it seemed I was in real need! I’ll miss our daily starting coffee so much, man! Jord was my room mate for 2,5 years and I enjoyed every day (.....almost). Your practical wisdom helped me a lot in my research and in my life here in the Netherlands. I think I won't find a better mate anywhere.

My relationship with Marko is a bit weird, I think. We didn't party as much as we wanted. It feels like a sliding-doors type of story, full of 'ifs'. If I would have been younger, if I would not be married and with children, if he would have come in this country two years earlier: lots of ifs. If some of these ifs would have been fulfilled we would have had a lot of fun! But that's life. I thank you for the trouble-free moments we spent together, for coming back from your vacation just to attend my defence and just for being yourself, no matter what. Together with you, I wish to thank people of the crew that helped me during my work and had fun with me: Schoen, Aron, Gijs (John) (for the time spent on my future project), Chris, Ivana, Jean, dj D, Hakki and Tobias. In particular, I thank Aron and Marko for the thorough grammar check they performed on this thesis and Tobias for some of the calculations showed in the Appendices and for the time spent together with our families.

So I thank also Branka, Lukas, Hadas, Mayan and Arie. Besides the nice moments spent together, I also thank you for the support you gave to my wife during the daily practical things, making our staying here possible. In particular, I'd like to thanks Alex for her support in my PhD party and for all the baby clothes. Un graziamento particolare alla famiglia Bizzarro: Elena, Sergio, Marco ed Ale. Quando eravamo insieme ci sembrava di essere in Italia e questo ha reso meno pesante la nostalgia di Casa. Con voi siamo riusciti ad avere sprazzi della vita semplice e leggera che io e la Bene abbiamo sempre voluto e che speriamo di aver una volta reintrati in Italia. Grazie di cuore. Ci mancherete da morire. Ma abbiamo una stanza per gli ospiti che vi aspetta a Firenze!

Special thanks to the two former members of the group who taught me to use PHANTOM and to speak understandable English (!!!): Rob and Marijn. Thank you very much, guys. Thanks to former and current members of the Center for Nanophotonics. At the beginning of my PhD I wasn't really happy with the Thursday Colloquium but afterwards I realized it was only cultural shock and then I started to understand how useful it is. In particular I'd like to sincerely thank Ad. As you said, once you went (unexpectedly) daddy on me and you did something GOOD that day. My 'mad'-doctor also thanks you (!!!).

Ringrazio anche i membri del gruppo di nano-ottica a Firenze, in particolare Silvia, Diederik e Francesca, per il lavoro fatto assieme e per avermi sempre fatto sentire a casa tutte le volte che ero nel vostro laboratorio. Special thanks to Diederik who 'sent' me to AMOLF when I told him that I wanted to go abroad.

Infine, mi scuso con tutta la mia Famiglia allargata (intendo familiari ed amici) per essere andato via privandomi della mia rifulgente presenza e per aver portato con me la Bene, la Marghe e Nicco per 4 anni. Pensavamo, e pensiamo, che fosse la scelta giusta (abbiamo solo seguito il flusso...), ma è stata pagata ad un caro prezzo, emotivo ed economico, anche da parte vostra e non solo nostra. La NOSTALGIA, nostra e vostra, è stata così grande che ritengo debba essere riconosciuta e ricordata.

Acknowledging the giants on which we stand.

In 1887, H.R. Hertz performed several experiments in the microwave regime to verify "Maestro Maxwell"'s hypotheses about electromagnetism (1856). Hertz wanted to generate and detect electromagnetic waves to prove their existence. Radiation was produced by accumulating electric charges at the extremities of a spark gap, which are two metallic spheres in close proximity (see images in the back of the cover of this thesis). Sparks periodically occurred and microwave radiation was emitted. With the use of a mirror placed several meters far from the source of radiation, he generated a standing wave. To detect this standing wave, Hertz used a metallic wire loop with a spark gap placed between mirror and source. This detector was the first split-ring resonator ever made. In fact, sparks occurred across the spark gap when the detector was placed where the magnetic field was maximum. Those sparks were a clear signature of a dipolar charge distribution through the spark gap, which acted as a capacitor, induced via magnetic component of the microwave radiation.

In essence, more than 120 years ago Hertz realized the microwave analogue of the experiment described in Chapter 6, which is performed at optical frequencies.

-The picture displaying H.R. Hertz has been downloaded from Wikipidia (www.-wikipidia.org). The drawings and picture of the setup employed by Hertz is a courtesy of John Jenkins (www.sparkmuseum.com). The picture of the cover was done by Marchiara.-

Heinrich Rudolf Hertz
(22/02/1857 – 01/01/1894)

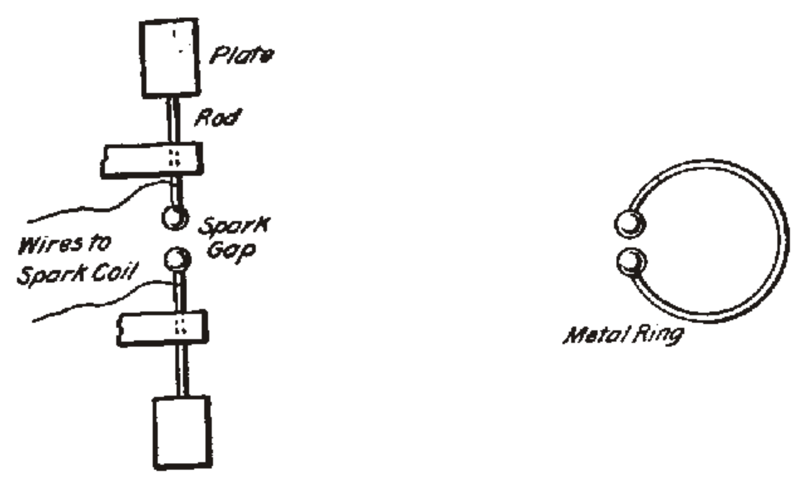

Schematic representation of the equipment employed by Hertz in the experiment performed in the 1887. He used the first split-ring resonator ever made!

Image of the
equipment
employed by Hertz

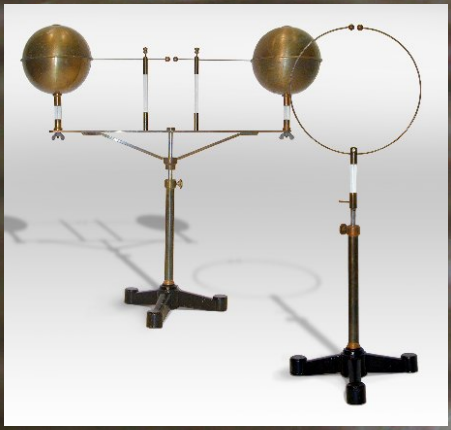

- More information in the last page of this thesis -